Impact Force and Stress Distribution of Drop Impact

A DISSERTATION
SUBMITTED TO THE FACULTY OF THE GRADUATE SCHOOL
OF THE UNIVERSITY OF MINNESOTA
BY

Ting-Pi Sun

IN PARTIAL FULFILLMENT OF THE REQUIREMENTS
FOR THE DEGREE OF
DOCTOR OF PHILOSOPHY

ADVISOR: XIANG CHENG, PH.D.

August, 2021

Acknowledgements

Firstly, I express my sincere gratitude to my advisor Prof. Xiang Cheng for giving me an opportunity on this challenging but promising project. We have spent so many times on discussion, and he inspires me to think questions based on fundamental science. His guidance also helps me improve my writing and presentation skills a lot. We develop the new technique together, and this is the source that I feel a sense of accomplishment in these five years.

Besides, I would like to thank the other committee members, Prof. Paul Dauenhauer, Prof. Lorraine Francis, and Prof. Sungyon Lee for reading and commenting on my works. I also thank Prof. Satish Kumar and Prof. Christopher Macosko for their insightful suggestions whenever I gave presentations on my works.

I also extend my gratitude to my group members, Leonardo Gordillo, Kyle Welch, Shuo Guo, Seunghwan Shin, Truong Pham, Zhengyang Liu, Xiaolei Ma, Yangming Kou, Shashank Kamdar, Yiming Qiao, Dipanjan Ghosh, and Gregorius Pradipta for discussing with me. I also thank the undergraduates who worked with me, Ming Gao, Xiao Liu, Tianyu Liu, Grace Lee, Josh Klukas, and Zhisen Chong.

I really appreciate not only my classmates in NTU but also my good friends Szu-Ming Yang and Hui-Min Chuang. You saved me when I hit rock bottom in my life. I could not move forward to pass the qualification without your help. Also, thanks to all my friends in Taiwan Student Association. We hanged out, had potluck parties, and played sports together. These activities add color to the dull routine of life here.

I sincerely thank my family. My father Chu-Kuo Sun and mother Su-Mei Chen always encourage me and pray for me. You always support me without any hesitation whenever I make any decision. Thanks to my brother Ding-Hao Sun who frequently exchanges ideas with me and inspires me. I believe you will do well in your graduate

career.

I thank the financial support from NSF, the PPG fellowship, the Government Scholarship for Study Abroad from the Ministry of Education of Taiwan, and the Department of Chemical Engineering and Materials Science.

Last but not least, there are so many people that I have earned my gratitude for their contribution, so I thank God.

Dedication

To my beloved family for supporting me over the years.

Abstract

Drop impact is ubiquitous and relevant to many important natural phenomena and industrial applications. Although the kinematics of drop impact has been extensively studied through simulations and high-speed imaging, the understanding of drop impact is still far from fully understood. The studies of dynamics such as the impact force and the stress distribution of drop impact are still relatively scarce. The impact force and the stress distribution lead to the most important consequence throughout the industrial processes and are crucial factors to erosion on substrates or waterjet cutting. Here, we systematically investigate the impact force and the stress distribution of drop impact through experimental studies.

To measure the impact force of drop impact, we synchronize the high-speed camera and the piezoelectric force sensor to obtain the temporal evolution of the impact force and the morphology of drop impact over several orders of magnitudes of Re. We verify the force-time scaling proposed by the self-similar theory at the high Re regime. In the finite Re regime, we consider the effects from the viscosity of liquids and analyze the scaling by using a perturbation method, which matches our experimental results very well. The influence of viscoelasticity is also discussed.

To obtain the temporal evolution of the stress distribution, which has not been measured experimentally, we develop a novel technique "high-speed stress microscopy." We confirm the propagation of the self-similar non-central maximum pressure and shear stress predicted by theories, and the shear force is also quantified. Moreover, we discover the impact-induced surface shock waves, which are crucial to the origin of erosion induced by drop impact.

Furthermore, we measure the shear stress distribution of drop impact on micropatterned surfaces with high-speed stress microscopy. We investigate the influence of micropillars on substrates to the displacement distribution, the shear stress distribution, and the shear force. We hypothesize that the change of shear stress distribution may result from the formation of vortices. Finally, the results show that on the micropatterned surface, the maximum shear stress is suppressed, which is helpful for mitigating erosion to substrates.

Our studies provide the experimental results for understanding the dynamics of drop impact. In addition to the pioneering works of measuring the stress distribution, high-speed stress microscopy can be applied to complicated conditions such as non-Newtonian drop impact and varying the ambient pressure. Besides, it opens the door for experimental exploration of the detailed information inside an impacting drop, including the patterns of the flow and the boundary layer.

Contents

List of Tables

List of Figures

Chapter 1

Introduction and Motivation

- Chapter 1 introduces the background of drop impact.
- Chapter 2 shows the dynamic analysis of the impact force of drop impact.
- Chapter 3 studies the pressure and the shear stress distribution of drop impact by applying the technique "high-speed stress microscopy."
- Chapter 4 discusses the change of the shear stress distribution of drop impact on micropatterned surfaces.
- Chapter 5 summarizes the whole research and provides the outlook on potential future works.

1.1 Background of Drop Impact

Drop impact is ubiquitous in our daily lives. It is relevant to a large number of natural phenomena, such as soil erosion [1], aerosol generated by raindrops [2, 3], formation of granular craters [4, 5, 6], meteorite impact [7], and dispersal of microorganisms by splashing of raindrops [8]. Drop impact also widely encounters in many technical applications, including ink-jet printing [9, 10, 11], spray printing and coating [12, 13], fire suppression by sprinklers [14], solder-drop dispensing in electric circuits [15], and forensic study of blood strain [16, 17], as shown in Figure 1.1. Therefore, understanding the

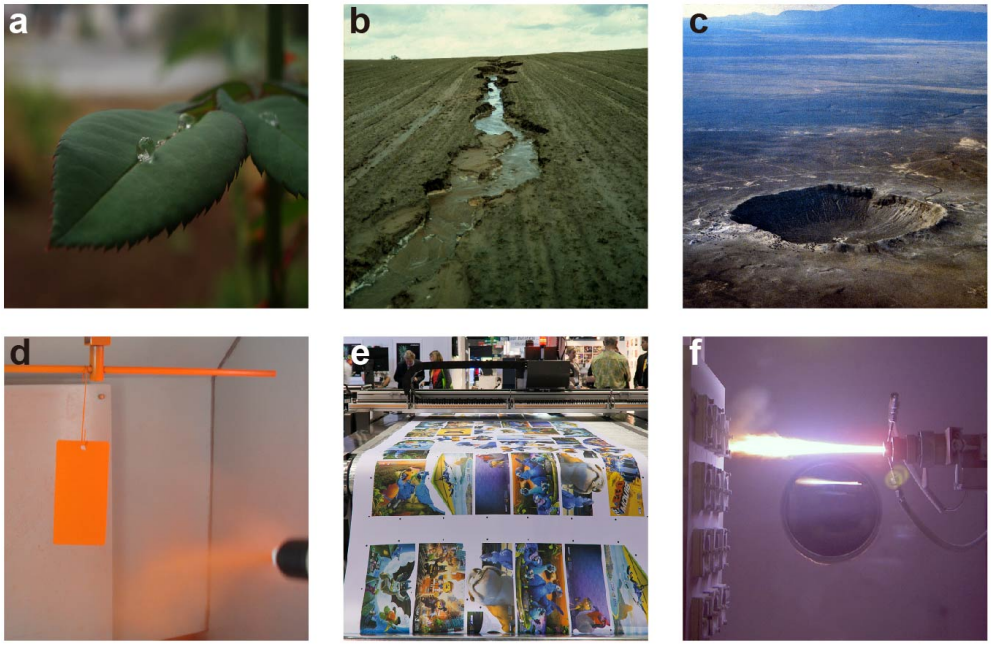

Figure 1.1: Natural phenomena and industrial applications of drop impact. (a) The raining drops on leaves. (b) Soil erosion. (c) Crater by meteorite impact. (d) Spray coating. (e) Ink-jet printing. (f) Plasma spraying. The figures are reproduced from Ref. [18, 19, 20, 21, 22, 23].

mechanism of drop impact is not only for the exploration of fundamental science but also for practical applications in industries.

Due to the importance of drop impact, drop impact has been studied for a long time. The history of studying drop impact can be traced back to 140 years ago. Worthington was one of pioneers to investigate drop impact systematically [24]. He designed an ingenious setup where the spark illumination was triggered by a falling drop, and then he sketched the snapshots of an impacting drop with his flash-illuminated visions. The drawings showed an impacting drop splashing with the fingering and the spreading lamella (Figure 1.2(a)). In the recent 20 years, thanks to the development of high-speed imaging and the advance of stronger numerical calculation [25, 26], the mystery of drop impact is gradually solved via looking into the spatiotemporal structures of drop impact events (Figure 1.2(b),(c)). Nevertheless, in spite of the more than 140 years of research, the omnipresent phenomena of drop impact are still far from fully understood due to the complexity of dynamics behind them.

The complexity of dynamics of drop impact arises from the interplay of various parameters and circumstances. Different parameters of drop impact include the impact velocity of drops (supersonic versus subsonic), shapes of drops (spherical versus elliptic due to oscillation), properties of drops (solid, liquid, or non-Newtonian fluid), types of surfaces (deep liquid pool, thin liquid film, or dry solid surface), directions of impact (normal versus oblique impact), etc [16, 27, 28]. In addition, liquid drops may be miscible or immiscible with pool or film [29]. Whether the liquid film is shallow or deep also matters. Solid surfaces can also be soft or hard, yielding or unyielding, and plane or curved [30]. Furthermore, if the surface of substrates is heated above the boiling point of liquid drop, the liquid would evaporate so fast and that causes the drop floating on a layer of vapor, which acts as a thermally insulating film [31, 32]. Surprisingly, the surrounding pressure and the gas composition can significantly influence the occurrence of splash [33]. Additionally, the dynamics of retract and rebound can be controlled by varying the wettability, or microstructures of solid surfaces [34, 35, 36].

For this research, we mainly emphasize spherical drops normally impacting on solid

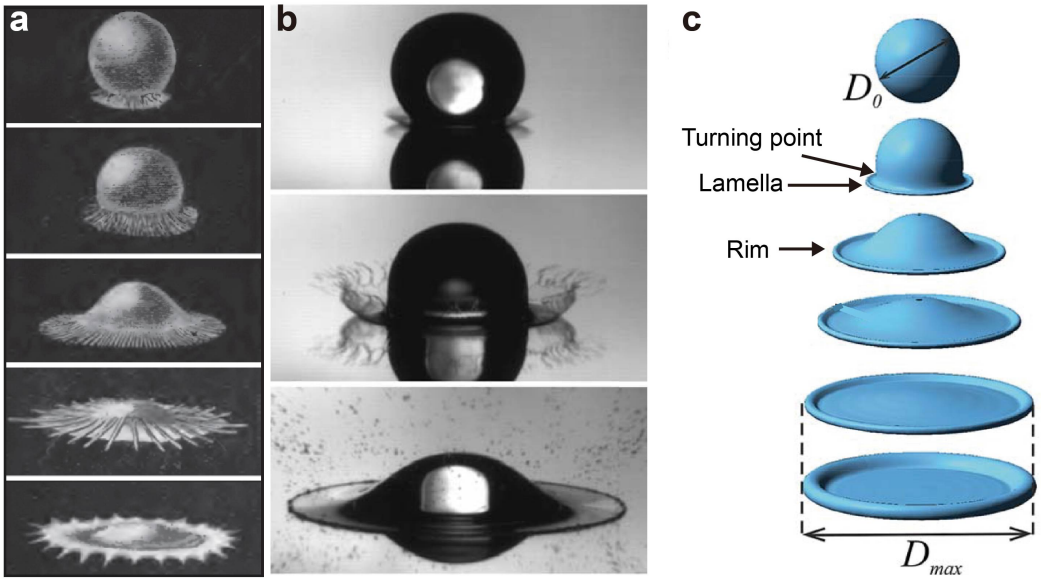

Figure 1.2: Time series of snapshots of drop impact. (a) Worthington's sketches of an impacting drop on a solid surface. (b) Snapshots of drop impact captured by a high-speed camera. (c) Process of an impacting drop through simulation. The kinematic features of an impacting drop including the lamella, the turning point, and the rim are indicated. Reproduced from Ref. [24, 37, 25]. Courtesy of Annual Reviews, American Physical Society, and Royal Society of Chemistry.

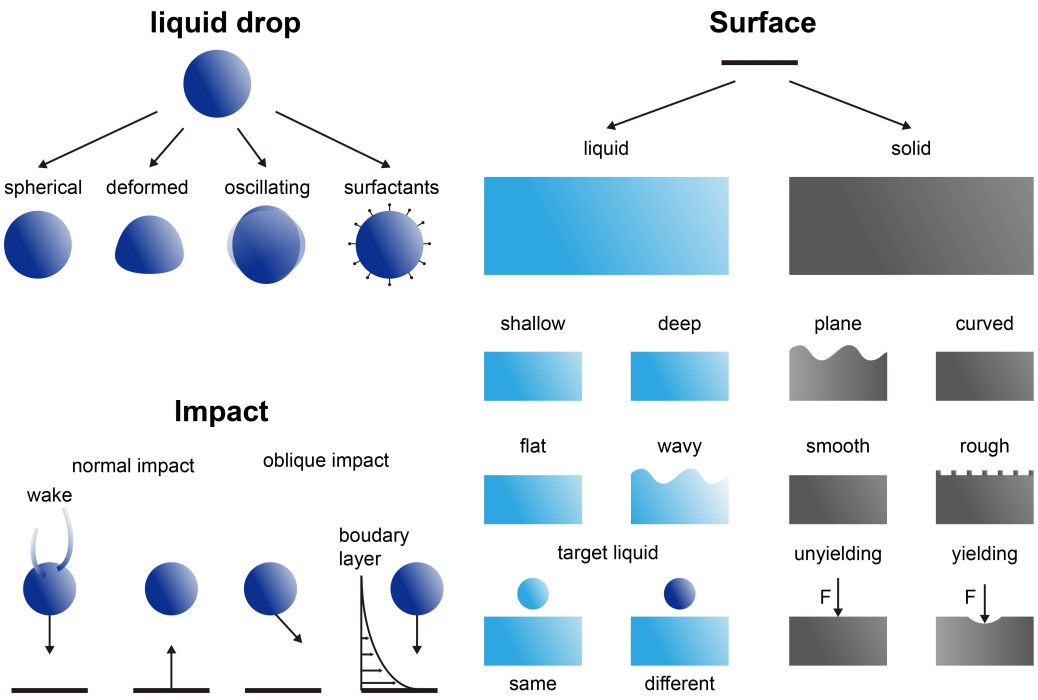

Figure 1.3: Overview of different parameters of drop impact. Generally the parameters can be categorized into three different groups: (1) The composition and the situation of a liquid drop. (2) The impacting angle to the substrate. (3) The properties of substrate such as impacting on a liquid pool or a solid surface. Reproduced from Ref. [16].

surfaces. Typically, the outcomes of drop impact events depend on the following dimensionless groups [26, 27]:

$$Re = \frac{\rho DV}{\mu},\ We = \frac{\rho DV^2}{\mu},\ Fr = \frac{V^2}{gD},\ Ma = \frac{V}{C}, \tag{1.1}$$

where the diameter, the viscosity, the density, and the surface tension of drops are D, μ, ρ, and γ, respectively. The normal impact velocity is V, and the speed of sound is C. Gravity denotes g. Reynolds number (Re) and Weber number (We) represent the ratio of the inertia to the viscous force and capillary force, respectively. Froude number (Fr) is the ratio of the inertia to gravity. Usually for drop impact $Fr \gg 1$, which means that the effect from gravity can be neglected. If Mach number $Ma \approx 1$, it implies that the effect of compressibility of the liquid drop should be considered [38]. In each drop impact event, these dimensionless numbers, especially for Re and We, may change several orders of magnitude during the impact of a single drop. It is difficult to categorize the drop impact process in a single fluid regime (e.g. low Re flow or incompressible flow) due to the fast non-stationary nature of drop impact. As a result, all the factors mentioned above lead to extremely diverse dynamics of drop impact, making drop impact an epitome of the entire field of fluid dynamics.

1.2 Regimes of a Drop Impact Event

Let's consider the case of liquid drops impacting on solid surfaces. Generally, one single event of drop impact can be divided into three regimes over time: the initial impact regime, the spreading regime, and the outcomes at the final stage.

Surprisingly, before a falling drop contacting a surface, the interplay of the drop and surroundings happens. Under the atmospheric condition, when a drop approaches a solid surface, the air pressure below the drop becomes higher and starts to deform the bottom of the drop [39] (Figure 1.5). Then, the air disk is entrapped between the drop and the solid surface, and it rapidly contracts into a central bubble on the substrate to minimize the surface energy [40, 41, 42]. Recently, the clear patterns of how an initial air disc contracts into a bubble were observed through ultra-high-speed imaging and X-ray imaging [43] (Figure 1.6).

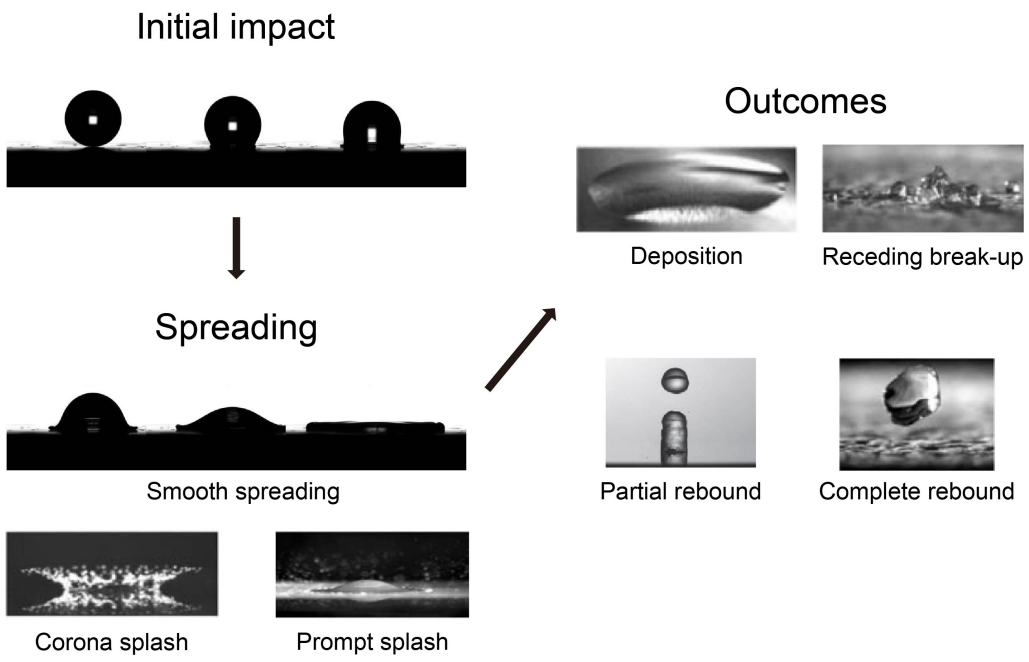

Figure 1.4: Regimes of a liquid drop impacting on a solid surface. The initial impact regime begins as the contact between a impacting drop and a surface. After reaching to the maximum impact force of drop impact, it enters to the spreading regime. Depending on the circumstances, an impacting drop can have different outcomes such as deposition or rebound. Reproduced from Ref. [51]. Courtesy of Begell House Inc.

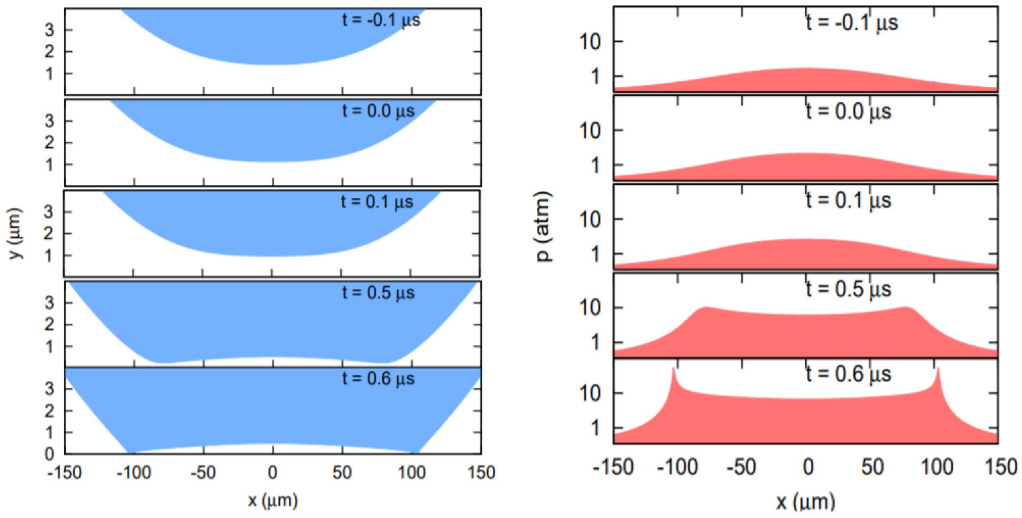

Figure 1.5: Air cushioning effect before the contact of a drop and a substrate. Snapshots from simulations show the temporal evolution of (a) the deformation of the bottom of an impacting drop and (b) the gas pressure within the air layer. Reproduced from Ref. [39] Courtesy of Cambridge University Press.

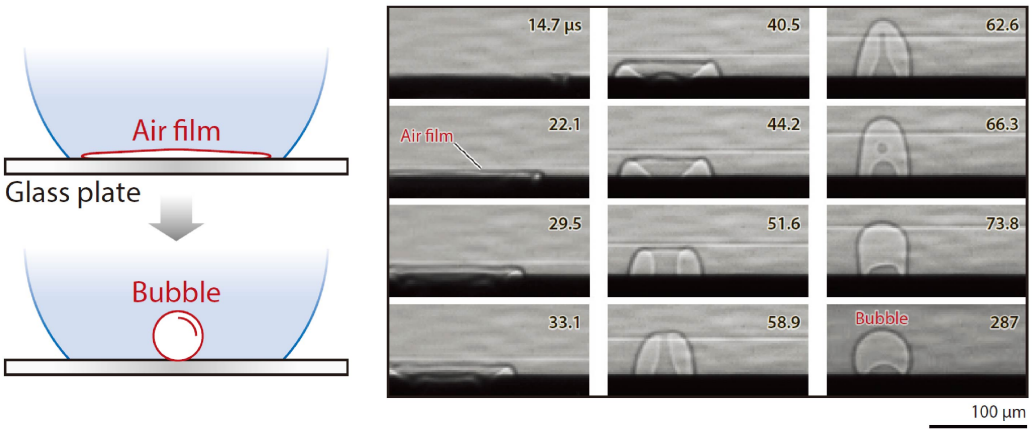

Figure 1.6: The X-ray imaging of the entrapment of an air disc and its contraction into an air bubble over time. Reproduced from Ref. [43]. Courtesy of American Physical Society.

1.2.1 Initial Impact Regime

When a drop falls and just contacts a solid surface, it is the beginning of the initial impact regime. The consideration of the compressibility of the liquid of the drop is important in this regime. The pressure inside the drop rises immediately. The acoustic limit of the pressure equals to the so-called water hammer pressure ρCV over a time duration of RV/C^2, where R is the radius of the drop [38, 44]. Here we mainly focus on drop impact at moderate impact velocities, where impacting drops can be considered as incompressible. Initially, the shape of the drop deforms axisymmetrically. The first contact is nearly like a point, and then the circular wetted contact zone develops. At the very early stage, the drop just looks like a truncated sphere. After that, a thin lamella starts to eject radially along the solid surface, and then the turning point appears (Figure 1.7). The radius of the lamella r_{lm} and the turnung point r_c grow as the scaling $\sqrt{VRt}$, which is proposed by Wagner in the context of the water entry of solid objects [45]. Recently, this scaling has been verified with the theoretical prediction and experimental measurements, showing that $r_c(t) = \sqrt{3VRt}$ [46, 30, 47, 48]. The motion of the lamella propagates roughly with $r_{lm}(t) = \sqrt{4.2VRt}$ fitted by the experimental results [49]. The initial impact regime lasts until the impact force of drop impact reaches the maximum value, and the side wall of the impacting drop is normal to the impacted surface [50], which will be introduced in Section 2. In this regime, merely the base of the drop is deformed. The upper hemisphere of the drop still remains the shape of the dome. The effects of the viscous and capillary force of the drop have not entered this regime.

1.2.2 Spreading Regime

In the spreading regime, the liquid of the drop is still pushed out to spread over the surface. The upper part of the drop begins to deform now, and the liquid expands radially into the lamella until reaching the maximum spreading diameter D_{max}. Besides, a rim is formed at the end of the lamella. At this moment, the inertia competes with the surface tension and the viscosity of the drop. The surface tension tries to pull back the liquid, and the viscosity dissipates the energy. Both of them limit the final D_{max}. It is reported that $D_{max}/D \sim We^{1/4}$ if the inertia balances with the surface tension,

and $D_{max}/D \sim Re^{1/5}$ if the viscous dissipation balances with the kinetic energy [52].

If the kinetic energy of an impacting drop is small, which implies that the impact velocity is very small, the drop just smoothly spreads over the surface. As the impact velocity increases and passes the splashing threshold, the drop would start to splash in this regime eventually. Splashing is defined as the formation of secondary droplets after the impact, and these secondary droplets disintegrate from the rim of the spreading drop. Classically, the splashing threshold can be categorized by the splashing parameter $K_s = We\sqrt{Re}$, which includes the viscosity, the surface tension, and the impact velocity of the drop [53]. Splashing is expected to happen if $K_s \geq 3,000$. However, the splashing threshold not only depends on the impact velocity, but also depends on the surface properties and the ambient pressure, unexpectedly. Xu *et al.* found that reducing the air pressure could suppress splashing [33, 35]. Moreover, splashing also can be suppressed by dropping onto the softer surfaces [30].

1.2.3 Outcomes after Spreading

With the interplay of parameters including Re, We, and the surface properties, there are several outcomes of drop impact [51]. In Section 1.2.2, it has been mentioned that if the kinetic energy of the impacting drop is low, the drop spreads smoothly, and finally it will deposit and stay on the surface. The splashing is promoted by increasing the impact velocity. Then, depending on the surface properties, the drop would retract after reaching the maximum spreading diameter. Particularly, if the substrate is hydrophobic or even superhydrophobic, the retraction would lead to partial rebound, complete rebound, or even jet formation [54, 55, 56] (Figure 1.4).

1.3 Dynamics of Drop impact

So far, drop impact attracts attention progressively, and recent studies have gradually revealed the mystery behind it. Nevertheless, most experiments, theories, and simulations mainly focus on the kinematic features of drop impact, such as the maximum spreading diameter, the splashing threshold, the fingering, and thickness of the expanding sheet, which are mentioned in Section 1.1. Comparably, fewer studies investigate

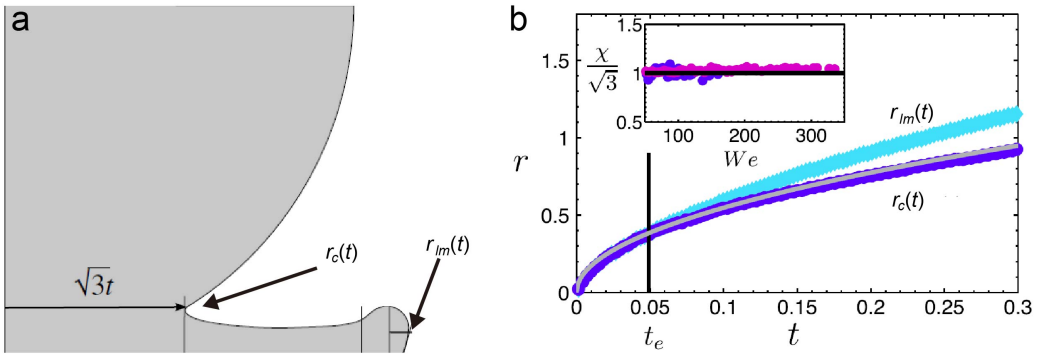

Figure 1.7: The position of the kinematic features of an impacting drop during spreading. (a) Sketch shows a drop spreading on a solid surface. The turning point r_c increases with $r_c = \sqrt{3RVt}$ proposed by Wagner [45]. (b) The experimental data of the radius of the lamella r_{lm} and the turning point r_c with respect to time. r_c follows $\sqrt{3RVt}$. The inset shows the ratio $\chi/\sqrt{3}$, where χ is the coefficient from the fitting of $r_c = \chi\sqrt{RVt}$. Reproduced from Ref. [46, 48]. Courtesy of American Physical Society and Cambridge University Press.

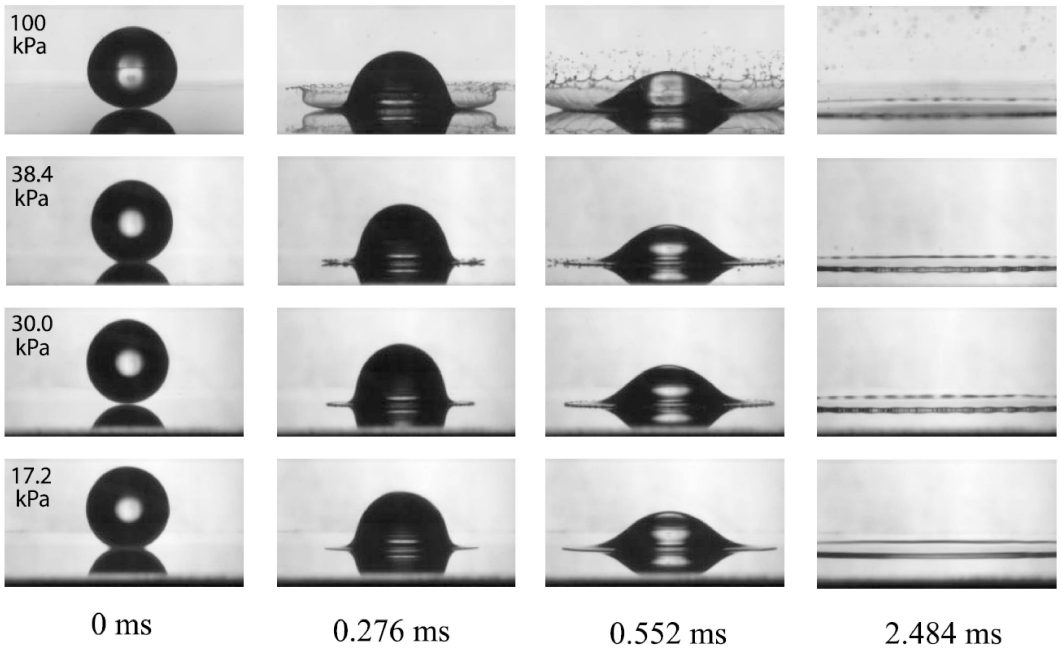

Figure 1.8: Effects of ambient atmosphere pressure to splashing. Drop splashes in the normal atmospheric pressure. As the background pressure decreases, the splashing is suppressed. As the pressure is much lower, no secondary droplets are emitted from the impacting drop. Reproduced from Ref. [33]. Courtesy of American Physical Society.

.

the dynamics of drop impact, especially for the impact force and the stress distribution of drop impact. The impact force and pressure distribution of drop impact play a crucial role in erosion and wear damage, including wear of turbine blades, impact damage to aircraft under rainy condition, surface cleaning, and water cutting [57, 58]. Therefore, understanding the mechanism of the impact force and the stress distribution is important for mitigating the erosion problem during the processes. In addition, the shear stress distribution of drop impact also reveals the development of boundary layer and the change of the flow inside an impacting drop, which are difficult to access by other experimental methods [59, 60, 61, 47].

1.3.1 Impact Force

Impact force is the most studied dynamic quantity of drop impact. Recent theories and simulations propose that the dynamics of drop impact may be controlled by the self-similar process, and deduce the scaling of impact force induced by a liquid drop at the initial impact regime [62, 61, 47]. Recall that initial impact occurs when a liquid drop falls and contacts a surface near $t = 0^+$ with high Re. In this regime, impact of a liquid drop is dominated by inertia. When a drop impacts on a solid surface, the strong pressure gradients develop near the bottom of the drop. The bottom of a drop is deformed rapidly and strongly due to the strong pressure gradients, which also drive the redirection of the flow in the droplet. The direction of the flow changes suddenly from the downward vertical z-direction to the outward radial r-direction in the cylindrical coordinate [63, 47].

Inspired by the classical impact theory, Josserand and Zaleski, Eggers *et al.*, and Philippi *et al.* proposed that the high pressure region occupies a volume with the same radius as the contact area of the drop with the surface, where the self-similar pressure and velocity field establish [62, 61, 47]. The self-similar field propagates within the impacting drop as the impact proceeds. When the front of the self-similar structure reaches the top of the drop, the high-pressure region spreads over the whole drop. The top of the drop would start to decelerate from the original impact velocity. That means, the propagation of the self-similar structure can be examined from the shape of drop. If the front of the self-similar pressure has not reached the top of the drop, the upper part of the drop would remain its original shape as if it does not “feel” the impact. Such a

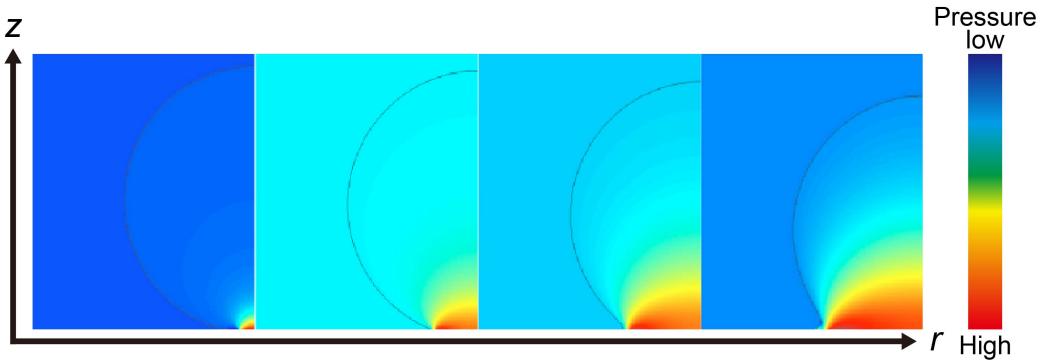

Figure 1.9: Propagation of the self-similar pressure field inside an impacting drop at early times from simulations. In this initial impact regime, the upper part of the drop remains the shape of hemisphere until the pressure field propagates to the apex of the drop. Reproduced from Ref. [61]. Courtesy of AIP Publishing.

counterintuitive prediction can be observed in Figure 1.9.

In addition to the shape of an impacting drop, the self-similar theory also predicts an instantaneous impact force F of drop impact. Philippi and co-workers proposed a model to derive analytical solutions of the impact force induced by drop impact at early times and at the high Re regime. Based on the assumption of inviscid flow motion of a drop, the scalar potential, the structure of the velocity field, and the self-similar pressure can be derived via the analytical derivations [47]. In the high Re limit, the total normal force F by an impacting drop at the early time $t \to 0^+$ is deduced from integrating the pressure on the surface:

$$F(t) = \frac{3}{2}\sqrt{6}\rho V^{5/2} D^{3/2} t^{1/2}. \tag{1.2}$$

In the aspects of experiments, piezoelectric force sensors are frequently used to measure the temporal evolution of the normal impact force of drop impact. Furthermore, with the support of high-speed imaging, the force measurements are synchronized with a high-speed camera in order to simultaneously capture the morphology of the impacting drop and obtain the force signal [64, 65, 66, 50].

In Section 2, we report the verification of the predicted square-root temporal scaling of the impact force through the experiments. Furthermore, the modification of the impact force in the finite Re and the viscoelastic regime is also discussed [66].

1.3.2 Stress Distribution

Although the impact force, which quantifies the average impact pressure, is an important factor in drop impact erosion, the pressure distribution is the determined role in studying damage to substrates. If the total impact force concentrates on a certain small area, the pressure would be high enough and easily damage the substrates. Conversely, if the pressure is distributed more uniform on the substrates, which can minimize the local maximal pressure, the erosion to the substrates can be alleviated. Therefore, depending on different conditions, we can tune the pressure distribution of drop impact based on the needs, i.e. higher pressure induced by drop impact for waterjet cutting, or lower pressure of drop impact for preventing erosion to substrates in spray coating. Therefore, measuring and controlling the pressure distribution of drop impact are necessary and

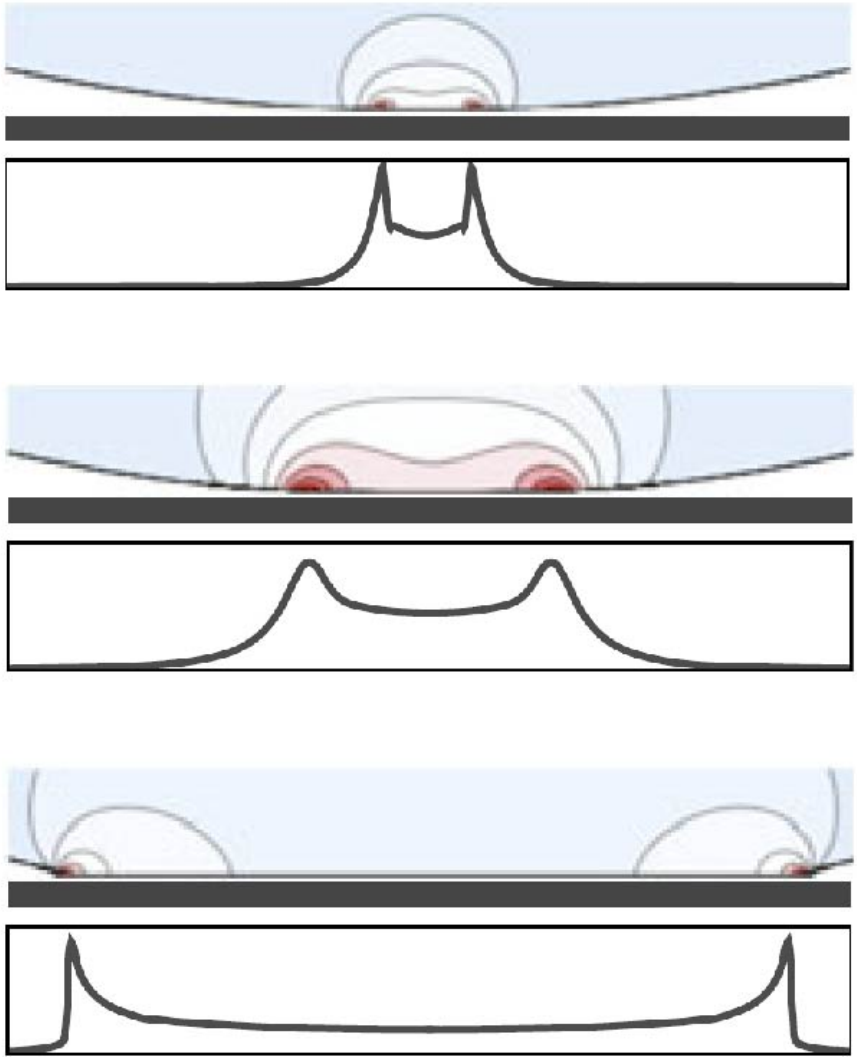

Figure 1.10: Pressure distribution of drop impact. Time series showing the development of the pressure field (top panels), as well as the pressure exerted by the impacting drop on the solid surface (bottom panels). Reproduced from Ref. [47]. Courtesy of Cambridge University Press.

vital for industrial applications of drop impact.

The pressure distribution of drop impact in early time was first identified by Josserand and Zaleski [62], who showed a pressure field developed inside a drop. The self-similar scaling in the early impact regime shows that $p \sim \rho V^{3/2} D^{1/2} t^{-1/2}$. Recently, with the progress of simulation, the detailed structure of the pressure field near the contact zone is revealed [62, 47]. As shown in Figure 1.10, the simulations show the complex structures of the pressure fields inside a drop impacting on a solid surface at early times. The pressure distribution counterintuitively exhibits the sharp maxima near the contact line $r(t) = \sqrt{3RVt}$ during the impact. The singular structure of the pressure distribution over the contact area shows

$$p(t) = \frac{3\sqrt{2}}{2\pi} \frac{\rho V^2 D}{\sqrt{3VDt - 2r^2}}. \tag{1.3}$$

It reveals a finite-time singularity at the turning line r_c away from the impact axis, and it predicts an annular ring of divergent pressure propagating radially with the turning line.

At high Re and We, the viscous boundary layer is thin, and the thickness of the boundary layer l_v scales as $l_v \sim \sqrt{t/Re}$. Pressure gradients across this thin viscous boundary layer are small. Hence, to the first order, the pressure distribution is not affected by the viscous boundary layer. Nevertheless, the boundary layer plays the essential role for the shear stress on impacted surfaces. Ignoring the viscous boundary layer would lead to zero shear stress and significantly reduce the erosion capability of impacting drops [67].

In the initial impact regime, Philippi *et al.* hypothesized that the structure of the viscous boundary layer of drop impact is similar to that of the shock-wave-induced boundary layer [47]. Here, the turning line of an impacting drop is analogous to a shock front with a growing viscous boundary layer trailing behind. Based on the classic shock-wave solution [68], they obtained the velocity profile within the boundary layer and calculated the shear stress distribution along the contact surface:

$$\tau(r,t) = \mu \frac{\partial v_r(r, z=0, t)}{\partial z} = \frac{\sqrt{6}\rho^{1/2} V^{3/2} D^{1/2} \mu^{1/2}}{\pi^{3/2}} \frac{2r}{3VDt - 2r^2}, \tag{1.4}$$

where v_r is the radial velocity of the flow inside an impacting drop. Similar to the pressure distribution (Equation 1.3), the shear stress also exhibits a finite-time singularity at the turning line $r_c(t)$. The formula agrees well with numerical simulations away from the singularity. A small cutoff Δ was found near the turning line, below which the $1/r$ singularity is screened. By integrating the shear stress over the contact area, they also derived the magnitude of the drag force F_d induced by drop impact in the early impact regime:

$$F_d(t) = \int_0^{2\pi} \int_0^{r_0-\Delta} \tau(r,t) r dr d\theta = 5.35 \mu^{1/2} \rho^{1/2} V^2 D t^{1/2}, \tag{1.5}$$

where $\Delta = 0.02\sqrt{VDt}$ is chosen based on numerical findings at different Re.

Experimental measurements on the transient pressure and shear stress distribution underneath millimeter-sized drops with micron spatial resolutions and sub-millisecond temporal resolutions are clearly difficult. There are only few studies that experimentally measured the stress distribution of drop impact. At an earlier time, Hartley *et al.* used hot-film anemometry to experimentally measure the shear stress of drop impact on the bottom surface of a water flume [69, 70]. A slow horizontal base flow has to be imposed in the flume in order to maintain a constant fluid temperature over the hot-film sensor in their experiments (Figure 1.11(a)). The result qualitatively agrees with the empirical relations from their numerical simulations. However, this method restricts the condition that there should be a layer of water on the substrates.

In recent years, Thanh-Vinh *et al.* introduced a method to obtain the pressure distribution by using a cantilever array of force sensors (Figure 1.11(b)) [71, 72]. Although the rough patterns of pressure distribution can be measured, the spatial resolution is not quite enough to observe the detailed structures near the contact line because of the finite sizes of the force sensors. In addition, the cantilever array of piezoresistors results in microstructure surfaces, limiting the possibility of exploring drop impact on surfaces with different controlled surface textures. Based on the discussions above, it is desirable to develop another technique which can be widely applied to measure the stress distribution of drop impact under any condition.

In Section 3, we conduct the novel technique "high-speed stress microscopy." By combing the ideas from laser sheet microscopy, high-speed photography, and traction

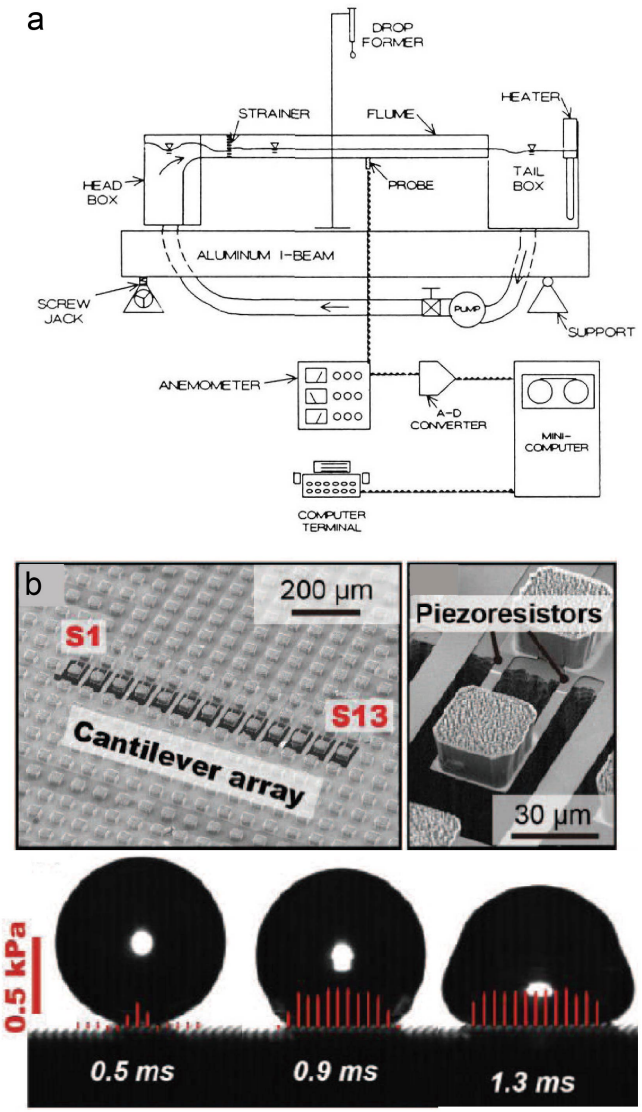

Figure 1.11: (a) Experimentally measured the shear stress of drop impact on the bottom surface of a water flume by using using hot-film anemometry. (b) Experimental measurements of the pressure distribution of drop impact through an array of mirco-piezoelectrical force sensors Reproduced from Ref. [71, 70]. Courtesy of Taylor & Francis and 2016 IEEE.

force microscopy, we can map the temporal evolution of the shear stress and the pressure distribution of drop impact—the key dynamic factors responsible for erosion to substrates.

Moreover, the development of high-speed stress microscopy helps us to investigate more advanced and complicated conditions of the stress distribution of drop impact. In Section 4, we synthesize the solid substrate with arrays of micropillars on its surface. How the microstructure would affect the shear stress and shear force is a crucial issue, and this problem has never been approached through any experiment.

Chapter 2

Impact Force of Drop Impact

This chapter is based on the publication: Leonardo Gordillo, Ting-Pi Sun, and Xiang Cheng. Dynamics of drop impact on solid surfaces: evolution of impact force and self-similar spreading. *Journal of Fluid Mechanics*, 840:190-214, 2018. [66]

Leonardo Gordillo and Xiang Cheng designed the project and conducted the theories. Leonardo Gordillo also conducted the experimental measurements. Ting-Pi Sun discussed and analyzed the experimental data.

2.1 Introduction

The elegant and ephemeral dynamics of liquid-drop impacts on solid surfaces have attracted scientists for generations. Since Worthington's first sketches [24], this deceivingly simple phenomenon have unfolded into one of the richest fields in fluid mechanics [16, 27, 25, 26]. Thanks to the rapid development of high-speed imaging and numerical simulation techniques in the last 15 years, a clear picture on liquid-drop impacts gradually emerges. Different regimes during drop impacts have been resolved, each describing a specific spatiotemporal feature. Processes such as lamella ejection and splashing [33, 46], maximum spreading [36, 52, 73], receding and rebound [74, 4], corona fingering [75, 76] and air cushioning [77, 78, 79] have been extensively studied. Among all these features, the impact force of liquid drops leads to arguably the most important consequence of impact events. This mechanical outcome of impacts is directly responsible for numerous natural and industrial processes including soil erosion [80], the formation

of granular craters [4, 6] and atmospheric aerosols [2] and the damage of engineered surfaces [81, 82]. The impact force of raindrops is also of vital importance to many living organisms exposed to the element [83, 84, 85]. Nevertheless, compared with the large number of studies on the morphology of impacting liquid drops, comparatively fewer experiments have been conducted to investigate the impact force of liquid drops. Most of the existing works have focused on the maximum impact force of liquid drops [80, 86, 64, 65, 87]. The temporal evolution of impact forces during impacts remains largely unexplored.

The complexity of drop-impact dynamics, with the evolution of impact forces as a specific example, arises from the interplay of various competing factors and the rapid and continuous change of their relative importance during a drop impact. Dimensionless numbers such as Mach (impact velocity/sound speed), Reynolds (inertial/viscous forces), Weber (inertial/capillary forces) and Froude (inertial/gravity forces) numbers may change several orders of magnitude in a single drop-impact event, making it a miniature of many branches of fluid mechanics [88, 59, 47, 89]. In spite of this complexity, pioneering theories have shown that drop-impact dynamics over a wide range of dimensionless numbers may be controlled by simple self-similar processes [59, 61, 47]. Identifying these self-similar processes will not only reduce mathematical difficulties at localised spatiotemporal scales, but also bridge separate impacting regimes into a coherent structure [90]. Unfortunately, exact or even approximate self-similar solutions are hard to spot in drop impacts. Most of studies rely on simple dimensional analyses [16, 27, 26], which are useful in determining asymptotic scaling relations but fail to reveal the underlying self-similar mechanisms in play.

In this section, we conduct systematic experiments on the temporal evolution of impact forces over a wide range of Reynolds numbers (Re). Built on the recent self-similar theory by Philippi and co-workers [47], we develop a quantitative understanding of the early-time scaling of impact forces over five decades of Re across inertial, viscous and viscoelastic regimes. Through this study, we experimentally verify the existence of an upward propagating self-similar structure during the initial impact of liquid drops at high Re [61, 47]. Our quantitative analysis on the temporal variation of impact forces also predicts the maximum impact force and the associated peak time as a function of Re, which have been extensively studied in experiments [80, 86, 64, 65, 87]. As such,

our experiments on the temporal evolution of impact forces provide a benchmark for verifying numerical and theoretical models of drop-impact dynamics. Our theoretical analysis constructs a unifying framework for understanding the early-time evolution of impact forces in different impact regimes.

2.2 Methods

2.2.1 Experimental Setup

The experimental setup of measuring impact force of drop impact are shown in Figure 2.1. The drops with a fixed diameter $D = 2.2 \pm 0.1$ mm was generated by a syringe pump. The drops were made of silicone oils with a wide range of viscosities $\nu = 10^{-1}$ - 10^{-6} cSt, and the density $\rho = 971$ kg/m^3 (Sigma-Aldrich). The drops were released from different heights, yielding different impact velocities U_0 ranging from 1.4 to 3.0 m/s. The drops impacted onto the piezoelectric force sensor of the diameter 15 mm (PCB Piezoelectronics 106B51) with a force resolution of 0.3 mN and a time resolution of 10 µs. The force signal from the piezoelectric force sensor passed through a signal conditioner and was recorded by an oscilloscope. To reduce the noises and oscillations, we performed the minimal data smoothing with moving averages of three adjacent data points. The high-speed photography was performed with 50,000 frames per second (Photron SA-X2). A photo-interrupter was triggered by falling drops in order to synchronize the high-speed imaging and force measurements. Therefore we can simultaneously probe the kinematics and dynamics of drop impacts. The light source for high-speed imaging is provided by the LED with high lumens.

2.2.2 Validation of Impact Force Measurements

To verify the experimental method for measuring impact forces via a piezoelectric force sensor, we have conducted two independent tests. First, we measure the temporal evolution of the impact force of elastic solid spheres, a well-known result in contact mechanism [91]. When a non-adhesive elastic sphere of radius R impacts on an infinite elastic plane, the impact force F is governed by the classical Hertzian contact:

$$F = \frac{3}{4} E^* R^{1/2} d^{2/3}, \tag{2.1}$$

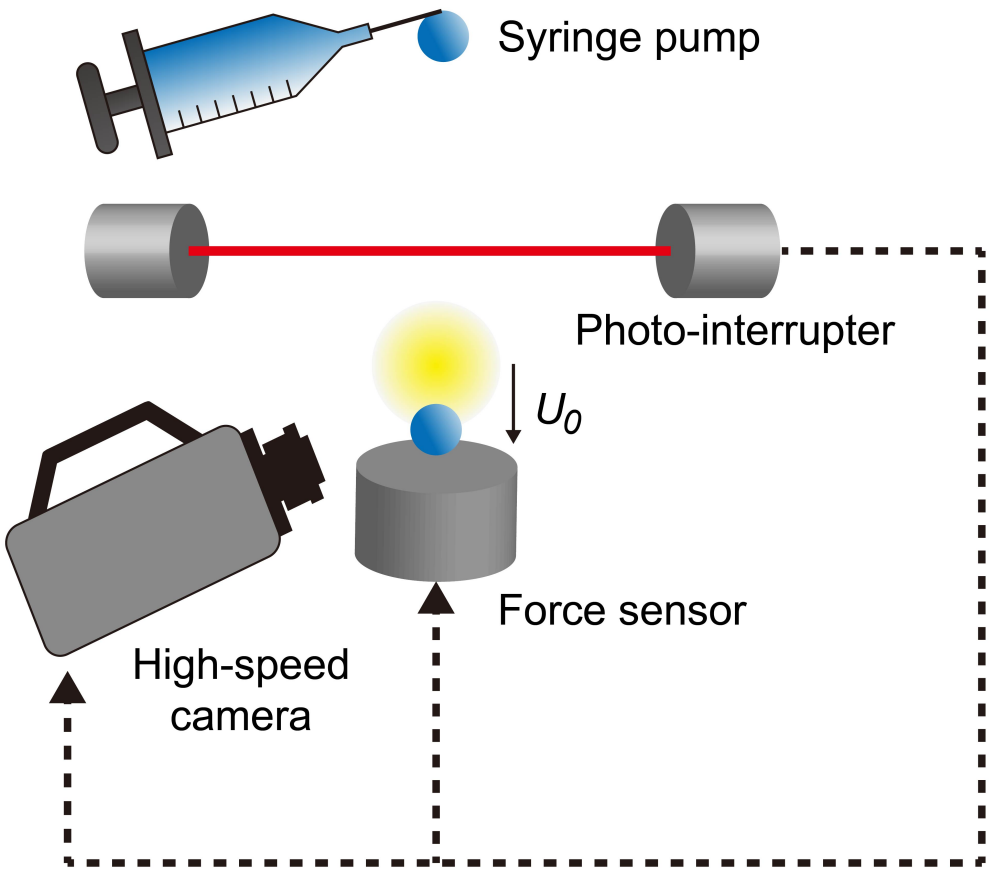

Figure 2.1: Schematic diagram of the experimental setup for measuring the impact force of drop impact. The force sensor is synchronized with the high-speed camera. Once the impacting drop passes through the photo-interrupter, the measurement will be activated automatically.

where

$$\frac{1}{E^*} = \frac{1-\nu_1^2}{E_1} + \frac{1-\nu_2^2}{E_2}. \tag{2.2}$$

Here, E_1 and E_2 are the elastic moduli and ν_1 and ν_2 are the Poisson's ratios of the elastic solid sphere and the surface of the piezoelectric force sensor, respectively. If d is the displacement of the sphere. At the initial impact $t \to 0$, $d = U_0 t$. Then we replace d in Equation 2.2 and it becomes

$$F = \frac{3}{4} E^* R^{\frac{1}{2}} d^{2/3} U_0^{2/3}. \tag{2.3}$$

In this experiment, we used the material of neoprene rubber as the impacting solid sphere, with the properties of $E_1 = 12.33$ MPa, $\rho = 1230$ kg/m^3, and ν_1=0.499. E_1 is measured by using a TA RSA-G2 Solids Analyzer. The radius and impact velocity of the sphere are $R = 2.2$ mm and $U_0 = 0.4$ m/s, respectively. Since the surface of the force sensor which is made of stainless steel is much harder than the neoprene rubber sphere, which means that $(1-\nu_2^2)/E_2 \ll (1-\nu_1^2/E_1)$. Equation 2.2 can be reduced to $E^* = E_1/(1-\nu_1^2)$. Figure 2.2 shows the experimental temporal evolution of the impact force of the rubber sphere. At the initial impact regime, the impact force follows the power law of $F \sim t^{\frac{2}{3}}$, which is consistent with the Hertzian contact theory.

Second, we also examine whether the impact process obeys the conservation of momentum. That is, the change of momentum Δp equals to the impulse J, which is obtained by numerically integrating the impact force of liquid drops over time:

$$\Delta P = J = \int_0^\infty F(t) dt. \tag{2.4}$$

The results of the change of momentum and the impulse quantitatively matches with each other (Figure 2.2).

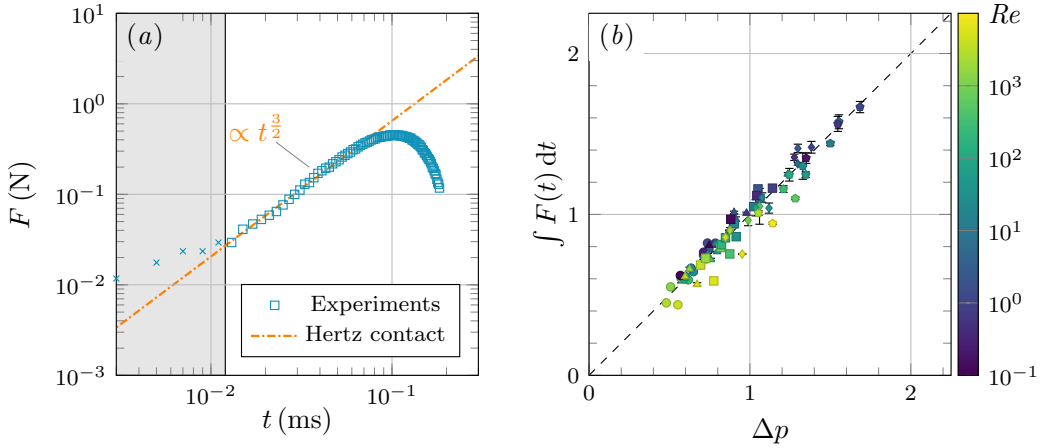

Figure 2.2: Validation of our experimental method. (a) Temporal evolution of the impact force of a neoprene rubber ball with $D = 4.5$ mm and $U_0 = 0.4$ m/s. The impact force scales as $t^{3/2}$ near $t = 0^+$ as predicted by the Hertz-contact theory [91]. The shaded area indicates the rise time of the force sensor. (b) The impulse of impacts, $J = \int_0^\infty F\mathrm{d}t$, versus the momentum of liquid drops, $\Delta p = mU_0$, where $m = \pi\rho D^3/6$ is the mass of liquid drops. The dashed line indicates $J = \Delta p$ as requested by momentum conservation.

2.3 Results and Discussion

2.3.1 Temporal Evolution of the Shapes of Drops

Figure 2.3 shows a representative data illustrating simultaneous measurements of the shape and the impact force of drop impacts. A liquid drop impacts on the surface at the time $t = 0$. The temporal evolution of the shapes of the impacting drop is quantified by measuring the height of the drop $h_{max}(t)$ and the radius of the spreading contact line $r_0(t)$. In the early time, r_0 follows a $t^{\frac{1}{2}}$ scaling which is indicated by the green dotted line, which confirms the scaling of previous theoretical studies $r \sim \sqrt{U_0 D t}$.

In the other hand, the slope of h_{max} versus t matches with the initial velocity $-U_0$ which is indicated by the blue dashed line. This result supports the theory of the existence of the propagating self-similar region. Before t_{max}, which is the time that the impact force reaches to a maximum, the front of the self-similar region has not reached to the top of the drop; hence, the motion of the drop's apex h_{max} travels with the initial velocity $-U_0$ without any change, as if it does not feel the impact happens. The snapshots of Figure 2.3 demonstrates that the shape of the upper part of the drop remains unchanged before t_{max}, and it also confirms the previous result of simulation in Figure 1.9.

2.3.2 Temporal Evolution of the Impact Force at the High *Re* Regime

Based on the temporal signature of the impact force, the dynamics of the impact force can be divided into two regimes: (1) the time before t_{max} called the initial impact regime and (2) the time after t_{max} called inertia-driven spreading regime. In the following discussion of the impact force, we will focus on the initial impact regime.

First, we investigate the dynamics of impacting drops during the time near $t \to 0^+$ at high Reynolds numbers Re, where Re is defined as $Re \equiv U_0 D/\nu$. In this limit, the impact of liquid drops is dominated by inertia. Upon the impact, the strong pressure gradients develop near the contact region of the solid surface. The strong deformation of the bottom of the drop make the flow inside the drop redirect from the vertical (z) direction to the radial (r) direction. In analogy to the classical impact theory [45], simulations and a recent theory have shown that the region of the large pressure gradients concentrates within a small volume of the impacting drop next to the contact

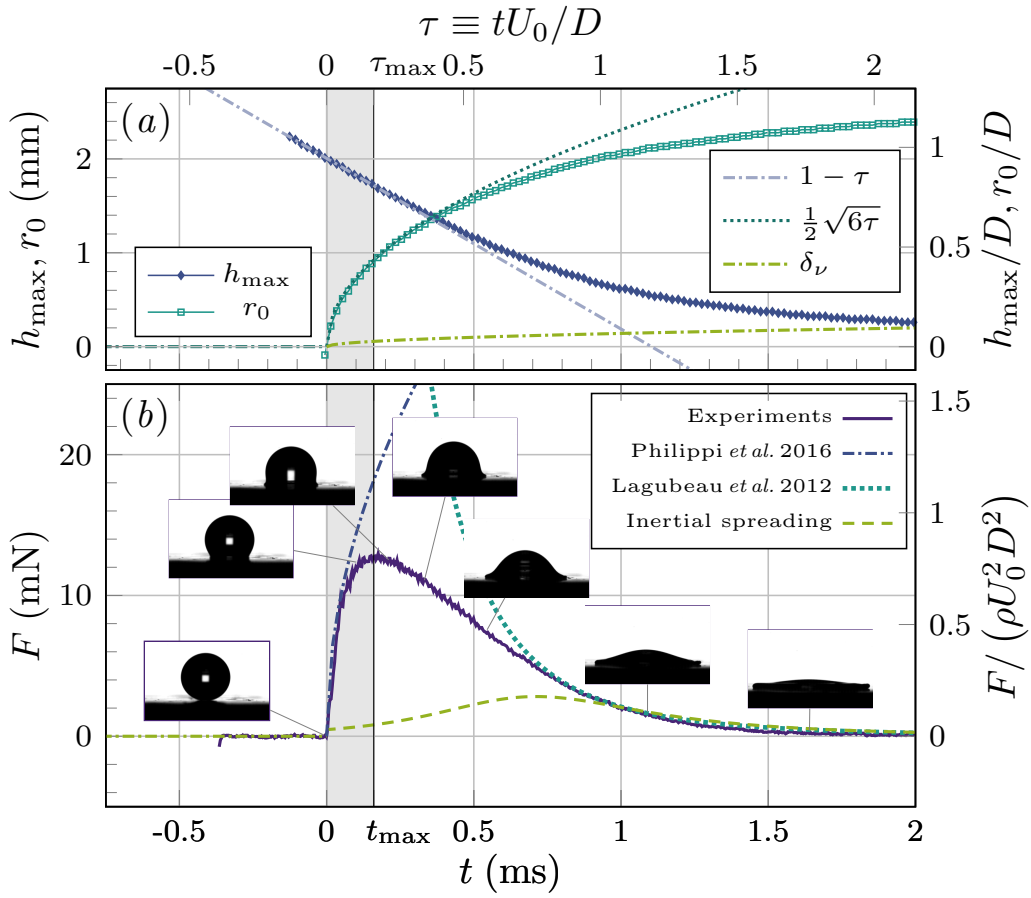

Figure 2.3: Simultaneous measurement of the kinematics and dynamics of the impact of a liquid drop with $\nu = 20$ cSt and $U_0 = 1.93\,\mathrm{m/s}$ ($Re = 212$). (a) Temporal evolution of the shape of the impacting drop, quantified by the height of the drop, $h_{\max}(t)$, and the radius of the spreading contact line, $r_0(t)$. The lower axis indicates t in unit of milliseconds. The upper axis indicates the dimensionless time τ. The thickness of the boundary layer, δ_ν, is calculated and shown by the curved dash-dotted line near the bottom. The linear dash-dotted line has a slope of $-U_0$ (or -1 in the dimensionless form), indicating the trajectory of the drop as if the impact never occurred. The dotted line indicates the $\sqrt{t}$ scaling of r_0. (b) Temporal evolution of the impact force of the impacting drop, $F(t)$. The dash-dotted line on the left is the prediction of the self-similar theory of initial impacts (Equation 2.5) [47]. The upper dotted line on the right is the prediction of the self-similar solution of drop spreading by Eggers and coworkers [61, 92]. The lower dashed line on the right is the prediction of our self-similar solution of drop spreading. The corresponding snapshots of the impacting drop from high-speed imaging are shown next to the curve. The regime of the initial impact is indicated by a shaded area spanning from 0 to $t_{\max}$. A small DC offset from the force sensor at $t \gg 1$ was removed from the raw data.

area, where self-similar pressure and velocity fields establish [47]. The length scale of the self-similar fields is given by $\sqrt{U_0 Dt}$ (Section A.1). The self-similar pressure from the theory gives rise to an instantaneous impact force as the function of time following [47]:

$$F(t) = \frac{3}{2}\sqrt{6}\rho U_0^{5/2} D^{3/2} t^{1/2}. \tag{2.5}$$

Or in the dimensionless form:

$$\tilde{F}(\tau) = \frac{3}{2}\sqrt{6}\tau^{1/2}, \tag{2.6}$$

where the dimensionless force $\tilde{F} \equiv F/\rho D^2 U_0^2$, and the dimensionless time $\tau \equiv t/(D/U_0)$.

Equation 2.5 can also be understood by the following scaling argument. During the impact, the deformation of the drop is limited in the self-similar pressure region. The volume of the self-similar occupies the same radius with the contact area between the drop and the solid surface [61]. Indeed, the previous theories and our experiments all have confirmed that the radius of the spreading contact line increases as $r \sim \sqrt{U_0 Dt}$ at short times during the initial impact regime (Figure 2.3) [49, 93, 46, 47], quantitatively similar to the length scale of the self-similar fields shown above. Therefore, we can approximate the volume of the self-similar pressure region increases with $V \sim (U_0 Dt)^{\frac{3}{2}}$. From the conservation of momentum, in order to balance the impulse of the impact force and the change of the momentum of the drop, the impact force can be written as

$$F(t) = \frac{\rho V U_0}{t} \sim \rho U_0^{5/2} D^{3/2} t^{1/2}. \tag{2.7}$$

We experimentally verify the prediction of the initial-impact self-similar theory by first plotting the impact forces at different Re in a log-log plot (Figure 2.4). To reveal the predicted $t^{1/2}$ scaling at short times, we divide the dimensionless force, $\tilde{F}$, by $\tau^{1/2}$. For the sake of clarity, we also multiply the rescaled forces by a time-independent factor, $Re^{2/5}$, which shifts the curves vertically to avoid overlap. Figure 2.4 shows that the early-time evolution of impact forces follows the predicted $\tau^{1/2}$ scaling at high Re, where $\tilde{F}/\tau^{1/2}$ is independent of τ for about one decade of time.

The data shown in Figure 2.4 represent only a small subset of our more than 200 independent experimental runs at different Re. To quantify all our measurements, we fit $\tilde{F}$ as a function of τ at short times using a power-law dependence, $\tilde{F} = \alpha\tau^{\beta}$. The

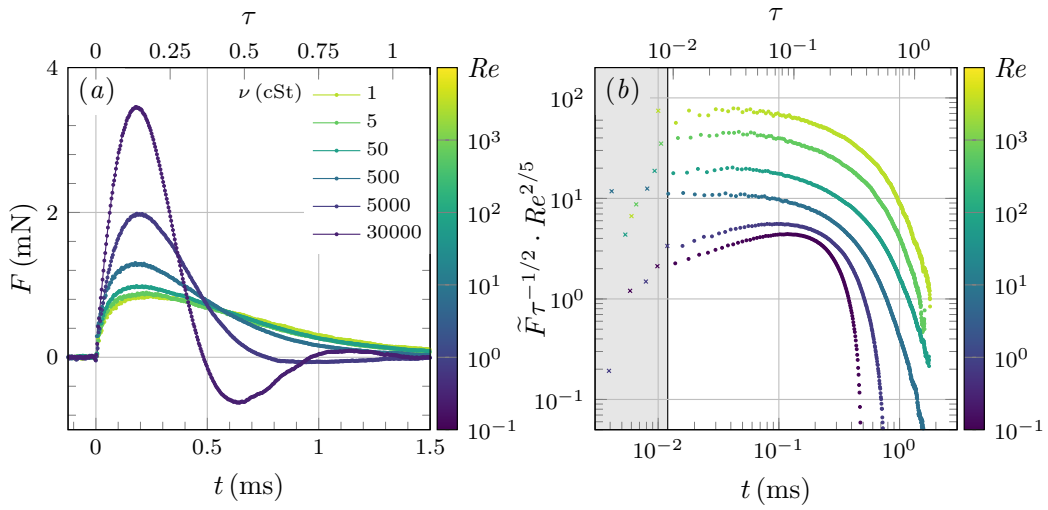

Figure 2.4: Impact force of liquid drops. (a) Temporal evolution of the impact force of liquid drops at different Re. In the order of the maximum impact force, from high to low, the Reynolds numbers of the curves are 0.10, 0.72, 6.90, 66.18, 665.52 and 3219.29, respectively. The viscosities of the drops are indicated in the legend. (b) Rescaled dimensionless force, $\widetilde{F}/\tau^{1/2}$, as a function of time, where $\widetilde{F}$ and τ are the dimensionless force and time, respectively. A time-independent factor, $Re^{2/5}$, is introduced to separate the curves vertically for clarity. The grey region indicates the rise time of the force sensor, which sets the time resolution of our measurements. The Reynolds numbers and viscosities of the curves are the same as those in (a).

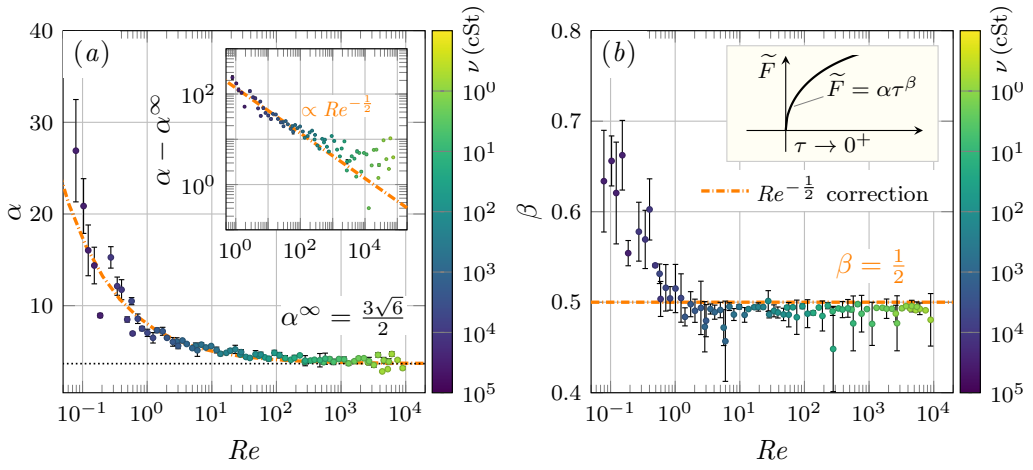

Figure 2.5: The early-time scaling of impact forces, $\widetilde{F}(\tau) = \alpha\tau^{\beta}$, near $\tau = 0^{+}$ over a wide range of Re. (a) The coefficient of the scaling, α, and (b) the exponent of the scaling, β. The range of the power-law fittings spans over one decade of time starting from $\tau = 0^{+}$. The horizontal dotted line in (a) indicates the asymptotic value $\alpha^{\infty} = 3\sqrt{6}/2$ predicted by the self-similar theory at the high-Re limit [47]. The dash-dotted lines show our model prediction $\alpha(Re)$ and $\beta(Re)$ (Equation 2.21). The colour bars on the right of each plot indicate the viscosity of the liquid drops used in each experiment. The inset of (a) shows $(\alpha - \alpha^{\infty})$ as a function of Re and our theoretical prediction in a log-log scale.

exponent β as a function of Re for all our measurements is shown in Figure 2.5(b). β reaches a plateau close to 1/2 when $Re > 0.7$. The coefficient α also approaches a constant $\alpha^{\infty} = 4.7 \pm 0.7$, close to the theoretical prediction $3\sqrt{6}/2$ in Equation 2.6, but only when $Re > 200$ (Figure 2.5(a)). Thus, in combination, our measurements on the early-time evolution of impact forces quantitatively verify the initial-impact self-similar theory at high Re above 200.

The existence of upward expanding self-similar fields during the initial impact of a high-Re liquid drop can also be seen from the shape of the impacting drop. Before the upper bound of the self-similar high-pressure region, marked by the isobar of some preset high pressure, reaches the top surface of the liquid drop, the motion of the drop apex should remain unchanged as if the drop had not experienced any impact at all. Such a counterintuitive hypothesis has indeed already been implied by Worthington's original sketch [24] and quantitatively verified by much more recent simulations [61, 59, 47] and experiments [36, 92]. Here, our simultaneous measurements of the shape and impact force of liquid drops provide further evidence that this unusual phenomenon arises from the finite propagation speed of the self-similar fields. As shown in Figure 2.3, in the regime where $F(t)$ follows the prediction of Equation 2.5, the apex of the drop, $h_{\max}$, keeps traveling at the initial impact velocity U_0 without any perceptible changes. Since the shape of the self-similar region—specifically the isobar of the self-similar pressure field—does not necessarily conform to the shape of the drop, the pressure field may touch the upper surface of the drop before reaching the apex. As a result, the impact force may start to deviate from the prediction of the initial-impact self-similar theory, when $h_{\max}$ is still outside the self-similar region and maintains its constant-velocity descent. This is indeed consistent with our observations (Figure 2.3). The impact force reaches its maximum and begins to decrease before the apex of the drop shows any clear deviation from U_0. Thus, it is more appropriate to use the peak time, $\tau_{\max}$, i.e. the time when $\tilde{F}$ reaches the maximum, to mark the end of the initial impact regime. In practical terms, the maximum force is easier to identify than the deviation of the drop apex from its linear descent, which relies on the derivative of $h_{\max}(t)$.

The peak time, $\tau_{\max}$, therefore, provides a proper time scale to estimate the average expanding speed of the self-similar fields. A more quantitative analysis of $\tau_{\max}$ based on the propagation of isobars will be provided in Section 2.3.3 below. We plot $\tau_{\max}$ and the

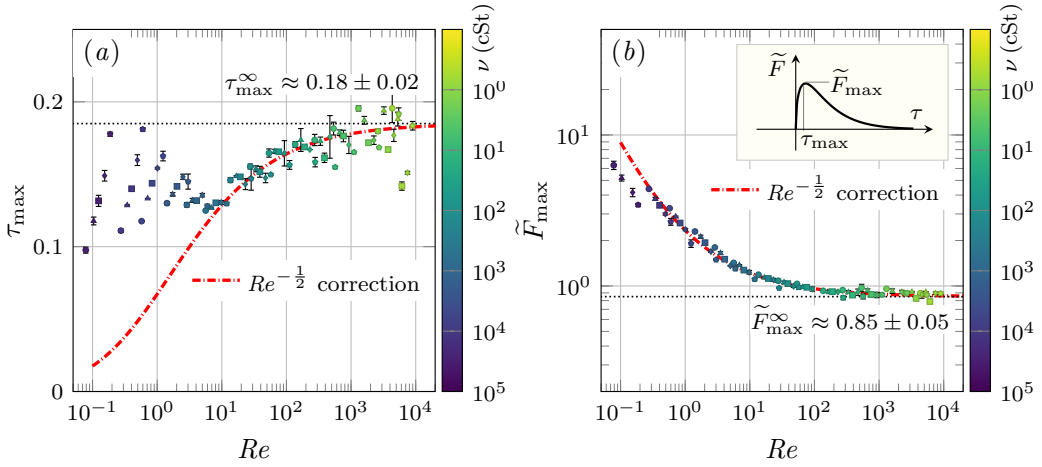

Figure 2.6: The maximum impact force and the associated peak time. (a) shows the dimensionless peak time, $\tau_{\max} \equiv t_{\max} U_0/D$, and (b) shows the dimensionless maximum impact force, $\widetilde{F}_{\max} \equiv F_{\max}/\left(\rho D^2 U_0^2\right)$, over five decades of Re. The asymptotic values at the high Re limit, $\tau_{\max}^{\infty}$ and $\widetilde{F}_{\max}^{\infty}$, are indicated by the horizontal dashed lines in each plot, which are obtained experimentally by averaging all the data with $Re > 10^3$. The dash-dotted lines are our model predictions given by Equation 2.22 and Equation 2.24. The colour bars on the right indicate the viscosity of liquid drops.

maximum impact force, $\widetilde{F}_{\max}$, as a function of Re in Figures 2.6(a),(b), respectively. The value of $\tau_{\max}$ approaches a constant $\tau_{\max}^{\infty} = 0.18 \pm 0.05$ at the high Re limit. Since the drop does not deform significantly during the initial impact, the average expanding speed of the self-similar fields at the high-Re limit can be simply estimated as $U_{\mathrm{self-similar}} = D/t_{\max} = U_0/\tau_{\max} \approx 5.5U_0$, which ranges from 7.7 up to 16.5 m/s in our experiments. Compared with the speed of sound, this relatively small speed demonstrates that the boundaries of the self-similar fields are not shock fronts induced by the compressibility of liquid drops. Accordingly, $F_{\max}$ should scale with the inertial force, $\rho D^2 U_0^2$, instead of the water-hammer force, $\rho D^2 c U_0$, where c is the speed of sound in the liquid. This argument is indeed supported by both previous studies [86, 65, 87] and our experiments (Figure 2.6(b)). Thus, the maximum impact force of subsonic liquid drops at high Re, relevant to most natural and industrial processes, arises from the development of upward expanding self-similar pressure fields, rather than water-hammer pressures assumed in several recent studies [94, 95, 71].

Lastly, it is worth discussing the effect of ambient air on impact forces. Air cushioning has been the focus of many recent studies [26]. Although the ambient air can profoundly affect the dynamics of drop impacts such as the formation of liquid sheets and splashing [33, 46], the numerical work of Philippi and co-workers showed that the impact pressure varies smoothly across the air-liquid interface of the air-cushion layer underneath impacting drops, indicating the transparency of air cushioning to the impact pressure [47]. Indeed, their study showed that the early-time $t^{1/2}$ scaling of the impact force is invariant in the presence of ambient air after they introduced a small time shift, t^*, to account for the delay of the impact moment due to cushioning. We estimate the magnitude of t^* in our experiments as follows. By balancing the air pressure with the inertial pressure of the impinging drop, Mani and co-workers showed that the characteristic thickness of the air-cushion layer is $H = RSt^{2/3}$, where $R = D/2$ is the radius of the drop and $St = \mu_g/(\rho U_0 R)$ is the inverse of the Stokes number with μ_g as the air viscosity [39]. Thus, the air-cushion time t^* can be estimated as $t^* = H/U_0$. Using the relevant parameters of our experiments, we find $t^* = 0.12 \sim 0.41$ μs, consistent with numerical simulations [39]. Since t^* is about two orders of magnitude smaller than the temporal resolution of our force sensor (Figure 2.4(b)), the presence of t^* should not affect the early-time scaling of our experiments. Furthermore, it has been shown

that the impact pressure underneath an impacting drop concentrates near the moving contact line [47], where air cushioning is weak or absent [77, 78]. Since the impact force is an integral of the impact pressure over the entire contact area, which is dominated by the high pressure near the contact line, air cushioning should not strongly affect the impact force measured in our experiments. Our measurements indeed show the $t^{1/2}$ scaling predicted by the initial-impact self-similar theory without ambient air, directly confirming the weak effect of air cushioning on the early-time scaling of impact forces. It should be noted that although we cannot directly detect the effect of air cushioning due to the finite time resolution of our force measurements, the existence of the trapped air layer prevents the formation of water-hammer pressures at the very early time of impacts within t^* [39].

2.3.3 Temporal Evolution of the Impact Force at the Finite Re Regime

Next, we investigate the early-time scaling of the impact force of viscous drops, $\widetilde{F} = \alpha\tau^{\beta}$, near $\tau = 0^+$ at finite Re. As shown in Figure 2.5, the coefficient α starts to deviate from the high-Re plateau when $Re < 200$, where α increases with decreasing Re. In contrast, the exponent β maintains at $1/2$ until $Re \approx 0.7$ and then quickly increases at even lower Re. In this section, we shall focus on impact forces, $\widetilde{F}(\tau)$, in the intermediate Re regime with $0.7 < Re < 200$ and leave the discussion of $\widetilde{F}(\tau)$ at even lower $Re < 0.7$ in the next section.

Before delving into rigorous calculations, it is instructive to consider a simple scaling for impact forces at finite Re. At finite Re, viscous forces cannot be ignored when determining the dynamics of drop impacts. The distance traveled by the centre of an impacting drop can be approximated as $d \approx U_0 t$ at short times. Based on a simple geometric arguments, the radius of the contact area between the drop and the solid surface is given by $r_0 = \sqrt{dD} = \sqrt{U_0 D t}$, as we have already confirmed previously (Figure 2.3(a)). Assume the vertical velocity decreases from the impact velocity U_0 to zero over a length l within the drop above the solid surface. Again, by simply balancing the impulse of the impact force with the change of the momentum of the deformed drop, we have

$$F(t) = \frac{\rho V U_0}{t} \sim \frac{\rho r_0^2 l U_0}{t}, \tag{2.8}$$

where $V \sim r_0^2 l$ is the volume of the part of the liquid drop that significantly deforms. At high Re, l is determined by the self-similar velocity field with $l \sim \sqrt{U_0 D t}$. Equation 2.8 restores to the previous scaling Equation 2.7. At finite Re, the boundary layer developed at the bottom of the impacting drop introduces a new length scale $\delta_\nu \approx \sqrt{\nu t}$, which competes with the growth of the self-similar field that scales as $\sqrt{U_0 D t}$. If we set $l \approx \delta_\nu$ in Equation 2.8, we have $F \sim \rho \nu^{1/2} D U_0^2 t^{1/2}$, which gives

$$\widetilde{F} \sim \frac{1}{Re^{1/2}} \tau^{1/2}. \tag{2.9}$$

Equation 2.9 predicts that the exponent of the early-time scaling, β, stays at $1/2$, whereas the coefficient of the scaling, α, increases with decreasing Re, qualitatively agreeing with our experiments at intermediate Re when $0.7 < Re < 200$ (Figure 1.5). Quantitatively, we fit $(\alpha - \alpha^\infty)$ as a function of Re from our experiments using

$$\alpha(Re) - \alpha^\infty = \frac{c_0}{Re^\gamma}, \tag{2.10}$$

where $\alpha^\infty = 3\sqrt{6}/2$ is the asymptotic coefficient at the high-Re limit from the initial-impact self-similar theory in Section 2.3.2. Our experiments show $\gamma = 0.45 \pm 0.4$, consistent with the $Re^{-1/2}$ scaling of 2.9 (the inset of Figure 1.5(a)). In addition, we obtain $c_0 = 4.36 \pm 0.50$.

Although the simple scaling of Equation 2.9 successfully explains the early-time scaling of the impact force of viscous drops, the usage of δ_ν as the characteristic length scale in our argument needs a formal justification. Moreover, the simple scaling only provides the viscous contribution of the impact force. It is not clear how the viscous impact force couples with the inertial impact force at finite Re. When fitting experiments using Equation 2.10, we simply assume the two forces are additive. This simple assumption also needs to be justified. Lastly, it is certainly relevant to analytically calculate the coefficient c_0 in the scaling Equation 2.10.

Here, we develop an asymptotic perturbation method to calculate the impact force of viscous drops at finite Re during initial impact [96]. The starting point of our calculation is the leading-order self-similar dimensionless radial velocity field inside the boundary layer. The field was obtained by Philippi and coworkers in analogy to the shock-induced

boundary layers [47], which compares well with the numerical result:

$$u_r^{(0)} = \frac{2r}{\pi\sqrt{\delta^2\tau - r^2}} f'\left(\eta \equiv \frac{\delta}{2}\sqrt{\frac{Re}{\delta^2\tau - r^2}}z\right), \tag{2.11}$$

where $\delta = \sqrt{6}/2$ is a constant, indicating the spreading contact line $r_0 = \delta\sqrt{\tau}$ (Figure 1.3(a)).(Notice that we define dimensionless quantities based on the diameter of liquid drops, instead of the radius of liquid drops used in [47]), which modifies the constant coefficients in Equation 2.11. The profile f' is the erf function and η is introduced as the dimensionless inner variable of the boundary layer. We assume a perturbation expansion for the inner velocity field, (u_r, u_z), in terms of the small parameter $\epsilon = Re^{-1/2}$. Thus, the radial velocity field can be expanded as $u_r = u_r^{(0)} + \epsilon u_r^{(1)} + \epsilon^2 u_r^{(2)} + \mathcal{O}\left(\epsilon^3\right)$ and the vertical velocity field as $u_z = u_z^{(0)} + \epsilon u_z^{(1)} + \epsilon^2 u_z^{(2)} + \mathcal{O}\left(\epsilon^3\right)$. From Equation 2.11 and the mass conservation, we immediately have

$$u_z^{(0)} = 0 \quad \text{and} \quad u_z^{(1)} = -\frac{4}{\pi\delta}\left[2f + \frac{r^2}{\delta^2\tau - r^2}\eta f'\right]. \tag{2.12}$$

Likewise, we also expand the dimensionless outer velocity field ($\eta \gg 1$), (U_r, U_z), in terms of ϵ. The asymptotic matching condition at the order ϵ for the vertical velocity reads [97]

$$\epsilon U_z^{(1)}\left(z = 0\right) = \lim_{\eta\to\infty} \epsilon u_z^{(1)} - \lim_{z\to 0} U_z^{(0)} + \mathcal{O}\left(\epsilon^2\right). \tag{2.13}$$

Using

$$\lim_{z\to 0} U_z^{(0)} = -\frac{2z}{\pi\sqrt{\delta^2\tau - r^2}}\left(2 + \frac{r^2}{\delta^2\tau - r^2}\right), \tag{2.14}$$

obtained from the mass conservation in the outer flow at $z \to 0$ and expressing z in terms of η, we obtain

$$U_z^{(1)}\left(z = 0\right) = -\frac{4}{\pi\delta}\lim_{\eta\to\infty}\left[2\left(f - \eta\right) + \frac{r^2}{\delta^2\tau - r^2}\eta\left(f' - 1\right)\right] + \mathcal{O}\left(\epsilon^2\right). \tag{2.15}$$

Since $f\left(\eta\right) = \eta - 1/\sqrt{\pi} + \mathcal{O}\left(\eta^{-2}\mathrm{e}^{-\eta^2}\right)$, we find that, at the first order of ϵ, the correction

of the vertical velocity of the outer flow at $z = 0$ is

$$U_z^{(1)}(z=0) = \frac{8\sqrt{6}}{3\pi^{3/2}}. \tag{2.16}$$

Remarkably, the presence of the self-similar boundary layer at finite Re induces at $\mathcal{O}(\epsilon)$ a uniform velocity in the outer flow near $z = 0$.

With the boundary conditions corrected due to the boundary layer, the outer velocity field at $\mathcal{O}(\epsilon)$ are given by an inviscid problem that can be solved using a potential velocity field $\Phi^{(1)}$, which satisfies Laplace's equation, $\nabla^2\Phi^{(1)} = 0$, and the set of boundary conditions:

$$\frac{\partial}{\partial z}\Phi^{(1)} = U_z^{(1)}, \quad \text{at } z = 0,\ r < \delta\sqrt{\tau}, \tag{2.17}$$

$$\Phi^{(1)} = 0, \quad \text{at } z = 0,\ r > \delta\sqrt{\tau}, \tag{2.18}$$

$$\Phi^{(1)} \to 0, \quad \text{at } z = \infty. \tag{2.19}$$

The mathematical structure of the problem is the same as the one solved at the zeroth order after changing the frame of reference (Figure 2.7(a)). Hence, the method used in Philippi *et al.* for solving the solution of the outer flow at the zeroth order can be directly used to obtain the flow field at $\mathcal{O}(\epsilon)$ [47]. The uniform asymptotic expansion of the velocity field at $\mathcal{O}(\epsilon)$ can be obtained by matching $u_z = \epsilon u_z^{(1)}$ and $U_z = U_z^{(0)} + \epsilon\nabla\Phi^{(1)}$. An example of a uniform asymptotic expansion of the vertical velocity profile at $r = 0$ at $\mathcal{O}(\epsilon)$ is depicted for $\epsilon = 0.1$ and $\tau = 0.1$ and compared with the profile at $\mathcal{O}(1)$ in figure 2.7(b). The smaller vertical velocity at $\mathcal{O}(\epsilon)$ at a fixed z indicates a faster propagation of the self-similar field in the presence of the boundary layer. In other words, the boundary layer affects the self-similar pressure field, making it propagate faster than that in the inviscid case at the high Re limit (Figure 2.7(b)).

Conveniently, many results at leading order can be renormalised to obtain results at the order of $\mathcal{O}(\epsilon)$ by simply replacing the impact velocity U_0 with $U_0\left(1 + \epsilon U_z^{(1)}\right)$. It is straightforward to show that in comparison with the impact force at the zeroth order

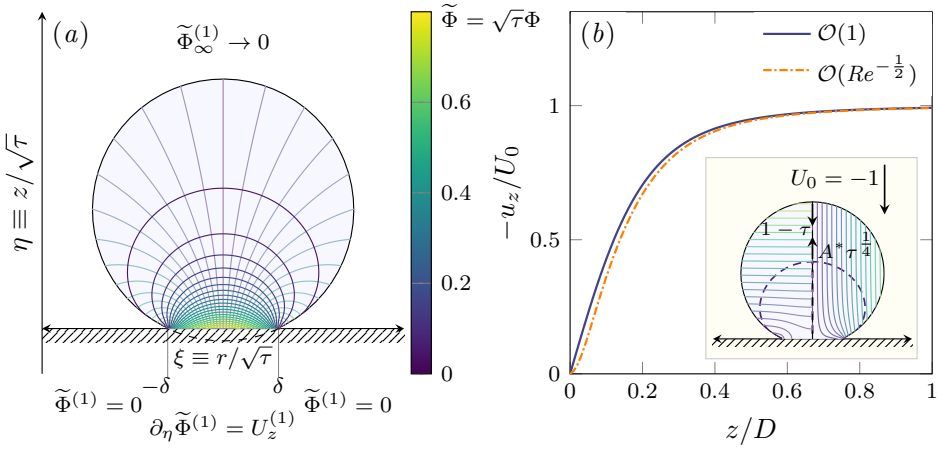

Figure 2.7: Flow induced by viscous boundary layer. (a) Velocity potential lines (thick) and streamlines (thin) in the self-similar frame of reference [47], obtained by calculating the self-similar potential $\widetilde{\Phi}^{(1)} \equiv \sqrt{\tau}\Phi^{(1)}$ from (2.17)-(2.19). The potential satisfies Laplace's equation and the boundary conditions similar to those at $\mathcal{O}(1)$ (cf. Figure 8 in [47]). (b) Dimensionless vertical velocity profile at $r = 0$ in the laboratory frame with $Re = 100$ and $\tau = 0.1$. The thick solid line represents the $\mathcal{O}(1)$ velocity profile from [47]. The dash-dotted line is our uniformly asymptotic correction after introducing the boundary layer. Notice that the dash-dotted line is on the right of the solid line, indicating a faster expansion of the self-similar field in the presence of the boundary layer. The inset shows a snapshot of the potential lines (left) and streamlines (right) in the laboratory frame. The dashed line represents the shape of an isobar far from the impact point. While the apex of the drop travels downward unperturbed as $(1-\tau)$, the isobar propagates upward as $A^*\tau^{1/4}$ in the lab frame (see the text).

(Equation 2.5), the dimensionless force at the first order near $\tau = 0^+$ is

$$\widetilde{F} = \frac{3\sqrt{6}}{2}\left(1 + \frac{8\sqrt{6}}{3\pi^{3/2}}\frac{1}{Re^{1/2}}\right)\tau^{1/2} + \mathcal{O}\left(Re^{-1}\right), \tag{2.20}$$

which gives the coefficient and the exponent of the early-time scaling in $\widetilde{F} = \alpha\tau^{\beta}$

$$\alpha = \frac{3\sqrt{6}}{2}\left(1 + \frac{8\sqrt{6}}{3\pi^{3/2}}\frac{1}{Re^{1/2}}\right) = \alpha^{\infty} + \frac{24}{\pi^{3/2}}\frac{1}{Re^{1/2}} \quad \text{and} \quad \beta = 1/2, \tag{2.21}$$

where $\alpha^{\infty} = 3\sqrt{6}/2$ is the asymptotic value of α when $Re \to \infty$ predicted by the initial-impact self-similar theory Equation 2.6. Equation 2.21 directly confirms the $Re^{-1/2}$ scaling for α at finite Re and, therefore, verifies the usage of the boundary layer thickness δ_ν as the relevant length scale in the simple scaling argument. Second, it shows that the inertial and viscous impact forces are additive as shown in Equation 2.10. Third, it gives $c_0 = 24/(\pi^{3/2}) \approx 4.31$, quantitatively agreeing with our experiments $c_0 = 4.36 \pm 0.50$. As such, Equation 2.11 quantitatively describes the experimental trends of $\alpha(Re)$ and $\beta(Re)$ without fitting parameters (the dashed-dotted lines in Figure 2.5).

The simple picture that the viscous boundary layer effectively increases the propagation speed of the self-similar pressure field also allows us to quantitatively predict the trends of $t_{\max}$ and $F_{\max}$ as a function of Re. To determine $t_{\max}$, we first analyze the propagation of isobars far away from the impact point within an impacting drop. We find that the isobars travel as $\left(U_0 D^3 t\right)^{1/4}$ at the high Re limit (Section A.1). Notice that the propagation speed of isobars is different from the length scale of the self-similar structure. The former indicates the location of constant-pressure contours, whereas the latter arises from the self-similar arguments when constructing the self-similar pressure field (Section A.1). When the isobar of a preset high pressure touches the upper surface of the liquid drop, which moves downward ballistically as $(D - U_0 t)$, the initial-impact regime terminates. Hence, $t_{\max}$, the boundary of the initial-impact regime, can be estimated simply from $A\left(U_0 D^3 t_{\max}\right)^{1/4} = (D - U_0 t_{\max})$, where A is a geometric factor that accounts for the threshold at which the apex starts to be affected by the self-similar pressure field. In the dimensionless form, the condition simply writes as $A\tau_{\max}^{1/4} = (1 - \tau_{\max})$ (see the schematic in Figure 2.3(b)). From the asymptotic value of $\tau_{\max}$ at the high-Re

limit, $\tau_{\max}^{\infty} \approx 0.18 \pm 0.05$, we find $A = 1.24 \pm 0.10$, on the order of one as expected. At finite Re, we assume that the non-monotonic trend of the impact forces also arises from the termination of the initial impact. Nevertheless, the propagation of the isobar should be corrected due to the presence of the boundary layer at finite Re. The isobar now propagates as $A^* \tau_{\max}^{1/4}$ with a renormalised $A^* = A\sqrt{1 + \epsilon U_z^{(1)}}$. The peak time is then given by the solution of the polynomial

$$(1 - \tau_{\max})^4 - A^4 \left(1 + U_z^{(1)} Re^{-1/2}\right)^2 \tau_{\max} = 0. \tag{2.22}$$

Notice that the ballistic motion of the apex of the drop is not affected by the correction $\epsilon U_z^{(1)}$, since the upper surface of the drop has not experienced the impact during the initial impact and, therefore, is not influenced by the impact-induced boundary layer. Equation 2.22 successfully predicts the decrease of $\tau_{\max}$ with decreasing Re, which quantitatively matches $\tau_{\max}(Re)$ in three decades of Re (the dash-dotted line in Figure 2.6(a)).

Although $F_{\max}$ has been extensively investigated and the scaling of $F_{\max}$ with the inertial force $\rho D^2 U_0^2$ has been reported in several previous experiments [86, 64, 65, 87], to the best of our knowledge, a quantitative description of $F_{\max}$ as a function of Re is still not available. Here, we propose a simple model for $F_{\max}(Re)$. Our calculation is based on an interesting observation: the overall shape of the rescaled impact force $F/F_{\max}$ is invariant when plotted against the rescaled time $t/t_{\max}$ in the regime of high and intermediate Re. From high to intermediate Re, $F(t)$ is highly asymmetric with respect to $t_{\max}$ (Figure 2.3(b) and Figure 2.4(a)): the increase of the impact force is fast before $t_{\max}$ and decays much slower after $t_{\max}$. In contrast, for low-Re impacts, $F(t)$ becomes more symmetric (Figure 2.4(a)). The rise and decay of $F(t)$ show a similar time scale. To quantify the change of the shape of $F(t)$, we define a symmetry factor, $S \equiv \int_0^{t_{\max}} F(t)\, \mathrm{d}t / \int_{t_{\max}}^{\infty} F(t)\, \mathrm{d}t$,(Notice that for the impact force of very low Re, $F(t)$ oscillates at long times and exhibits negative impact pressures (figure 2.4a; for explanation see Section 2.3.4). In this case, we replace the upper limit of the integral in the denominator $t = \infty$ to a finite t_0, the time when $F(t)$ first crosses zero.) which is shown as a function of Re in Figure 2.8(b). Interestingly, S reaches a plateau $S^{\infty} = 3.08 \pm 0.01$ when $Re > 7$, showing that the impulse of impacts before

$t_{\max}$ invariably annihilates a quarter of the total momentum of liquid drops irregardless Re as long as $Re > 7$. The constant plateau of S suggests that the shapes of the rescaled impact force, $F(t/t_{\max})/F_{\max}$, are invariant with changing Re and can be collapsed into a master curve when $Re > 7$. We directly confirmed this hypothesis in our experiments (Figure 2.8(a)). The collapse of $\widetilde{F}(\tau)$ at high Re without the rescaling $\widetilde{F}/\widetilde{F}_{\max}$ and $\tau/\tau_{\max}$ has also been reported in a recent experiment, where $\widetilde{F}_{\max} = \widetilde{F}^{\infty}_{\max}$ and $\tau_{\max} = \tau^{\infty}_{\max}$ are constant [87]. Finally, since the integral of the force is equal to the momentum of the drop,

$$\int_0^{\infty} \widetilde{F}\,(\tau)\ \mathrm{d}\tau = \frac{\pi}{6}, \tag{2.23}$$

it is straightforward to show that

$$\tilde{F}_{\max} = \widetilde{F}^{\infty}_{\max}\frac{\tau^{\infty}_{\max}}{\tau_{\max}}. \tag{2.24}$$

Using Equation 2.22 and the asymptotic value of $\widetilde{F}_{\max}$ at high Re, $\widetilde{F}^{\infty}_{\max} \approx 0.83$, Equation 2.24 quantitatively predicts the trend of $\widetilde{F}_{\max}(Re)$ for over five decades of Re between 0.3 and 10^4 (the dash-dotted line in Figure 2.6(b)).

2.3.4 Temporal Evolution of the Impact Force at the Low Re Regime

At even lower Re below 0.7, β increases above 1/2 and deviates from the scaling predicted for impact forces near $\tau = 0^+$ at finite Re. The data also show a strong scatter in this regime (Figure 2.5(b) and Figure 2.6(a)). To experimentally achieve these low-Re impacts, we had to use silicone oils of high viscosities above $10,000$ cSt. Silicone oils of such high viscosities are made of polymerised siloxanes of high molecular weights, which exhibit obvious viscoelasticity during fast impacts. The increase of β can be attributed to the increase of elasticity. In the elastic limit, the kinetic energy of an impinging drop is converted into the elastic potential of the deformed drop. The deformation of the elastic drop can still be approximated as $d \approx U_0 t$ at short times. The elastic strain in the deformed drop is d/r_0 with $r_0 \approx \sqrt{dD}$ and the volume of the deformed region is $\sim r_0^2 d$. The energy balance in the elastic limit can then be written as

$$Fd \sim E\frac{d}{r_0}r_0^2 d, \tag{2.25}$$

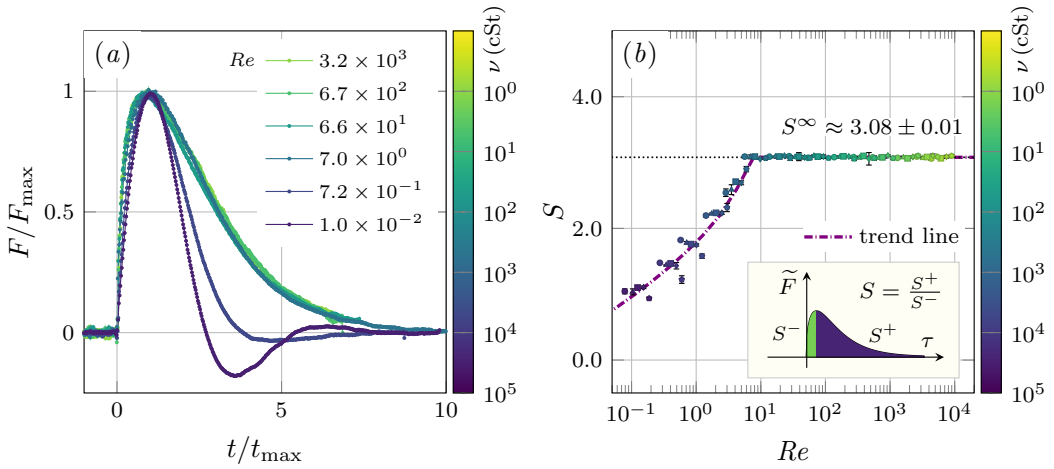

Figure 2.8: Shape of impact forces. (a) Rescaled impact forces of the six impacts shown in figure 2.4(a). F is normalised by the maximum impact force, $F_{\max}$, and t is normalised by the peak time, $t_{\max}$. The rescaled impact forces collapse into a master curve for $Re > 7$. Notice that the curves are the same if plotting in terms of dimensionless quantities $\widetilde{F}/\widetilde{F}_{\max}$ versus $\tau/\tau_{\max}$. (b) Symmetry factor, S, defined as the quotient of the time integral of $\widetilde{F}$ before and after $\tau_{\max}$, as a function Re (see inset). The horizontal dashed line indicates the asymptotic value at high Re. The thick dash-dotted line is a fitting as a guide of eyes.

which gives

$$\tilde{F} \sim \frac{E}{\rho U_0^2}\tau^{3/2} \tag{2.26}$$

in the dimensionless form, where E is the elastic modulus of the drop. The $\tau^{3/2}$ scaling is the well-known result for the impact force of elastic spheres with Hertzian contacts. A detailed calculation shows

$$\tilde{F} = \frac{2\sqrt{2}}{3}\frac{E}{\rho U_0^2}\tau^{3/2} \tag{2.27}$$

(see Section 2.2.2). The large exponent 3/2 in the pure elastic limit qualitatively explains the increase of β as the elastic effect of high-molecular-weight silicone oils gradually sets in. In the presence of viscoelasticity, Re is no longer a proper dimensionless number for scaling the data, which results in the strong scatter of data shown in Figures 2.5(b) and Figure 2.6(a).

The effect of viscoelasticity of high-molecular-weight silicone oils can also be seen from the overall shape of impact forces (Figure 2.4(a) and Figure 2.8(a)). While $F(t)$ of low-viscosity silicone oils are highly asymmetric, $F(t)$ for high-molecular-weight silicone oils becomes more symmetric with respect to $t_{\max}$, approaching the symmetric impact force of elastic spheres. Quantitatively, the symmetry factor, S, of high-Re impacts is large with $S^{\infty} = 3.08 \pm 0.01$ (Figure 2.8(b)). In contrast, S of the high-viscosity silicone oils gradually approaches 1, signalling a perfect symmetric curve similar to the impact force of elastic spheres. The elastic effect becomes even more obvious for silicone oils of very high viscosity above $30,000$ cSt. The drops made of these oils bounce upward slightly towards the end of impact processes due to their elasticity, leading to negative impact pressures and oscillating impact forces (Figure 2.4(a)).

To conclude this result and discussion, we summarise the early-time scaling of impact forces during initial impact at different regimes in Table 2.1.

2.4 Conclusion

By synchronising force sensory with the high-speed photography, we simultaneously measured both the kinematics and dynamics of liquid-drop impacts over a wide range of Re. Our experiments on the early-time scaling of impact forces verified that the

Impact regime	Re	α	β
Inertial	> 200	$\frac{3\sqrt{6}}{2}$	$1/2$
Viscous	$0.7 - 200$	$\frac{3\sqrt{6}}{2}\left(1 + \frac{8\sqrt{6}}{3\pi^{3/2}}\frac{1}{Re^{1/2}}\right)$	$1/2$
Elastic	N/A	$\frac{2\sqrt{2}}{3}\frac{E}{\rho U_0^2}$	$3/2$

Table 2.1: Early-time scaling of impact forces, $\widetilde{F} = \alpha\tau^{\beta}$, near $\tau = 0^{+}$ at three different impact regimes

initial impact of a liquid drop at high Re is governed by upward expanding self-similar pressure and velocity fields. The expanding speed of the self-similar fields is of the same order of magnitude as the impact speed of the liquid drop. The prediction of the initial-impact self-similar theory breaks down when $Re \lesssim 200$, where viscous dissipation becomes important. Using a perturbation method, we quantitatively analysed the early-time scaling of the impact force of viscous drops at finite Re. Our calculation provided a quantitative description of the maximum force ($F_{\max}$) and the peak time ($t_{\max}$) as a function of Re. Lastly, we also discussed the influence of viscoelasticity on the temporal evolution of impact forces of high-viscosity silicone oils. In the spreading regime of drop impacts, we generalised the asymptotic self-similar solution proposed by Eggers and co-workers [61] and found an exact solution for inertia-driven drop spreading at finite times at high Re. Our solution quantitatively predicts the height of spreading drops. The discrepancy between the exact solution and experiments on the temporal evolution of contact lines and impact forces reveals the limit of the self-similar approach in predicting drop-spreading dynamics. In summary, our systematic experiments illustrate the detailed temporal evolution of impact forces across inertial, viscous and viscoelastic regimes. The corresponding theoretical analysis provides a quantitative understanding of the early-time scaling of impact forces in these different impact regimes. Finally, our exact self-similar solution on inertia-driven drop spreading extends the well-known asymptotic self-similar scaling to finite times and provides a parameter-free description of the height of spreading drops.

Our work also poses new questions and directions. Theoretically, the logical next step is to incorporate the exact solution of the Euler equations with the solution of the boundary layer [61] and quantitatively predict the rim dynamics of liquid lamella [98] and the temporal evolution of impact forces during spreading. More importantly,

a theoretical understanding is needed to bridge the two self-similar regimes at high Re, which should illustrate how the self-similar spreading establishes from the expanding self-similar fields at the end of initial impacts. This transition is particularly important given that the maximum impact force occurs during the transition. Experimentally, we have showed that high-speed imaging and fast force measurement are two complementary tools. While high-speed imaging can accurately resolve the variation of the shape of impacting drops during spreading, force measurement reveals the unique signature of drop dynamics during initial impact. Although the use of high-speed photography has become a routine in the study of drop impacts [26], the combination of the two has not been frequently implemented. A broader application of the combined techniques will certainly deepen our understanding of liquid-drop impacts.

Chapter 3

Shear Stress and Pressure of Drop Impact

3.1 Introduction

Laozi, the ancient Chinese philosopher in the 6th century BCE, has long noticed that water, although the softest and weakest material known in his time, is most effectual in eroding hard substances [99]. The saying of Laozi has often been misinterpreted nowadays, the erosion of solid surfaces such as stones eroded by impacting drops is usually attributed to their virtue of persistence (Figure 3.1(a)), rather than their effectiveness in erosion because of their fluid nature. To demonstrate the superior ability of drop impact in erosion, we compare the size of impact craters by liquid drops and those by solid spheres on both granular media and plaster slabs. The impact craters by liquid drops are always larger than those by solid spheres under similar impact conditions (Figure 3.1(b)-(e), Table B.1 in Section B.1). Why are liquid drops so erosive? What are the key dynamic features that distinguish the erosion of drop impact from that of solid-sphere impact? Beyond testifying the wisdom of the ancient philosopher, the answers to these questions are of great importance for a wide range of natural, environmental and engineering processes including soil erosion [100, 101, 4, 67], preservation of heritage sites [102, 103], wear of wind and steam turbine blades [104], and cleaning and peening of solid materials (e.g. silicon wafers) [82, 105].

The superior ability of an impacting drop in erosion cannot stem from its impact

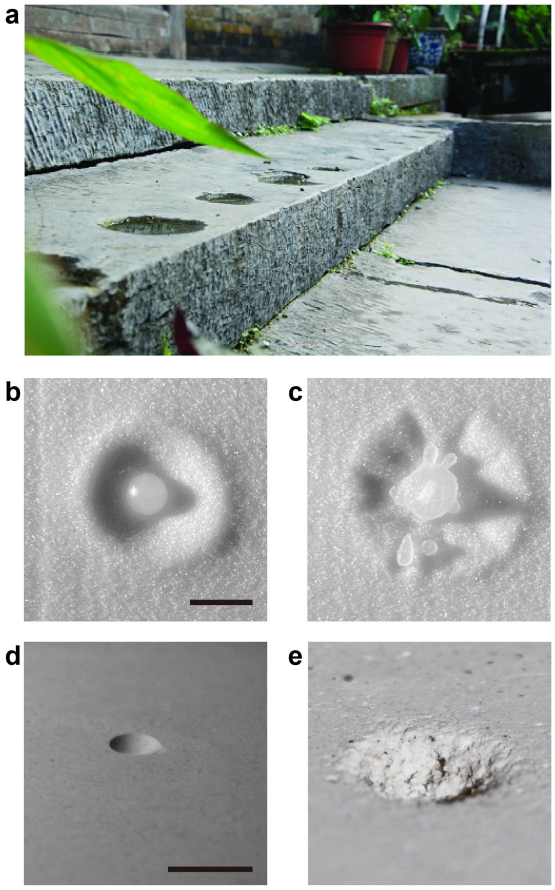

Figure 3.1: Surface erosion by drop impact. (a), Dripping water hollows out stone: Raindrop-induced holes on a stone step underneath the eaves of a historical 300-year-old house in Yangshuo, China. The holes have a diameter of ~ 5 cm and a depth of ~ 0.5 cm. (Image credit: Guilin Daily, 23 Sept 2015). (b),(c), Comparison of the craters in granular media created by the impact of a nylon sphere (left) and a water drop (right) of the similar size ($D \approx 3$ mm) and impact velocity ($U = 2.97$ m/s). Scale bar: 5 mm. (d),(e), Comparison of the craters in plaster slabs by the repeated impacts of steel spheres ($D = 5.0$ mm, $U = 1.4$ m/s, number of impact $N = 235$) (left) and water drops ($D = 3.0$ mm, $U = 2.6$ m/s, $N = 2500$) (right). The total impact energies are the same at 0.12 J. Scale bar: 5 mm. We also compare impact craters with the same number of impact and the same impact momentum. Drop-impact craters are larger and deeper in all cases (Table B.1 in Section B).

force, as the maximum impact force induced by a millimetric water drop falling near its terminal velocity is more than an order of magnitude smaller than that generated by the impact of a solid sphere of similar size, density and velocity [66]. The average impact pressure of the drop is even smaller due to the large contact area formed by the spreading drop. Thus, instead of impact force or average impact stress, the erosion ability of drop impact must originate from the unique spatiotemporal structure of its impact stress and the response of impacted substrates under the dynamic stress. However, although the impact force of liquid drops has been recently studied experimentally [66, 86, 65, 64, 87, 50, 106], quantitative measurements which can measure the stress distributions of drop impact on solid surface are still not available. Here, we develop a new experimental method—high-speed stress microscopy—to measure the shear stress and pressure of drop impact on solid elastic substrates. The method integrates the principles of three state-of-the-art imaging techniques, i.e., traction force microscopy, laser-sheet microscopy and high-speed photography, allowing us to map the temporal evolution of the pressure and shear stress distributions underneath millimeter-sized drops in fast impact events with a microsecond temporal resolution and a micron-scale spatial resolution. Our measurements using this novel method provide not only first experimental results on the unusual dynamics of the impact stress distributions but also new insights into the origin of high erosion efficiency of drop impact.

3.2 Methods

3.2.1 Parameters of Drop Impact

Our drops are made of a sodium iodide aqueous solution (60% w/w), which has a similar viscosity η and surface tension σ as water but with a density ρ 2.2 times higher. The diameter of drops is measured by using ImageJ to analyze the snapshots of drops and fit with spherical shapes. Drops of $D = 3.49 \pm 0.19$ mm impact normally on the surface of the PDMS gels at $U = 2.97$ m/s, giving a Reynolds number $Re = \rho UD/\eta = 22,800$ and a Weber number $We = \rho DU^2/\sigma = 940$. Hence, the impact is dominated by fluid inertia at early times, when the shear stress and pressure of the drop are highest leading to the strongest erosion [47]. Below, we focus on drop impact at early times and report positions and times in dimensionless forms using D and D/U as the corresponding

length and time scales.

3.2.2 Preparation and Characterization of PDMS Substrates

Polydimethylsiloxane (PDMS) elastomers were prepared from two-part Sylgard 184 silicone elastomer kits (Dow Corning). To adjust the Young's modulus, E, of the cured PDMS gels, we mixed siloxane monomers with crosslinkers at a controlled mass ratio. In most experiments reported in this paper, we used a monomer-to-crosslinker mass ratio of 30:1, which yielded PDMS gels of $E = 100$ kPa. PDMS gels of $E = 250$ kPa (mass ratio 20:1) and $E = 420$ kPa (mass ratio 18:1) have also been tested to assess the effect of gel stiffness on the impact pressure and shear stress. Florescent polystyrene (PS) particles of diameter 30 μm (ThermoFisher) were mixed into the two-part PDMS mixtures at a controlled volume fraction of 0.23% before curing. The PDMS-particle mixture was finally vacuumed to remove air bubbles and placed in an oven at 90°C overnight for curing. The fully cured gels have a fixed thickness of 6.5 mm and an area of 24 $\times$ 24 mm^2. The area is much larger than the maximum spreading area of impacting drops.

We measured the Young's modulus of the cured gels by surface indentation. Specifically, we used a steel ball of radius $R = 2.5$ mm as an indenter. A control weight was then applied on the top of the sphere to indent the gels. The indentation length d at a given indentation force F was measured from the side view. The Young's modulus of the gels was calculated via the Hertzian contact equation [91]:

$$F = \frac{3}{4} E^* R^{1/2} d^{2/3}, \tag{3.1}$$

where the reduced Young's modulus E^* is defined as

$$\frac{1}{E^*} = \frac{1-\nu^2}{E} + \frac{1-\nu_s^2}{E_s} \approx \frac{1}{2E}. \tag{3.2}$$

Here, E and ν are Young's modulus and the Poisson's ratio of the PDMS gels, and E_s and ν_s are the Young's modulus and the Poisson's ratio of the sphere. Note that $E \ll E$s and $\nu \approx 0.5$. We also estimated the Young's modulus by matching the experimental stress distributions of solid-sphere impact with those from finite element simulations.

Young's moduli measured using these two different methods agree well with less than 20% difference. The value of the Young's moduli thus obtained also agree quantitatively with previous studies [107, 108]. The Poisson's ratio of the gels, ν, is more difficult to measure accurately. We used $\nu = 0.49$ based on previous studies of the mechanical properties of PDMS gels under small strains [109].

We modified the wettability of the surface of the PDMS gels via plasma modification. The PDMS gels were exposed to air plasma for 3 mins with a power of 100 W. The pressure of a chamber for plasma treatment was 300 mTorr. Without the plasma modification, the untreated PDMS surface is hydrophobic with a contact angle around 90°. After the modification, the surface becomes hydrophilic with a contact angle less than 10°. Untreated hydrophobic gels were used in all the experiments reported in this study unless stated otherwise (Figure B.3).

3.2.3 Image Analysis and Data Average

The fluorescent PS particles embedded in the PDMS gels were served as tracers to track the deformation of the gels under impact. We used standard Particle Image Velocimetry (PIV) algorithm (PIVlab, Matlab) to track the displacement field of the gels at different times [110]. An interrogation window of 384 μm $\times$ 384 μm with 70% overlap was adopted in PIV, which gave a spatial resolution of 115 μm. The temporal resolution is 0.025 ms, which is set by the frame rate of high-speed photography.

To reduce measurement errors, we first averaged the cross-correlation fields of PIV from five repeated impacts on the same gel at the same location, which were used to calculate the average shear stress and pressure fields shown in Figure 3.3 and 3.7. The results such as the position of the maximum shear stress and the drag force shown in Figure 3.4 and 3.6 were the outcome of a further average over three different average displacement fields for impacts on different gels or impacts on the same gels at different impact locations. Thus, one data point in Figure 3.4 and 3.6 is the average result of total 15 experiments.

3.2.4 Moving-least Squares (MLS) Method

Stress fields depend on strain fields, which are the derivative of the displacement fields. A smoothing procedure is necessary in order to reduce the noise of differentiation. We used the moving-least squares (MLS) interpolation method to obtain a continuously differentiable displacement field from an experimentally obtained discrete PIV displacement field [111]:

$$\mathbf{g}(\mathbf{x}) = \mathbf{P}^T(\mathbf{x})\mathbf{a}(\mathbf{x}) \tag{3.3}$$

where $\mathbf{g}(\mathbf{x})$ is the targeted continuous displacement field, $\mathbf{P}^T(\mathbf{x})$ is a polynomial basis and $\mathbf{a}(\mathbf{x})$ is the corresponding coefficients of the basis. x is the continuous position vector. Because of the cylindrical symmetry of drop impact geometry, we chose $x = (r, z)$ with $r = 0$ and $z = 0$ at the impact point. The negative z direction points along the direction of the impact velocity of drops. We adopted a cubic polynomial basis, so $\mathbf{P}^T(\mathbf{x})$ and $\mathbf{a}(\mathbf{x})$ are

$$\mathbf{P}^T(\mathbf{x}) = [1, r, z, r^2, z^2, rz, r^3, z^3, r^2z, rz^2], \tag{3.4}$$

$$\mathbf{a}(\mathbf{x}) = [\mathbf{a_0}(\mathbf{x}), \mathbf{a_1}(\mathbf{x}), \mathbf{a_2}(\mathbf{x}), ..., \mathbf{a_9}(\mathbf{x})]. \tag{3.5}$$

Noting that $\mathbf{a}(\mathbf{x})$ is not constant, and it varies with the different position vectors. The coefficients of the targeted function at x were obtained by minimizing the weighted least-square error,

$$L(\mathbf{x}) = \sum_{i=1}^{n} f(\mathbf{x} - \mathbf{b_i})[\mathbf{P}^T(\mathbf{b_i})\mathbf{a}(\mathbf{b_i}) - \mathbf{w}(\mathbf{b_i})]^2 \tag{3.6}$$

where $\mathbf{w}$ is the discrete PIV displacement field from experiments. $\mathbf{b_i}$ indicates the discrete PIV coordinates with a total n = 540 points in our experiments. $f(x - bi)$ is the decaying weighted function defined as [112]:

$$f(\mathbf{x} - \mathbf{b_i}) = \begin{cases} \frac{\exp(1-d^2/d_m^2)-1}{e-1} & \text{for } d \le d_m \\ 0 & \text{for } d > d_m \end{cases} \tag{3.7}$$

where $d = |\mathbf{x} - \mathbf{b_i}|$ is the distance between the continuous position $\mathbf{x}$ and $\mathbf{b_i}$. d_m is the cut-off distance:

$$d_m = 2\sum_{i=1}^{m} \frac{|\mathbf{x} - \mathbf{b_i}|}{m}. \tag{3.8}$$

m is adjustable and it determines the fitting range. In this study we chose $m = 43$. By making the derivative of L with respect to $\mathbf{a}(\mathbf{x})$ to be zero in order to minimize L, it leads to a set of linear equations which can be solved analytically. The solution of the interpolation function $\mathbf{g}(\mathbf{x})$ gives

$$\mathbf{g}(\mathbf{x}) = \mathbf{P}^T(\mathbf{x})\mathbf{a}(\mathbf{x}) = \mathbf{P}^T(\mathbf{x})\mathbf{A}^{-1}(\mathbf{x})\mathbf{B}(\mathbf{x})\mathbf{w} \tag{3.9}$$

where

$$\mathbf{A}(\mathbf{x}) = \sum_{i=1}^{n} f(\mathbf{x} - \mathbf{b_i})\mathbf{P}(\mathbf{b_i})\mathbf{P}^T(\mathbf{b_i}). \tag{3.10}$$

$$\mathbf{B}(\mathbf{x}) = [f(\mathbf{x} - \mathbf{b_1})\mathbf{P}(\mathbf{b_1})\mathbf{P}^T(\mathbf{b_1}), ..., f(\mathbf{x} - \mathbf{b_n})\mathbf{P}(\mathbf{b_n})\mathbf{P}^T(\mathbf{b_n})]. \tag{3.11}$$

3.2.5 Calculations of Shear Stress and Pressure

Through applying the MLS method in Section 3.2.4, the continuous displacement fields were obtained, and the strain fields can be calculated by taking the spatial derivative to the interpolation polynomial functions $\mathbf{g}(\mathbf{x})$, where $g^T = [g_r, g_z]$. Because the deformation of the substrate is small in this study, we adopted the assumption of linear elasticity. The strain-displacement relation is expressed as:

$$\epsilon = \frac{1}{2}((\nabla \mathbf{g}) + (\nabla \mathbf{g})^T) \tag{3.12}$$

where ϵ is the strain tensor. For an axisymmetric case in the cylindrical coordinate, the strain-displacement relation can be reduced to

$$\epsilon_{rr} = \frac{\partial g_r}{\partial r}, \epsilon_{zz} = \frac{\partial g_z}{\partial z}, \epsilon_{\theta\theta} = \frac{g_r}{r}, \epsilon_{rz} = \frac{1}{2}[\frac{\partial g_r}{\partial z} + \frac{\partial g_z}{\partial r}] \tag{3.13}$$

where ϵ_{rr}, ϵ_{zz}, and $\epsilon_{\theta\theta}$ are the normal strains in the r, z, and θ direction, respectively. ϵ_{rz} is the shear strain. By applying the linear elastic isotropic model, which implies that

the properties of the polymer gel are independent of direction and it is in the leaner elastic regime, the generalized Hooke's law can be applied. Therefore it follows the stress-strain relation:

$$\sigma_{ij} = \lambda\epsilon_b\delta_{ij} + 2G\epsilon_{ij}. \tag{3.14}$$

where $\lambda = 2\nu G/(1-2\nu)$ is the Lamé constant, $G = E/2(1+\nu)$ is the shear modulus, ν is the Poisson's ratio, and δ_{ij} is the Kronecker delta. ϵ_b is the bulk strain, which is the sum of the three normal strains $\epsilon_b = \epsilon_{rr} + \epsilon_{zz} + \epsilon_{\theta\theta}$. In this study, we define σ_{rz} as the shear stress τ, and σ_{zz} gives the pressure p.

The PDMS polymer gels are nearly incompressible with Poisson's ratio close to 0.5, which leads to a very large λ. On the other hand, the bulk strain ϵ_b is close to 0. Therefore, the impact pressure cannot be accurately determined from the product of $\lambda\epsilon_b$ in Equation 3.14. Instead, we adopted a different approach by using the quasisteady state assumption [111]. Specifically, we replaced $\lambda\epsilon_b$ by a term $-\mu$ in Equation 3.14.

$$\sigma_{ij} = -\mu\delta_{ij} + 2G\epsilon_{ij}. \tag{3.15}$$

Under the quasi-steady-state assumption, the stress tensor obeys:

$$\sum_{j=1}^{3} \frac{\partial\sigma_{ij}}{\partial x_j} = 0. \tag{3.16}$$

By substituting Equation 3.14 into Equation 3.15, Equation 3.16 becomes

$$\mu(\mathbf{x}) = \mu(\mathbf{x_0}) + G\int_{\mathbf{x_0}}^{\mathbf{x}} (\nabla^2\mathbf{g})\cdot d\mathbf{s} + G[\epsilon_b(\mathbf{x}) - \epsilon_b(\mathbf{x_0})] \tag{3.17}$$

where x_0 sets a reference point for integration. We chose the reference point at the top layer $z = 0$ with r as large as possible away from the impact point at short times. Taking $p(x_0) = \sigma_{zz}(x_0) = 0$, we have $\mu(x_0) = 2G\sigma_{zz}(x_0)$. The integration path goes from the reference point x0 to x, as shown in Figure B.1. Finally, the pressure can be obtained

$$p(\mathbf{x}) = -G\int_{\mathbf{x_0}}^{\mathbf{x}} (\nabla^2\mathbf{g})\cdot d\mathbf{s} + G[\epsilon_b(\mathbf{x}) - \epsilon_b(\mathbf{x_0})] + 2G[\epsilon_{zz}(\mathbf{x}) - \epsilon_{zz}(\mathbf{x_0})] \tag{3.18}$$

For an axisymmetric case, the Laplacian term $\nabla^2 g$ in the cylindrical coordinate can be calculated by

$$\nabla^2 \mathbf{g} = (\frac{\partial^2 g_r}{\partial r^2} + \frac{1}{r}\frac{\partial g_r}{\partial r} + \frac{\partial^2 g_r}{\partial z^2} - \frac{g_r}{r^2})\mathbf{e_1} + \frac{\partial^2 g_z}{\partial r^2} + \frac{1}{r}\frac{\partial g_z}{\partial r} + \frac{\partial^2 g_z}{\partial z^2})\mathbf{e_2} \tag{3.19}$$

e1 and **e2** are the unit vector also in the direction of the r and z axes, respectively.

To verify the quasi-steady-state assumption used in the pressure calculation, we compared the ratio of the inertial force to the elastic force per unit volume:

$$ra = |\frac{\rho_g \frac{\partial^2 g_z}{\partial t^2}}{\frac{\partial \sigma_{zz}}{\partial z}}| \tag{3.20}$$

for solid-sphere impact, where ρ_g is the density of the PDMS gels. $ra < 2\%$ near the impact axis where the impact stress is large enough relevant to our measurements. Consistent with the estimate, the impact pressure of solid spheres calculated using the quasi-steady state assumption quantitatively matches that of the finite-element simulations without the assumption (Figure 3.2). It should be emphasized that the calculation of shear stress—the quantity most relevant to surface erosion—does not rely upon the quasi-steady-state assumption and therefore is immune to the errors associated with the assumption.

3.2.6 Finite Element Analysis

To calibrate high-speed microscopy and testify its accuracy (Figure 3.2(b) and (c)), we used the commercial finite element software ABAQUS to simulate solid-sphere impact, which has a shorter time scale compared with drop impact at the same impact condition. The impact geometry was axisymmetric. The element shape for the meshing of the impacted surface was quadrilateral with adjustable sizes. Near the impact point, the element size was 0.2 mm. The diameter and the impact velocity of the impacting solid sphere were 3.16 mm and 0.49 m/s, matching the impact condition of the experiments. Since Young's modulus of the steel sphere is much larger than that of the impacted PDMS substrate, the sphere is assumed to be rigid in the simulation. The substrate is isotropic and linearly elastic. While Poisson's ratio of the substrate was fixed at 0.49, Young's modulus of the substrate was chosen to match the outcome of

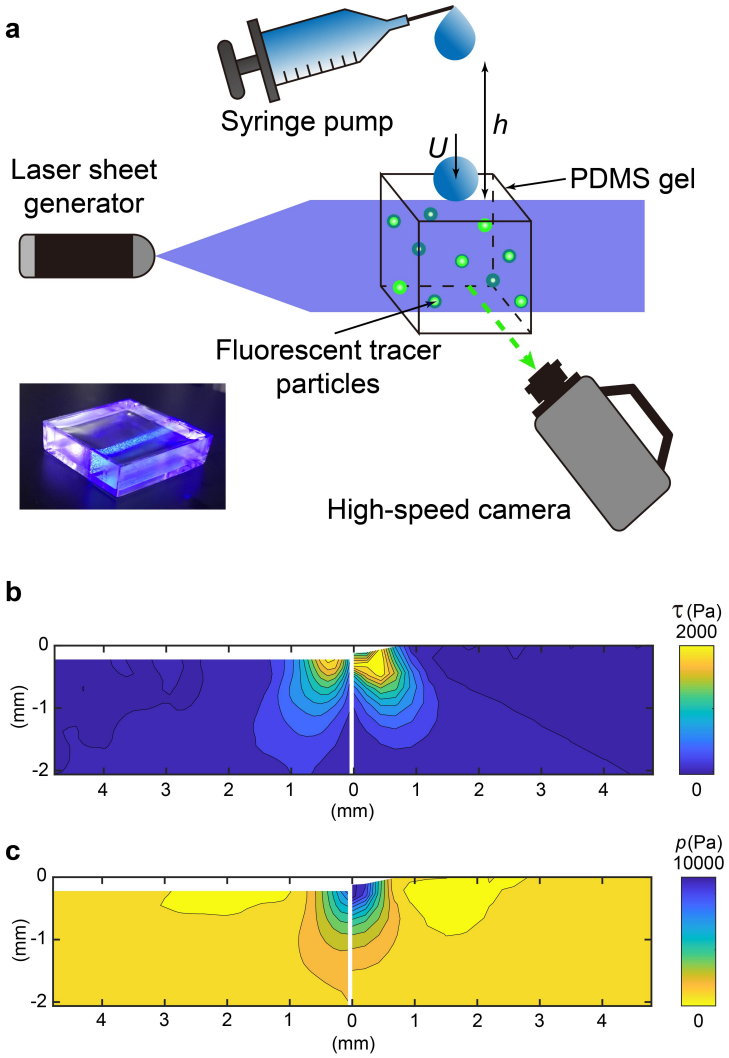

Figure 3.2: High-speed stress microscopy. (a), A schematic showing the principle of high-speed stress microscopy. Lower left inset: An image of the PDMS gel embedded with fluorescent particles under the illumination of the laser sheet. (b),(c), Comparison of (b) the shear stress and (c) the pressure induced by the impact of a steel sphere obtained from high-speed stress microscopy (left) and from finite element simulations (right). The impact condition is specified in the text. The impact time is $t = 0.25$ ms, where $t = 0$ corresponds to the momentum when the sphere first touches the solid surface.

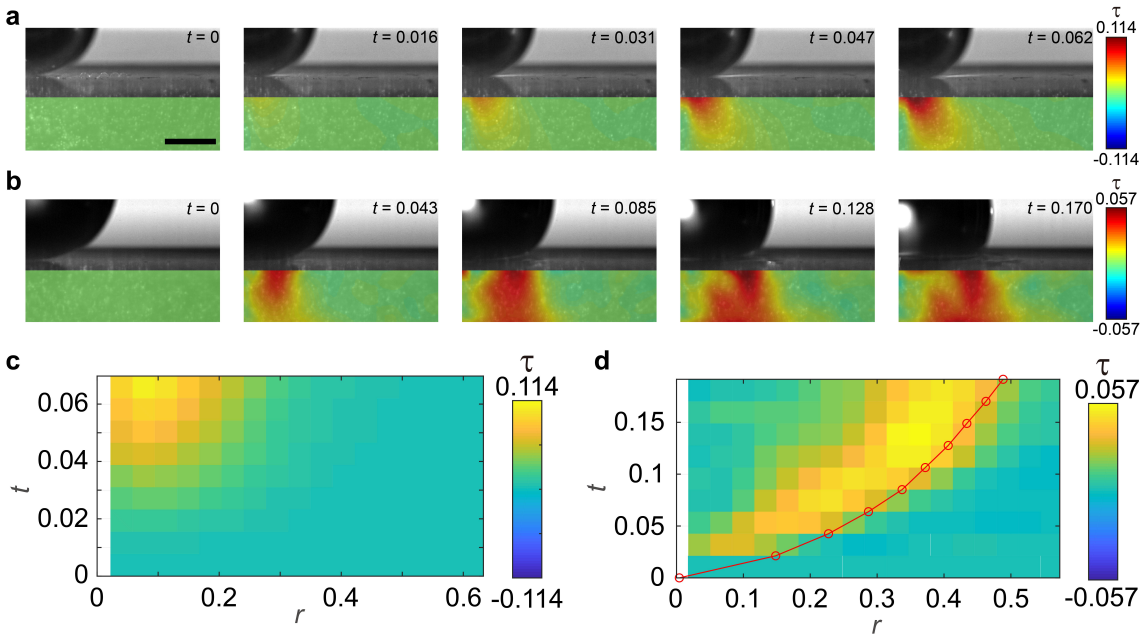

Figure 3.3: Shear stress distribution of solid-sphere impact and drop impact. (a), (c), The temporal evolution of the shear stress $\tau(r, z, t)$ and the spatiotemporal diagram of the surface shear stress $\tau(r, z = 0, t)$ of the impacting steel sphere. τ is non-dimensionalized by $E^{4/5}(\rho U^2)^{1/5}$, a scaling based on the energy balance (Section B.3). (b), (d), The temporal evolution of $\tau(r, z, t)$ and the spatiotemporal diagram of $\tau(r, z = 0, t)$ of the impacting drop. τ is non-dimensionalized by ρU^2 based on the self-similar theory with infinitely rigid substrates [47]. The impact conditions are specified in the text. The red line in (d) indicates the position of the turning point. Scale bar: 1 mm.

experiments. Thus, the simulation allowed us to assess Young's modulus of the PDMS gels, independent of the indentation measurements discussed above. The two methods yielded quantitatively similar moduli, which also agree well with the literature value. To numerically solve the coupled equations of the impact stress of impacting drops and the deformation of elastic media (Figure 3.9), we used the partial differential equation toolbox in Matlab. Specifically, we adopted the transient axisymmetric geometry in the structural mechanics analysis of the toolbox. The pressure and shear stress distributions of incompressible drops on infinitely rigid substrates (Equation B.10 and B.11 in Section B.6) were assigned as the boundary loads on the elastic medium, which has Young's modulus and Poisson's ratio matching those of experiments. We then numerically calculated the radial and vertical displacements of the surface of the elastic medium as a function of time (Figure B.5). The dimension and the grid size of the medium are chosen so that the results are convergent independent of these parameters. The detailed discussion of the coupled differential equations and their numerical solutions can be found in Section B.6.

3.3 Results and Discussion

Figure 3.2(a) shows the idea of experimental setup of high-speed stress microscopy. Specifically, we embed low-concentration (0.23% v/v) fluorescent polystyrene particles of diameter 30 μm in a cross-linked polydimethylsiloxane (PDMS) gel as tracers to track the deformation of the gel under impact (Section 3.2.2). The surface area of the gel is much larger than the maximum spreading diameter of impacting drops. A thin laser sheet of 30 μm thickness illuminates the gel from the side and excites the fluorescent label of tracer particles within the sheet. The laser sheet is finely adjusted to be normal to the impacted surface and through the center of impacting drops. A high-speed camera focusing on the sheet is then used to image the motions of fluorescent tracers at 40,000 frames per second. The resulting tracer displacement fields at different times are processed to calculate the temporal evolution of the stress distributions within the gel (Section 3.2.2). The gel surface is hydrophobic with the contact angle$\sim$90°. We control the Young's modulus of the gel at $E = 100$ kPa in our experiments, so that the deformation of the gel is large enough to be accurately measured by our image analysis,

but small enough that the impact process of liquid drops is not strongly affected by the deformation at the surface. Gels with Young's modulus up to 420 kPa by changing the mass ratio of crosslinkers to monomers are also tested. Furthermore, we also examine the gels with hydrophilic surfaces through applying the plasma treatment (Figure B.3).

As a calibration and the basis of comparison, we first measure the pressure and shear stress induced by the impact of a solid steel sphere of diameter $D = 3.16$ mm at impact velocity $U = 0.49$ m/s by using Equation 3.14 and 3.18, and compare the experimental results with those from finite-element (FEM) simulations under the same condition. Figure 3.2(b) and (c) show the contours of the shear stress τ and pressure p fields of solid-sphere impacts at $t = 0.25$ ms, respectively. It shows that experiments and simulations match quantitatively, verifying the accuracy of high-speed stress microscopy.

3.3.1 Shear Stress of Drop Impact

Figure 3.3(a) and (b) compare the temporal evolution of the shear stress of solid-sphere impact and drop impact at early times. Upon the impact, spatially non-uniform shear stresses quickly develop in both cases. However, while the position of the maximum shear stress of solid-sphere impact is stationary near the impact axis at $r = 0.095$, the maximum shear stress of drop impact propagates radially with the spreading drop. Quantitatively, the spatiotemporal diagrams of the shear stress near the contact surface, $\tau(r, z = 0, t)$, of the two impact processes are shown in Figure 3.3(c) and (d), highlighting further the fast propagation of the maximum shear stress of drop impact. Besides, Figure 3.3(d) shows that the magnitude of the maximum shear stress increases in the beginning. After it reaches to the maximum value at $t = 0.13$, the maximum shear stress then decreases. Here, $t = 0$ is defined as the moment when the impacting drop or sphere first touches the gel surface.

To understand the origin of the maximum shear stress of drop impact, we correlate the position of the maximum shear stress r_τ with the shape of impacting drops (Figure 3.4). Two kinematic features are analyzed: the tip of the expanding lamella r_{lm} and the turning point r_c, where the drop body connects to the root of the lamella (Figure 3.4 inset). While the lamella moves significantly faster than the maximum shear stress, r_τ follows closely behind r_c. Hence, the maximum shear stress arises from the strong velocity gradients near the turning point, where the flow changes rapidly from

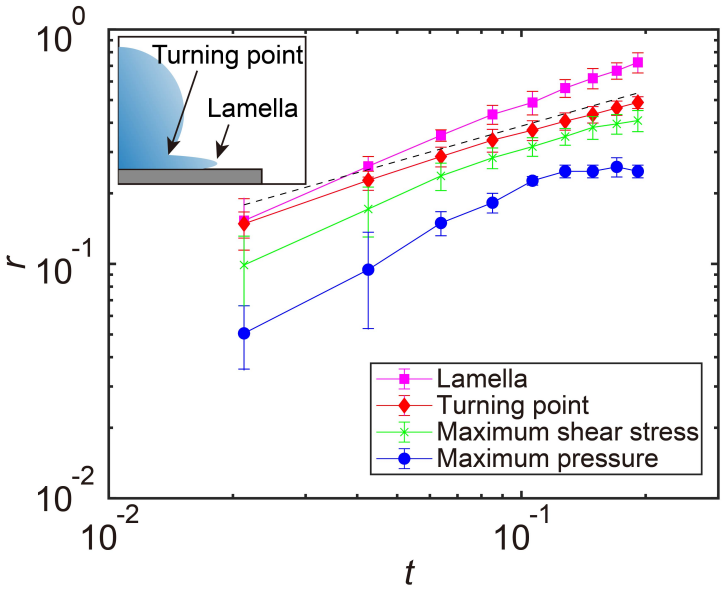

Figure 3.4: Dynamic tracking of the maximum shear stress and the maximum pressure. The position of the lamellar tip, the turning point, the maximum shear stress and the maximum pressure as a function of time. The dashed line indicates $r = \sqrt{6t}/2$. Upper inset: Definition of the kinematic features of an impacting drop.

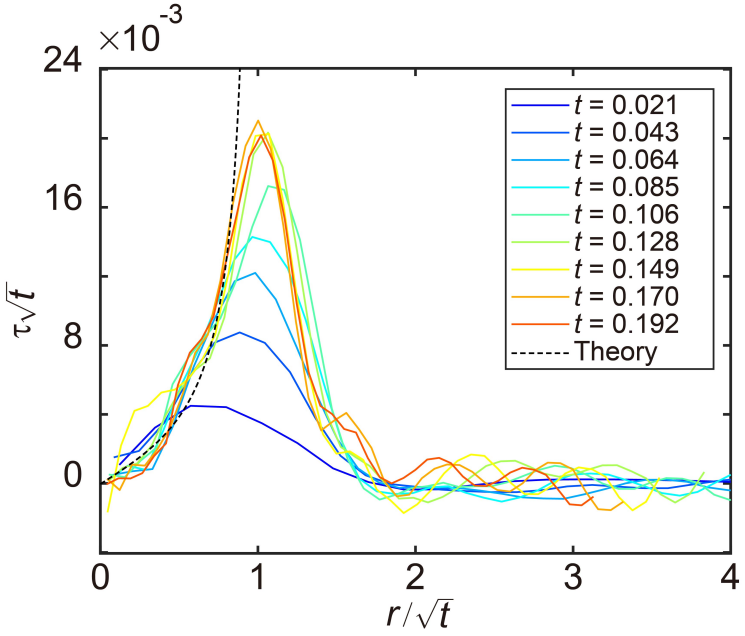

Figure 3.5: Self-similar scaling of the shear stress. The rescaled surface shear stress $\tau/\sqrt{t}$ as a function of the rescaled radial position $r/\sqrt{t}$. The dashed line is the prediction of Equation 3.21 with the modified scaling function $f(x)$. Oscillations of shear stress can be identified above $t_c = 0.106$ at large r.

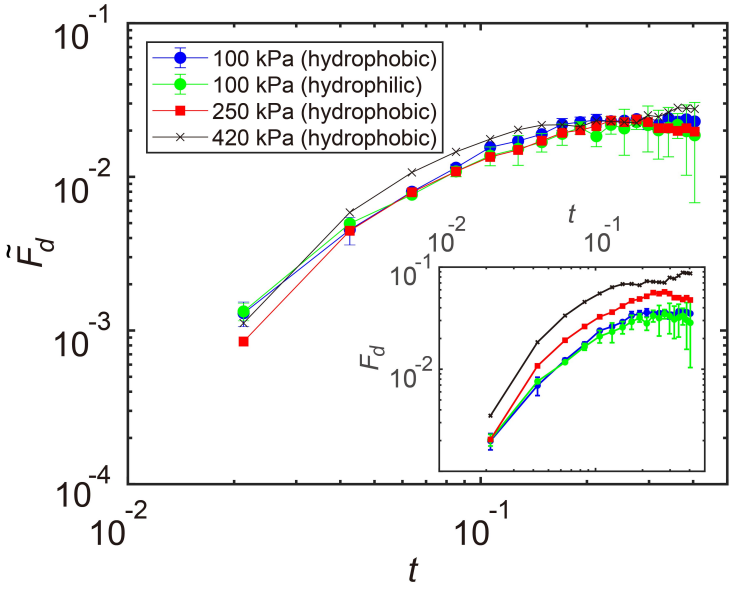

Figure 3.6: The shear force on the impacted surface $F_d(t)$. While the inset shows the dimensionless force F_d scaled by $\rho U^2 D^2$ suggested by the self-similar theory [47], the main plot shows the dimensionless force F_d scaled by $E^{1/2}(\rho U 2)^{1/2} D^2$ based on our theoretical analysis of deformable substrates (Section B.6).

the downward vertical direction within the drop body to the horizontal radial direction inside the narrow lamella. Beyond the maximum, the shear stress induced by the boundary layer of the fast expanding lamella decreases with increasing r [89]. While $r_c(t)$ follows the well-established square-root scaling $r_c(t) = \sqrt{6t}/2$ [66, 46], $r_\tau(t)$ shows a similar square-root scaling but with a slightly smaller prefactor $r_\tau = \sqrt{t}$.

Based on an analogy of the structure of the boundary layer in the trail of a shock-wave, Philippi *et al.* proposed that the shear stress of incompressible drops on infinitely rigid substrates possesses a self-similar structure when $t \to 0^+$ [47],

$$\tau(r, z = 0, t) = 2\sqrt{\frac{6}{\pi^3 Re}}\frac{1}{\sqrt{t}} f(\frac{r}{\sqrt{t}}) \text{ for } r \leq r_c(t), \tag{3.21}$$

where $f(x) = x/(3 - 2x^2)$. $\tau(r, t)$ is non-dimensionalized by ρU^2 and exhibits a finite-time singularity at $r_c(t) = \sqrt{6t}/2$. To verify the self-similar hypothesis, we plot $\tau\sqrt{t}$ versus $\sqrt{t}$ of our experimental results (Figure 3.5), which shows a good collapse at small r away from the singular region. With a modified scaling function $f(x) = x/(1 - x^2)$ to count the different temporal scalings of r_c and $r_\tau = \sqrt{t}$, the collapsed data quantitatively agrees with Equation 3.21 (the dashed line in Figure 3.5).

By integrating the shear stress over the contact area, we also obtain the shear force F_d of drop impact,

$$F_d(t) = 2\pi \int_0^{r_{lm}} \tau(r, z = 0, t) r dr, \tag{3.22}$$

which quantifies the erosion strength of drop impact. $F_d(t)$ is independent of the wettability of the impacted surface, but increases with Young's modulus following a scaling $F_d \sim \sqrt{E}$ within the range of our experiments $E = 100$ kPa to $E = 420$ kPa (Figure 3.6). F_d of the drop impact is substantially larger than that of the solid-sphere impact at early times at $E = 100$ kPa (Figure B.4).

3.3.2 Pressure of Drop Impact

Although subject to larger experimental errors due to the nearly incompressibility of PDMS, the pressure (i.e. normal stress) distribution $p(r)$ underneath impacting drops is also measured with high-speed stress microscopy. Similar to the shear stress, we observe a noncentral pressure maximum propagating radially with the spreading drop

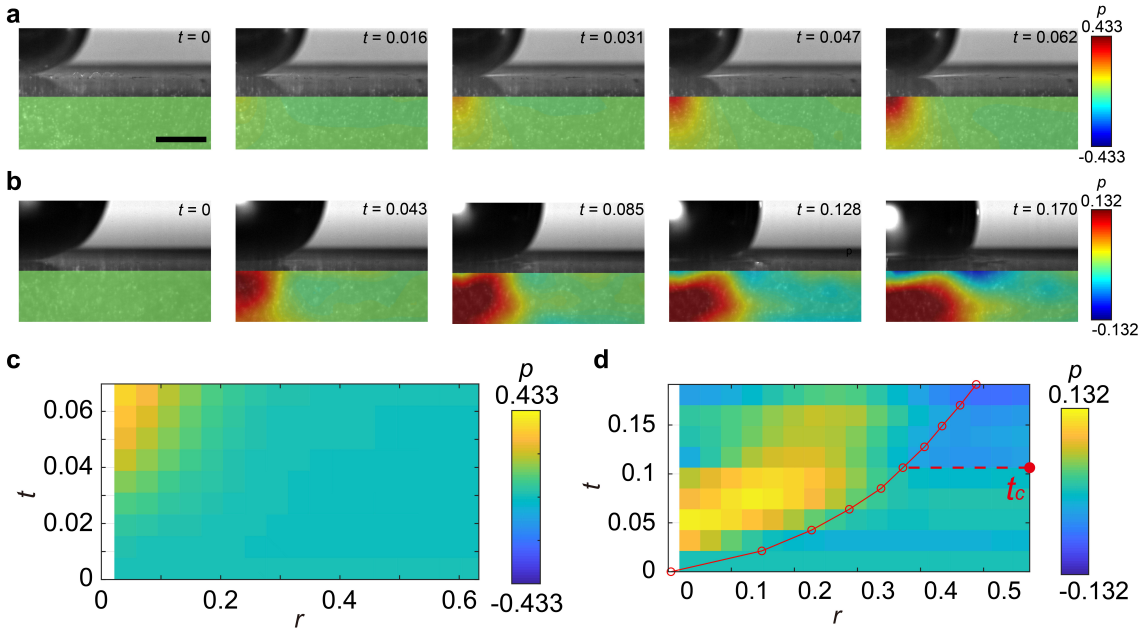

Figure 3.7: Pressure distribution of solid-sphere impact and drop impact. (a), (c), The temporal evolution of the pressure $p(r, z, t)$ and the spatiotemporal diagram of the surface pressure $p(r, z = 0, t)$ of the impacting steel sphere. p is nondimensionalized by $E^{4/5}(\rho U^2)^{1/5}$. (b), (d), The temporal evolution of $p(r, z, t)$ and the spatiotemporal diagram of $p(r, z = 0, t)$ of the impacting drop. p is non-dimensionalized by ρU^2. The impact conditions are specified in the text. The red line in (d) indicates the position of the turning point. The time when the negative pressure emerges $t_c = 0.106$ is also indicated. Scale bar: 1 mm.

(Figure 3.7(b) and (d)). The dynamics are again in sharp contrast to the pressure of solid-sphere impact, where the maximum impact pressure is fixed at $r = 0$ (Figure 3.7(a) and (c)). Thus, our experiments provide unambiguous evidence on the existence of the counterintuitive noncentral pressure maximum predicted by drop-impact theories [113, 39, 47]. To the best of our knowledge, our study provides the first experimental evidence on the existence of propagating off-axial pressure maximum during drop impact. Nevertheless, the maximum pressure falls behind the maximum shear stress (Figure 3.4), a feature unexpected from the self-similar theory with infinitely rigid substrates [47].

3.3.3 Shock Wave

More interestingly, a negative pressure emerges in front of the turning point r_c at t_c = 0.106 (Figure 3.7(b) and (d)). Above t_c, both shear stress and pressure show clear oscillations at large r (Figure 3.5). Consistent with the stress measurements, we also observe the oscillation of the radial displacement of the gel surface, $u_r(r,t)$, at large r above t_c (Figure 3.9(b)), suggesting the formation of a surface acoustic wave in the gel—the classic Rayleigh wave—driven by the maximum pressure and shear stress near r_c. The speed of the turning point can be calculated through the derivative of $r_c(t)$ with respect to time:

$$\frac{dr_c}{dt} = \frac{\sqrt{6}}{4} t^{-1/2}. \tag{3.23}$$

Since the speed of the turning point V_c as $t \to 0^+$, the stress maxima spread supersonically at short times (Figure 3.8). Thus, a shock front forms near r_c on the impacted surface when $t < t_c$. The surface wave overtakes the turning point above t_c, releasing the Rayleigh wave in front of the spreading drop in an explosion-like process. The speed of the surface wave can be estimated as 1.88, which quantitatively matches the speed of the Rayleigh wave [114]

$$V_R = \frac{1}{M}\left[\sqrt{\frac{1}{2(1+\nu)}}\frac{0.862 + 1.14\nu}{(1+\nu)}\right] = 1.89 \tag{3.24}$$

Here, the Mach number $M \equiv U\sqrt{\rho_S/E} = 0.292$. $\rho_S = 0.965$ g/cm^3 and $\nu = 0.49$ are the density and Poisson's ratio of PDMS, respectively. Without the shock process, the Rayleigh wave of solid-sphere impact is much weaker and inconspicuous in comparison

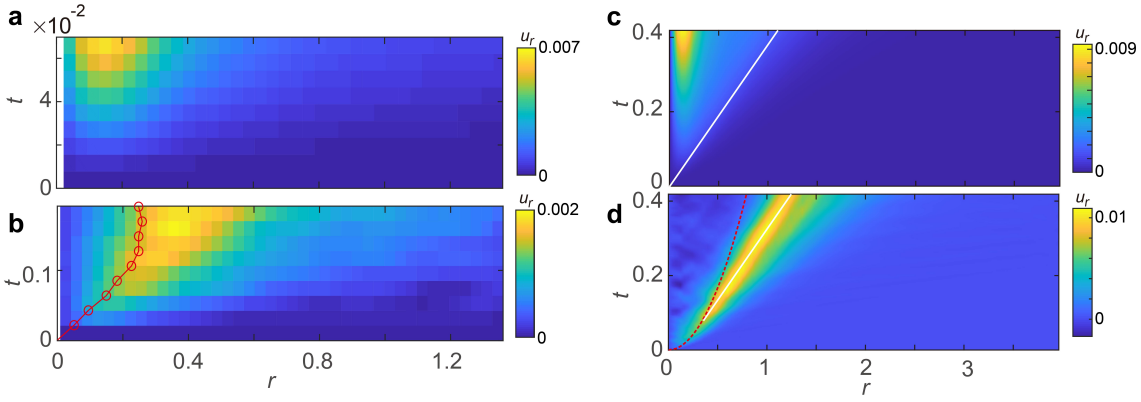

Figure 3.8: (a), (b), The spatiotemporal diagram of the radial displacement of the gel surface $u_r(r,t)$ induced by the impact of the steel sphere (a) and the liquid drop (b). u_r is normalized by the diameter of the impactors D. (c), (d), The numerical solution of $u_r(r,t)$ by the impact of the steel sphere (c) and the liquid drop (d). The red lines in (b) and (d) indicate the position of the maximum pressure that drives the surface wave, whereas the white lines in (c) and (d) indicate the propagation of the Rayleigh wave emitting at $t = 0$ and $t_c \approx 0.1$, respectively. For the complete solution of the surface waves, see Figure B.5.

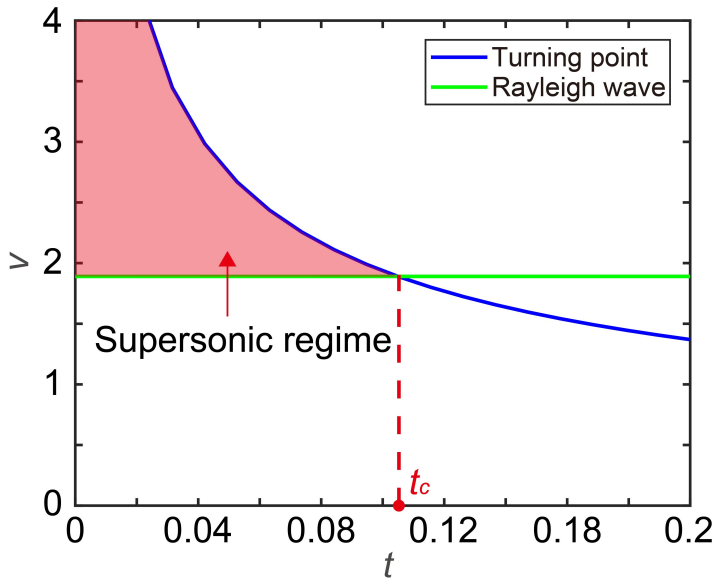

Figure 3.9: Competition between the speed of the turning point V_c and the speed of the Rayleigh wave V_R. The supersonic regime before t_c, where $V_c > V_R$, is indicated.

(Figure 3.9(a)).

Encouraged by the agreement between Equation 3.21 and experiments, we couple the theoretical impact pressure and shear stress of incompressible drops on infinitely rigid surfaces with the Navier-Lamé equation of semi-infinite elastic media (Section B.6). After non-dimensionalizing the governing equation and the boundary conditions, the results become independent of M in terms of the dimensionless variables. Particularly, the shear force scales as $F_d \sim E^{1/2}(\rho U^2)^{1/2}D^2$, agree with our measurements at different E (Figure 3.6). The numerical solution of the coupled equations qualitatively reproduces the formation of the shock-induced Rayleigh wave in drop impact, where a sharp surface wave with a well-defined peak emerges at $t_c \approx 0.1$ and propagates with V_R (Figure 3.9(d)). In contrast, the surface wave of solid-sphere impact emits continuously from a stationary source and is therefore much smoother and diffusive (Figure 3.9(c)).

3.4 Conclusion

Our high-speed stress microscopy reveals three unique dynamic features of drop impact, which may contribute to its unusual ability to erode solid substrates. (i) The stress distributions of impacting drops are spatiotemporally highly non-uniform. The radially propagating stress maxima simultaneously press and scrub impacted substrates, leading to a larger erosion area and a higher shear force. (ii) Because of the divergent speed of the turning point, a shock wave forms on impacted substrates at short times, which substantially increases the erosion strength. Each impacting drop behaves like a tiny bomb, releasing its kinetic impacting energy explosively. (iii) A sharp shock-induced surface wave finally emerges from the explosion process, weakening the cohesion of surface materials before the arrival of the shear stress maximum.

It is worth of noting that shock propagation including that within impacting drops and along impacted surfaces has been extensively investigated theoretically for compressible drops with the liquid Mach number $U/C \sim \mathcal{O}(1)$, where C is the speed of sound in liquid drops [38]. Nevertheless, the shock process of incompressible drops with $U/C \ll 1$ relevant to most natural and industrial processes [67, 65, 25] has not been realized and discussed heretofore. Thanks to low impact speeds, we are able to examine the propagation of drop-impact-induced surface shock in real time experimentally,

crucial for understanding the erosion of drop impact. Finally, the use of high-speed microscopy demonstrates its potential to measure the impact stress of liquid drops in diverse situations such as drop impact on patterned substrates, at low ambient pressures and with non-Newtonian drops [27, 26].

Chapter 4

Drop Impact on Micropatterened Surfaces

4.1 Introduction

With the advance of technology in recent decades, surfaces with various properties have been created. Biomimetic materials inspired by lotus leaves, spider silks, butterfly wings are the typical examples [115]. Studying drop impact on these kinds of surfaces has lots of potential applications, such as self-cleaning, spray coating, and anti-icing of airplane wings [26]. The general way of modification is changing topography and varying wettability of surfaces. So far, the literatures mainly focus on the how the textures affect the kinematics of drop impact. For examples, the surface roughness plays the role in splashing [35, 116]. The scaling of the maximum spreading radius is also examined [117, 118, 52]. In addition, many studies have investigated the characteristics of retract, rebound, jet of drops impacting on superhydrophobic surfaces at different We, Re, impact velocities, and surface properties [119, 120, 121, 122, 123, 124, 56, 54, 55]. In particular, Chen *et al.* concluded that as Re and We increase, the orders of the regimes of outcomes would be regular rebound, jetting, partial rebound, and splashing [125]. Patil *et al.* stated that as the impact velocity of a drop increases, the Cassie to Wenzel state occurs in which the liquid penetrates the grooves between pillars. The outcomes of rebound or non-rebound corresponds to non-penetration or complete penetration of liquids [126].

Despite these extensive studies, there are still few literatures discussing how the textures of surfaces affect the stress distribution of drop impact due to the difficulty of simulations and analytical derivations. The structure of substrates is a crucial parameter related to erosion or damage on coatings or substrates [127]. Exploring the effects of desired modifications on stress distribution measurements can finally be achieved through the experiments. Here, we perform photolithography to synthesize the polymer gel with arrays of micropillars on its surface. The novel technique"high-speed stress microscop" is applied to obtain the temporal evolution of displacement fields and shear stress fields of drop impact at short times. We compare the difference of displacement, shear stress, and shear force of the micropatterned surface with the smooth surface. The results help to understand how micropatterns mitigate erosion of drop impact.

4.2 Methods

4.2.1 Preparation of Micropatterned PDMS Substrates

In order to have the micropatterned structure on the surface of substrate, soft lithography is one of the most common technique to fabricate the mold. Here, SU-8, an epoxy negative photoresist, was served as the master mold for the patterned template. Firstly, a clean 4 inch Si wafer was prepared, and 4 mL of SU-8 2010 was dispensed on the wafer. The spin coating of SU-8 is processed in two steps: (1) 500 rpm for 10 s and then (2) 2000 rpm for 30 s. The thickness of the film was 14 μm. The SU-8-coated wafer was placed on a hotplate for soft baking at 95°C for 3 mins. A soda lime photomask of arrays of circular shape patterns was used for SU-8 exposure. The circles were 20 microns in diameter with a 40-micron pitch. The pattern was transferred to sample through exposure of UV radiation with a mask aligner (K2 Aligner Suss MABA6,) in the soft contact mode. The dose of exposure energy was 60 mJ. After the exposure, the post exposure bake was directly applied at 75°C for 2.5 mins. Afterwards, the sample was immersed in SU-8 developer (Propylene glycol monomethyl ether acetate) for 3 mins in order to dissolve the uncrosslinked parts, and then followed by rinsing with isopropyl alcohol. After the air dry, the hard bake was incorporated at 100°C. Through these processes, the structure of arrays of holes with the diameter = 20 μm and the depth = 14 μm was obtained (Figure 4.1).

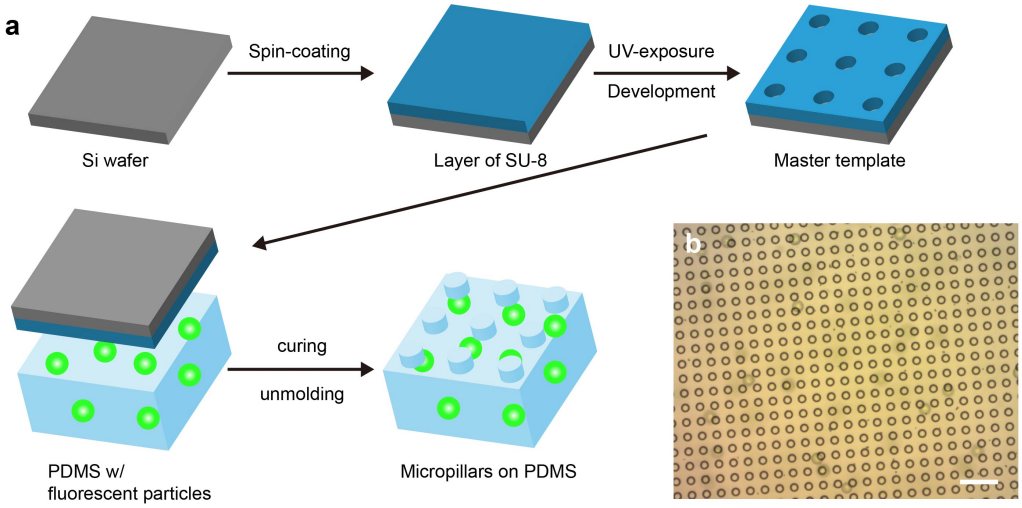

Figure 4.1: Schematic diagram of synthesizing micropatterned PDMS. (a), The process of synthesizing the micropatterned PDMS by applying photolithography to manufacture the master template on a Si wafer. (b), Optical microscope image of the surface of micropatterned PDMS. Scale bar: 100 μm.

Polydimethylsiloxane (PDMS) elastomers were prepared from two-part Sylgard 184 silicone elastomer kits (Dow Corning). To adjust the Young's modulus, E, of the cured PDMS gels, we mixed siloxane monomers with crosslinkers at a controlled mass ratio. In the experiments reported in this paper, we used a monomer-to-crosslinker mass ratio of 30:1, which yielded PDMS gels of $E = 100$ kPa. Florescent polystyrene (PS) particles of diameter 30 μm (ThermoFisher) were mixed into the two-part PDMS mixtures at a controlled volume fraction of 0.23% before curing. The PDMS-particle mixture was finally vacuumed to remove air bubbles. Subsequently, the SU-8 coated wafer was placed on the top of a container of PDMS-particle mixture, and all of them were placed in an oven at 90°C overnight for curing of PDMS. The fully cured gels have a fixed thickness of 6.5 mm and an area of 24 $\times$ 24 mm^2, and have the micro-patterned pillars with the diameter = 20 μm and the height = 14 μm. The surface area is much larger than the maximum spreading area of impacting drops.

4.2.2 Calculations of Displacement Fields and Shear Stress Fields

The fluorescent PS particles embedded in the PDMS gels were served as tracer particles. Through tracking the motion of tracer particles, the deformation of the gels under impact can be obtained. We used Particle Image Velocimetry (PIV) algorithm (PIVlab, Matlab) to obtain the temporal evolution of displacement fields of the gels [110]. An interrogation window of 384 μm $\times$ 384 μm with 70% overlap was adopted in PIV, which gave a spatial resolution of 115 μm. The temporal resolution is 0.025 ms, which is set by the frame rate of high-speed photography. The first frame which is at $t = 0$ was set to be the reference frame. That means, each frame at different moments was cross-correlated with the first frame.

The displacement fields derived from the PIV analysis are discrete; furthermore, the strain fields and the stress fields are the derivative of the displacement fields. Therefore, it is necessary to apply the smoothing process in order to reduce the effects of noises due to differentiation. Here, we used the moving least-square (MLS) method to construct continuous and differentiable displacement fields fitted by polynomial functions:

$$\mathbf{g}(\mathbf{x}) = \mathbf{P}^T(\mathbf{x})\mathbf{a}(\mathbf{x}) \tag{4.1}$$

where the interpolation function $\mathbf{g}(\mathbf{x})$ is the fitting displacement fields, $\mathbf{P}^T(\mathbf{x})$ is a polynomial basis and $\mathbf{a}(\mathbf{x})$ is the corresponding coefficients of the basis. Because of the geometry of the impact, we set the impact point at $(r, z) = (0, 0)$. In this experiment, we chose a cubic polynomial basis, so $\mathbf{P}^T(\mathbf{x})$ and $\mathbf{a}(\mathbf{x})$ are.

$$\mathbf{P}^T(\mathbf{x}) = [1, r, z, r^2, z^2, rz, r^3, z^3, r^2z, rz^2], \tag{4.2}$$

$$\mathbf{a}(\mathbf{x}) = [\mathbf{a_0}(\mathbf{x}), \mathbf{a_1}(\mathbf{x}), \mathbf{a_2}(\mathbf{x}), ..., \mathbf{a_9}(\mathbf{x})]. \tag{4.3}$$

Following the same derivation in Reference [111] and Equation 3.6-3.8, The solution of the interpolation function $\mathbf{g}(\mathbf{x})$ gives

$$\mathbf{g}(\mathbf{x}) = \mathbf{P}^T(\mathbf{x})\mathbf{a}(\mathbf{x}) = \mathbf{P}^T(\mathbf{x})\mathbf{A}^{-1}(\mathbf{x})\mathbf{B}(\mathbf{x})\mathbf{w} \tag{4.4}$$

wheres $\mathbf{w}$ is the discrete displacement fields obtained from PIV.

With the help of the MLS method, the continuous displacement fields can be obtained, and the strain fields can be calculated by taking the spatial derivative to the interpolation polynomial functions $\mathbf{g}(\mathbf{x})$, where the component vectors of $\mathbf{g}^T = [g_r, g_z, g_\theta]$ are in the r, z and θ direction, respectively. Because the deformation of the substrate is small in this study, we adopted the assumption of linear elasticity. Because of the patterned structure on the surface of the substrate, strictly the impact geometry in this study cannot be regarded as axisymmetry. However, for the plane which passes through the origin where the center of the impacting drop is, The shear strain-displacement relation still can be expressed as:

$$\epsilon_{rz} = \frac{1}{2}[\frac{\partial g_r}{\partial z} + \frac{\partial g_z}{\partial r}]. \tag{4.5}$$

Following the linear elastic and isotropic model, the shear stress-shear strain relation which is also known as the generalized Hooke's law is:

$$\sigma_{rz} = 2G\epsilon_{rz}, \tag{4.6}$$

where G is the shear modulus. In this study σ_{rz} is denoted as τ.

4.3 Results and Discussion

We adopted the idea of the technique "high-speed stress microscopy" which has been introduced in Section 3.2. An elastic gel made of cross-linked polydimethylsiloxane (PDMS) gel is served as the substrate. Dilute fluorescent particles of diameter 30 μm with the volume percent 0.23% were embedded in the gels during crosslinking, and these particles are tracer particles to track the deformation of the substrate induced by drop impact. We prepared two kinds of gels with different surface properties: smooth surfaces and micropatterned surfaces to compare how microstructures affect the shear stress distribution. The laser sheet of 30 μm thickness shone from the side of the gel illuminated the fluorescent tracer particles within the laser sheet plane and the laser sheet was finely adjusted to go through the center of the impacting drop. A high-speed camera pointing perpendicular to the sheet focusing on the sheet is then used to image the motions of tracer particles at 40,000 frames per second. We applied the PIV analysis to quantify the images to obtain the temporal evolution of the deformation of the gel under impact. Subsequently, the resulting displacement fields at different moments are processed to calculate the temporal evolution of the stress distributions within the gel (Section 4.2.2). The PDMS gel with a smooth surface is intrinsically hydrophobic with the contact angle $\sim 90°$. With the help of micropillars on the surface, the gels approach to superhydrophobic. The Young's modulus of the gel was controlled at $E = 100$ kPa in this study, so that the deformation of the gel is large enough to be accurately measured by the PIV analysis, but small enough that the impact process of liquid drops is not strongly affected by the deformation at the surface.

In the experiment, we mixed sodium iodide with water as the liquids of drops (60% in weight concentration) to increase the impact force of drop impact. The viscosity μ and the surface tension σ of a sodium aqueous solution are the same as water, and the density ρ, the diameter D, and the impact velocity U are $\rho = 2200$ kg/m^3, $D = 3.49$ mm, and $U = 2.97$ m/s, which give a Reynolds number $Re = \rho U D/\mu = 22,800$ and a Weber number $We = \rho D U 2/\sigma = 940$. Therefore, in this case the impact is dominated by inertia, and we focus on the discussion in the initial impact regime. In the following we report the variables in dimensionless forms by using D and D/U to scale the length and the time, respectively.

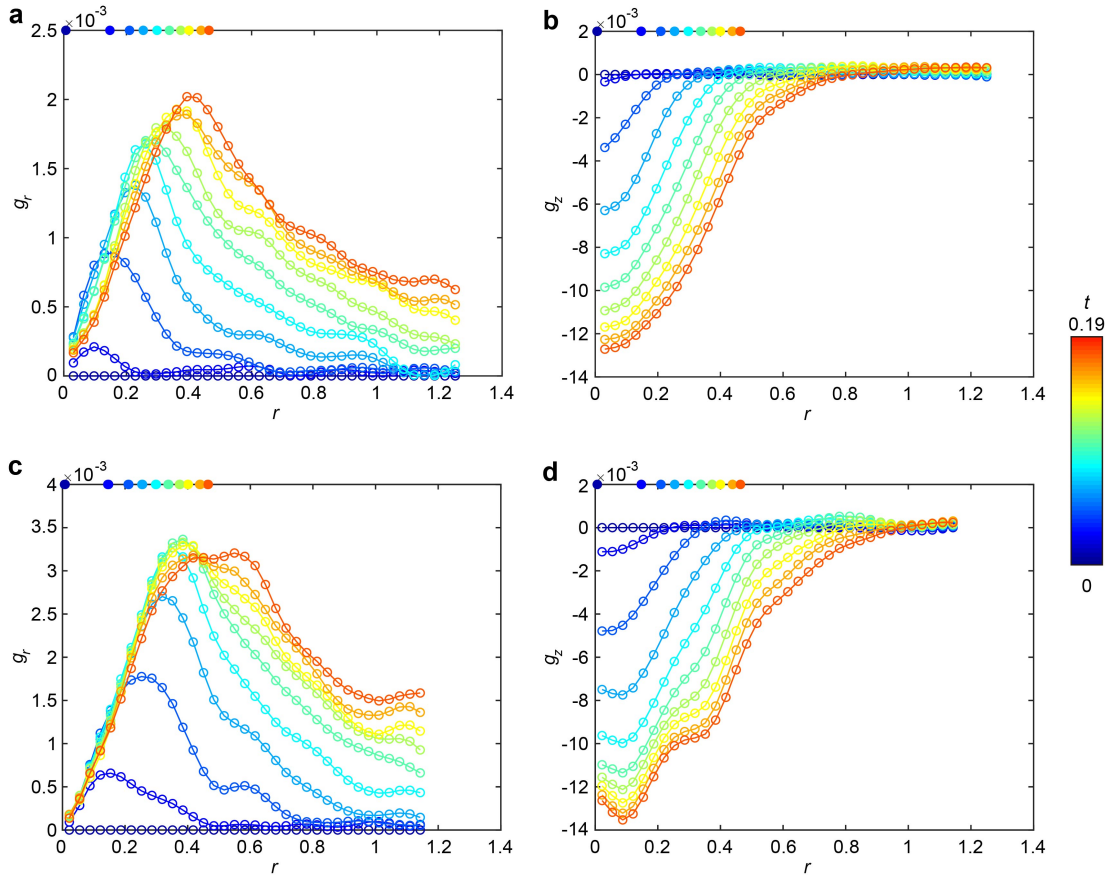

Figure 4.2: Displacement distribution of drop impact on the smooth and the micropatterned PDMS. (a), (c), g_r near the impacted surface of the smooth and micropatterned PDMS, respectively. (b), (d), g_z near the impacted surface of the smooth and micropatterned PDMS, respectively. The solid circles represent the position of the turning point at different times.

4.3.1 Displacement Fields of Drop Impact of Patterned Surfaces

Figure 4.2 compares the temporal evolution of the displacement distribution of drop impact near the impacted surface of the smooth and the micropatterned PDMS at early times. $t = 0$ is defined as the moment when an impacting drop contacts with the surface of gels. We decompose the displacement vector into the vector in the r-direction g_r and in the z-direction g_z. For both cases, they have the same trend that the position of the maximum g_r propagates radially with the spreading of an impacting drop, If we correlate the position of the maximum g_r with the kinematic features of the shape of an impacting drop including the lamella r_{lm} and the turning point r_c, it demonstrates that the the maximum g_r of both cases follows r_c (Figure C.2). r_c is the location where the large momentum redirects from the vertical direction to the horizontal direction. It is noted that r_{lm} and r_s are independent of the surface properties at the initial impact regime, and in the both cases r_s follows the scaling $r_s = \sqrt{6t}/2$, which is consistent with the theories and experimental results [128, 48] (Figure C.1). Differently, the the position of the maximum g_z is fixed at the $r = 0$ where is at the impacting point.

However, if we compare the magnitude of the displacement field, although there is no apparent difference for g_z, it shows that g_r of the micropatterned surface is larger than the smooth surface. During the spreading of an impacting drop on the surface of the gel, the liquid inside the drop flows out radially. Therefore, the bending of pillars on the patterned surface leads to stretch the substrate outward in r-direction.

4.3.2 Shear Stress of Drop Impact of Patterned Surfaces

Through Equation 4.6, the distribution of the shear stress τ can be derived from the displacement fields. Figure 4.3$(a)(b)$ compare the temporal evolution of the shear stress of the smooth surface and the patterned surface. In the early time, the non-uniform shear stress with a non-central peak develops in both cases. For the case of the smooth surface, the shear stress profile remains the bell-shaped all over the initial impact regime. It lasts until entering the spreading regime that the peak splits into two peaks at $t = 0.3$. In addition, the magnitude of the maximum shear stress increases and then decreases monotonically. However, for the case of the micropatterned surface, the shape of the

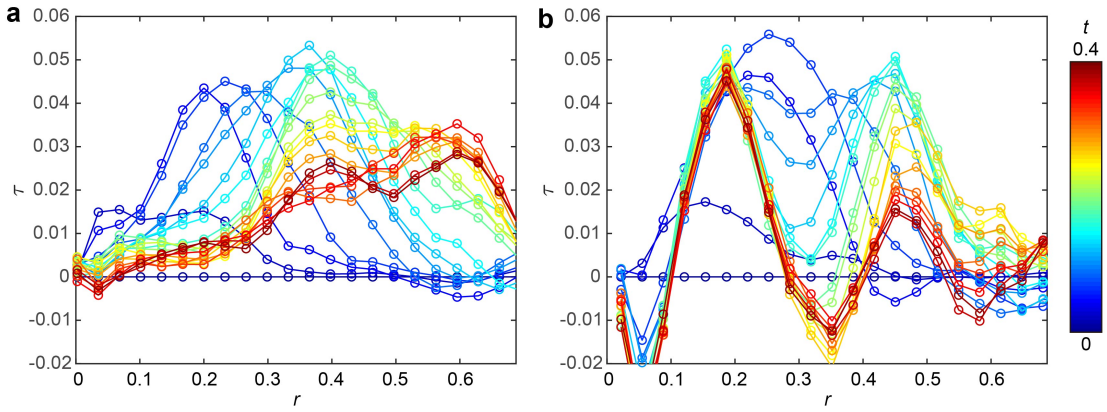

Figure 4.3: Shear stress distribution of drop impact on the smooth and micropatterned PDMS. (a), The shear stress distribution of the smooth surface. The shape of curves remains bell-shaped until $t = 0.3$. (b), The shear stress distribution of the micropatterned surface. The curve begins to be flatten at $t = 0.07$, and then splits into several peaks.

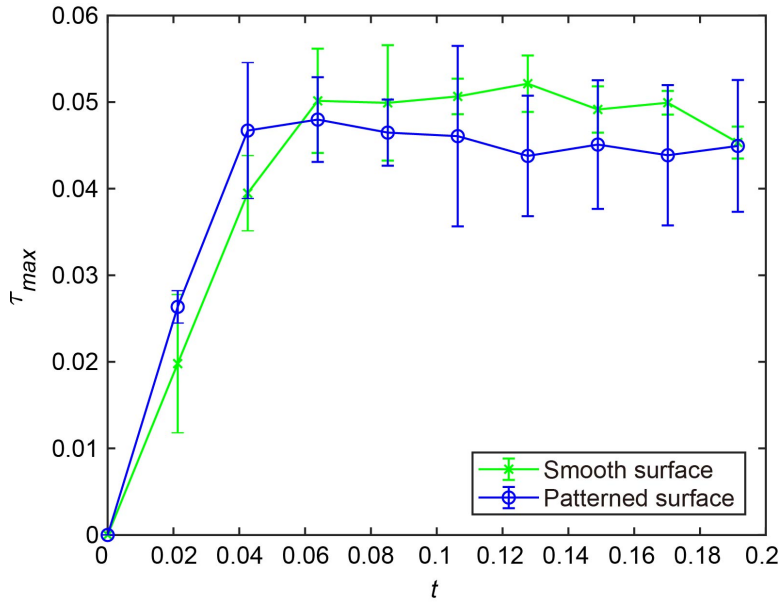

Figure 4.4: Maximum shear stress of drop impact of the smooth and the micropatterned PDMS. Before $t = 0.07$, the growth of τ_{max} is roughly the same for both case. After that, τ_{max} is smaller of the patterned PDMS.

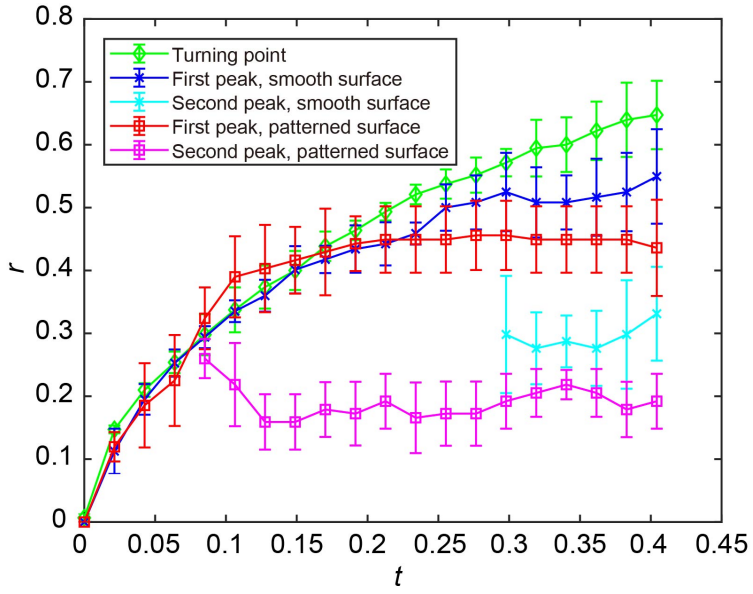

Figure 4.5: Dynamics of the maximum shear stress of drop impact on the smooth and the micropatterned PDMS. For τ_{max} of the smooth surface, the second peak appears at $t = 0.3$. For the patterned surface, the second peak emerges at $t = 0.07$.

shear stress curve is bell-shaped only in the beginning. After $t = 0.07$, the peak disappears and the curve becomes flattened even in the initial impact regime. Then it will finally split into two peaks.

Besides, the trend of the maximum shear stress τ_{max} is also different in both cases. Initially, the magnitude of τ_{max} grows similarly in both cases. However, after $t = 0.07$, the mean value of τ_{max} for drop impact on the micropatterned surface is around 10% smaller than that on the smooth surface (Figure 4.4). Based on Figure 4.3, we explore the details of dynamics of τ_{max} shown in Figure 4.5. Initially, the position of τ_{max} of the smooth surface follows the position of the turning point. After $t = 0.3$ which is in the spreading regime, the stress distribution splits into two peaks. One of peaks continues the propagation and we call it the first peak, and the other peak which is the second peak stays at the same location. For τ_{max} of the patterned surface, although before $t = 0.07$ the trend of τ_{max} is the same as the smooth surface, the formation of the splitting peaks happens much earlier. After $t = 0.07$, the first peak propagates with the turning point until $t = 0.17$, and then the position of the first peak does not alter. The position of the second peak is roughly fixed at the same location.

To explain this phenomenon, we propose a hypothesis that the streamlines of the flow inside an impacting drop are not parellel. Most theories propose that the flow either in the initial impact regime or in the spreading regime is lamellar on smooth surfaces [61, 47]. However, in this case of micropatterned surfaces, the flow which propagates radially near the surface is hindered by the micropillars. The flow will change its direction and vortices would generate subsequently (Figure 4.7)(a). To provide a general idea of the patterns of the flow inside a drop, we make a conjecture of the effects of vortices based on the shear stress profiles shown in Figure 4.3(b) and the g_z in Figure 4.2(d). From our measurements, we find that dg_z/dr of the gel is the dominant term in Equation 4.5, either for smooth surfaces or micropatterned surface. The magnitude of $G(dg_z/dr)$ is three times larger than the magnitude of $G(dg_r/dz)$ (Figure 4.6). Therefore, the influence of the pressure and the flow in the vertical direction in an impacting drop play a role, which are the main sources to deform the substrate in the z-direction. As a result, the trend of the shear stress curves is linked to the shape of g_z versus r curves because the derivative would give dg_z/dr. In Figure 4.2(d), the inflection point shows up after $t = 0.07$, and the location of the inflection point corresponds to the valley of

the shear stress curves shown in Figure 4.3(b).

We propose a simple model to simulate the deformation g_z of substrates near surfaces, and explain how vortices affect g_z. When an impacting drop contacts smooth surfaces of substrates, the surface deforms in the negative z-direction with a constant velocity induced by an impacting drop (Figure 4.7)(b). Depending on the position of the spreading lamella, different positions of surfaces begin to deform in different times. g_z equals to the velocity multiplied by impacting time shown in Figure 4.7(d). However, when a drop contacts the patterned surface for a short while ($t = 0.07$), vortices start to form in an impacting drop. The flow of vortices would affect the velocity of surface deformation. Therefore, the net velocity of surface deformation equals a constant velocity plus the velocity induced by vortices in the z-direction (Figure 4.7)(c), and the corresponding g_z shown in Figure 4.7(e) agrees with Figure 4.2(d) for the behavior of curve inflection. We also observe the shear stress of smooth surfaces will split into two peaks in a late time ($t = 0.3$), which also implies that even for smooth surfaces, vortices may form in the spreading regime.

So far, there are very few literatures investigating the flow of drops upon an impact [63, 52, 129]. Additionally, the studies regarding vortices only focus on drop impact on a pool, which the vortices are formed between the interface of the lamella and the water of the pool [130]. Our experimental results of measuring the shear stress shed light on the mysterious flow patterns inside an impacting drop on a solid substrate. Furthermore, it implies that the micropillars cause the formation of vortices, and the non-smoothing flow leads to change the shear stress distribution. It potentially helps mitigate erosion during drop impact.

4.3.3 Shear force of Drop Impact of Patterned Surfaces

Through integrating the shear stress over the contact area between the spreading drop and the surface of the gel, the shear force F_d of drop impact can be obtained:

$$F_d(t) = 2\pi \int_0^{r_{lm}} \tau(r, z = 0, t) r dr. \tag{4.7}$$

It is interesting that although the shear stress distribution of drop impact varies from the micropatterned surfaces to the smooth surface, the temporal evolution of the shear

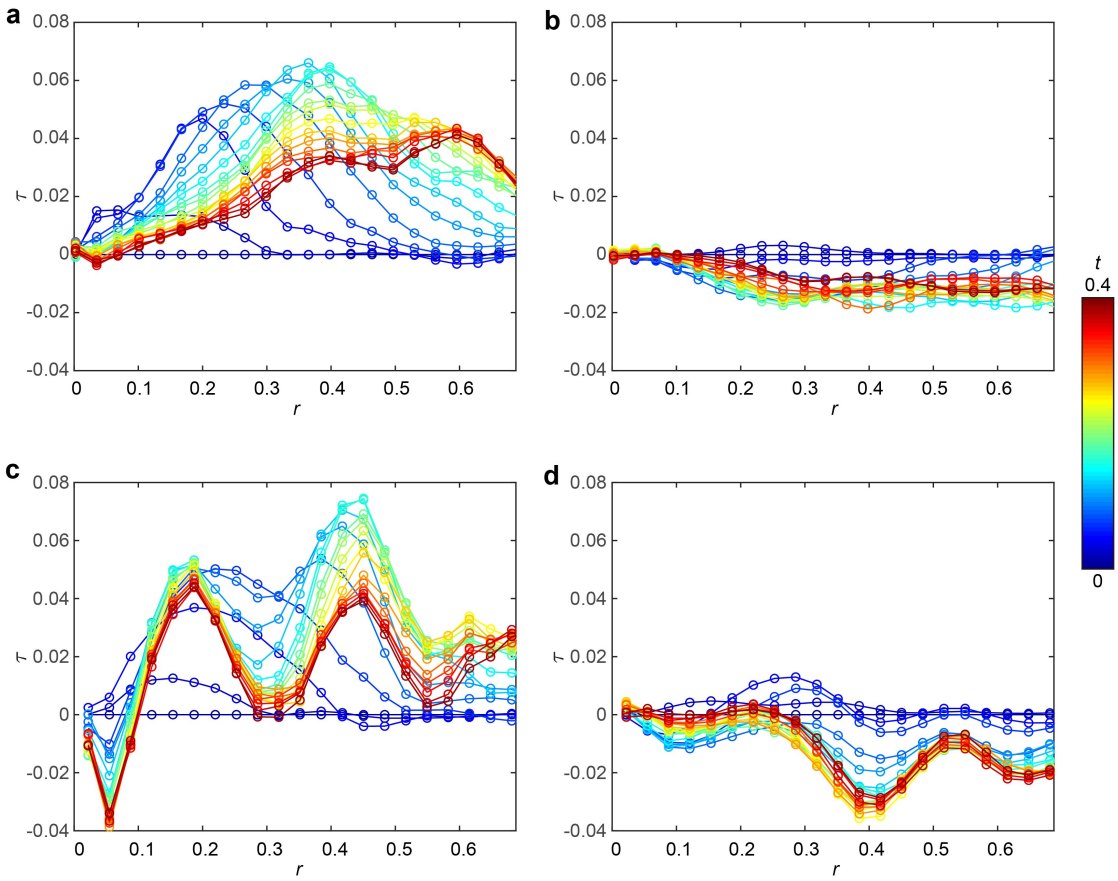

Figure 4.6: Components of shear stress of drop impact. (a), (c), $G(dg_z/dr)$ near the impacted surface of the smooth and micropatterned PDMS, respectively. (b), (d), $G(dg_r/dz)$ near the impacted surface of the smooth and micropatterned PDMS, respectively.

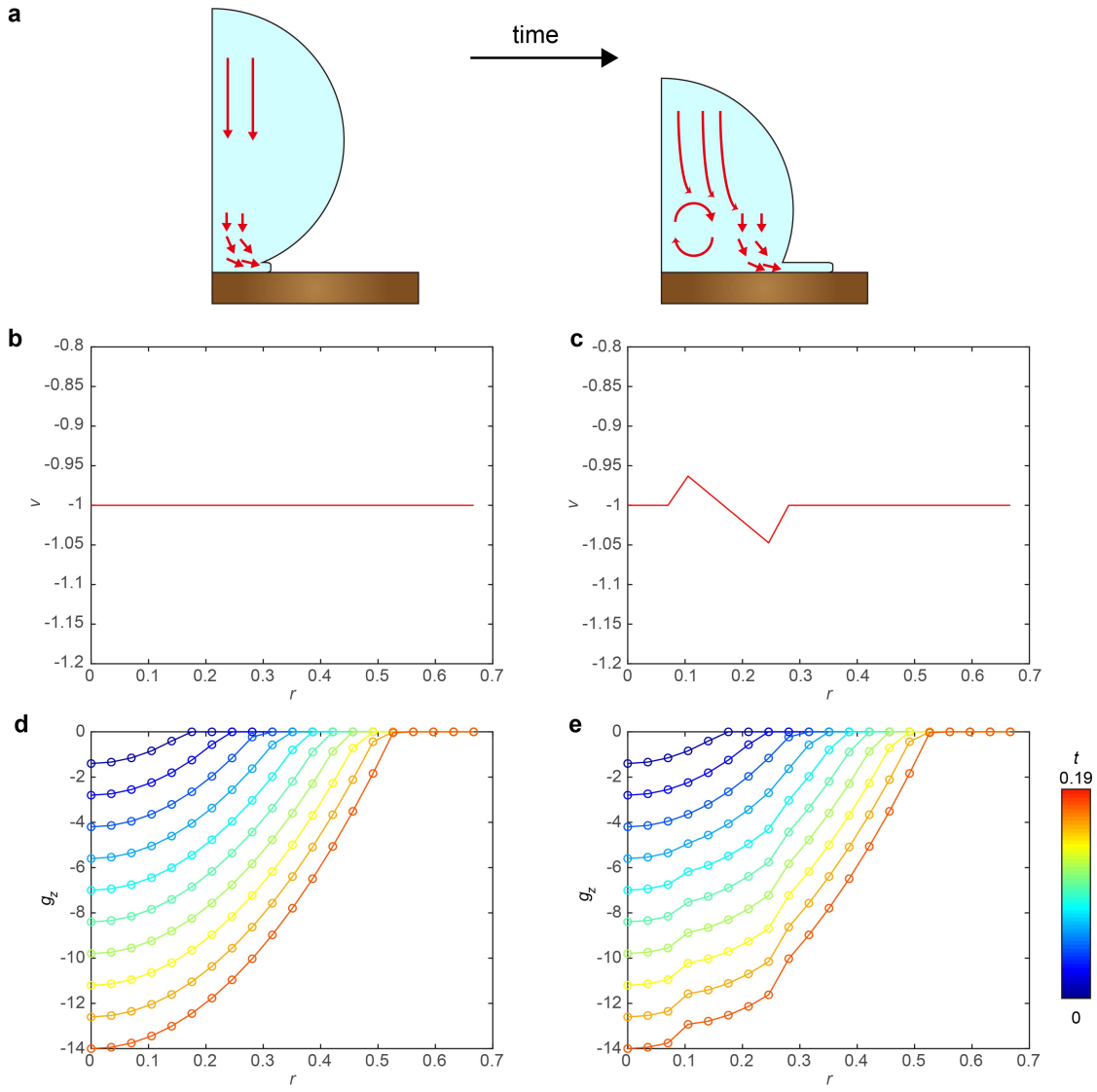

Figure 4.7: Model of vortices affecting the deformation of PDMS. (a), flow patterns of an impacting drop on micropatterned surfaces. (b), (c), the velocity in the z-direction of surface deformation of smooth PDMS (left) and micropatterned PDMS (right). (d), (e), g_z of impacted surfaces of smooth PDMS (left) and micropatterned PDMS (right) derived from the velocity in (b), (c).

force is the same for both cases (Figure 4.8). It means that the area underneath the the curves of the shear stress is still unchanged. The micropillars can reduce the magnitude of the local maximum shear stress, but the total shear force exerting on the surfaces are all the same.

In this experiment both Re and We are very large. Based on the previous studies, in this condition an impacting drop would contact the surface of patterned gels, which is regard as the impacting Wenzel state [125]. The liquid of the drop is complete penetration to fill the grooves of patterned surfaces because the dynamic pressure exceeds the capillary pressure across the interface of liquids and solids [126, 94]. This situation may be the reason that the shear force of the patterned are the same as that of the smooth surface. In contrast, if we decrease Re and We of the impacting drop or increase the roughness by making the height of micropillars higher, the liquid would not penetrate to the grooves, which is the Cassie state. Then there will be a layer of air between a drop and a substrate, and the contact area between the drop and the surface of substrate decreases. With an analogy to the leidenfrost drop impact where there is a vapor layer preventing the drop contacting the substrate [31], the shear stress and shear force between the drop and the substrate may decrease [131, 132, 133].

4.4 Conclusion

High-speed stress microscopy enables us to measure the stress distribution of drop impact under complicated conditions. Through photolithography, we manufactured a polymer gel with micropillars on its surface. We investigate how the dynamic features including the temporal evolution of the displacement distribution, the shear stress distribution, and the shear force of substrates varies from drop impact on smooth surfaces to on micropatterned surfaces at high Re at early times. We found that although some kinematic features such as the positions of the lamella and the turning point are not different in both cases, the shear stress distribution varies after a very short time. The reason may result from that the flow near the substrate inside the drop is not smooth, and the phenomenon could be caused by the formation of vortices. We hope the conjecture of the vortex structures inside an impacting can be verified through laser induced fluorescence (LIF) or particle image velocimetry (PIV).

Our works pose a potential direction on examining the detailed features of the dynamics of drop impact. The flow patterns inside an impacting are extremely hard to be seen and measured directly, and all the statements related to the flows so far are only proposed by theories. From the experimental measurements of the shear stress, the results link the relationship among the shear stress, the boundary layer, and the velocity of the flow inside an impacting drop. Through observing the temporal evolution of shear stress distribution, we can deduce that whether the flow is smooth or not and how the incontinuous structures of flows change as function of the time and the position.

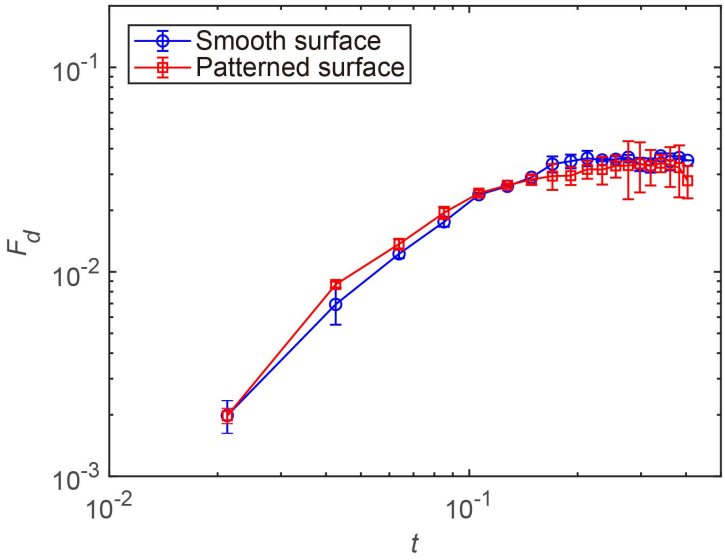

Figure 4.8: The shear force on the smooth and the micropatterned PDMS. The dimensionless shear force F_d here is scaled by $\rho U^2 D^2$.

Chapter 5

Conclusion and Outlook

5.1 Summary

In summary, dynamics of drop impact have been studied experimentally in this research. As we state in the beginning, studying drop impact is important to the issue of erosion in nature and industrial processes. Although extensive studies have been conducted in probing the kinematics of drop impact across a large control parameter spaces, the impact force and the stress distribution are still far from fully understood. Firstly, through synchronizing high-speed imaging and the fast force sensory, we experimentally measured the temporal evolution of impact force of drop impact over a wide range of Re by matching the prediction of the impact force. We verified the existence of self-similar pressure fields at the initial impact regime at high Re. In addition, we also quantitatively analyzed the early-time scaling of the impact force of drops at the different regimes of Re and our theories fit the experimental data very well.

The next step is to explore the details of the dynamic features-the pressure and the shear stress distribution of drop impact. However, to the best of our knowledge, there is no available setup to measure the stress distribution of drop impact on a smooth surface. Therefore, we developed the novel technique "high-speed stress microscopy" to measure the pressure and the shear stress fields of the substrate induced by drop impact. We observed the non-centered maximum pressure and shear stress propagate radially, which agrees with the previous arguments from simulations and theories. Moreover, we also discovered the formation of a shock wave on impacted substrates at short times.

These two features may contribute to the high erosion efficiency by drop impact.

Furthermore, high-speed stress microscopy finally enables us to probe into the stress distribution of drop impact under complicated conditions, which is challenging to be derived through simulations or analytical calculations. We examined drop impact on patterned substrates, and the results demonstrated that the shear stress distribution near the impacted surface would be changed. The magnitude of the maximum shear stress on the micropatterned surface is lower than that on the smooth surface, which implies that the micropillars on impacted surfaces may mitigate erosion from drop impact. Though the mechanism is still under exploration, we hypothesize that vortices are generated inside an impacting drop due to micropillars. This research provides a possibility to map the detailed flow patterns inside an impacting drop, which is very difficult to be visualized.

5.2 Outlook

We have studied the temporal evolution of the impact force and stress distribution of drop impact. Despite the progress, the existing studies concerning the dynamics of drop impact force mainly focus on the most simple type of drop impact: Newtonian drop impact on smooth solid surfaces. Therefore, it requires further efforts to explore the impact force and the stress distribution under different impact conditions. For example, how important parameters including the texture of impacted surfaces, non-Newtonian drop impact, the impact angle of impinging drops, and the pressure of ambient gases affect the stress of drop impact have not been systematically studied. Understanding the influence of these parameters will open a door for manipulating the impact force and the stress distribution of drop impact in engineering applications, such as polymer drop impact of inkjet printing and raindrops on superhydrophobic surfaces for self-cleaning.

5.2.1 Ambient Atmosphere Pressure

Since the discovery of the effect of ambient air on the splashing of impacting drops on solid surfaces [33], air cushioning in drop impact has attracted great research interests [26]. A thin layer of air underneath an impacting drop induces a sub-micron dimple-like deformation on the bottom of the drop and delays the contact between the drop and

the solid surface [41, 77, 78, 43], which is also shown in Figure 1.5. This effect of air cushioning screens the $1 = \sqrt{t}$ singularity of the pressure at the impact point predicted by the equation:

$$p(r = 0, t) = \frac{1}{2}\rho V^2 + \frac{2\rho V}{\pi}\frac{dr_0}{dt} = \frac{1}{2}\rho V^2 + \frac{\sqrt{6}}{2\pi}\rho V^{3/2} D^{1/2} t^{-1/2}, \tag{5.1}$$

as well as the water hammer pressure at the very early moment of impact. Smith *et al.* calculated the screened pressure on the impacted surface [134]. Before the drop touches the surface, a maximum gas pressure first builds up at the impact axis. As the impact pressure overcomes the gas pressure, an annular pressure maximum develops at later times along a ring where the distance between the bottom of the deformed drop and the surface is smallest at h_{min}. Similar dynamics have also been reported by Mandre and co-workers (Figure 1.7) [113, 39], who further showed that the air underneath an impacting drop can either drain out of the thin layer or be compressed depending on specific impact parameters and the ambient pressure. The compression dynamics are further divided into two different regimes in their theory: the sub-compressible regime at large h_{min} and the super-compressible regime at small h_{min}. In all the cases, the pressure distributions near h_{min} can be described by self-similar solutions. However, systematic experiments investigating the effect of air cushioning on the impact force and the stress distribution of drop impact have not been conducted. With our setup for measuring the stress distribution incorporated with a vacuum chamber, the development of gas pressure underneath an impacting drop can be unveiled experimentally.

5.2.2 Non-Newtonian Drop Impact

Liquid suspensions, emulsions, and polymer solutions are commonly used in chemical process, including spray cooling and printing [135]. Therefore, studying the impact of composite drops and non-Newtonian fluid drops is of great practical importance. For instance, Boyer *et al.* stated that compared to Newtonian drops, the shapes of drops consisting cornstarch suspension are irregular with a breaking of the symmetry [136]. Bartolo *et al.* demonstrated how non-Newtonian flow properties slow down retraction to inhibit rebound [28]. Besides, other literatures have analyzed the dynamics of splashing and retraction [28, 137], the scaling laws of heights of an impacting drop, maximum

spreading diameters, and dimensionless numbers [137, 138, 139]. Interestingly, Driscoll *et al.* showed a drop of dense colloidal suspension impacting on a glass substrate. After impact, a dimple forms at the top of the drop, indicating that the drop is jammed at the bottom but still liquid-like at the top [140]. Exploring how the profiles of stress distribution of drops of complex fluids would be changed is helpful for studying compressing damage to substrates impacted by polymer ink droplets during printing processes.

In the end, it is promising but challenging to study drop impact, especially for the stress distribution of drop impact which has never been systematically measured through experiments. We believe the technique "High-speed stress microscopy" we developed will be a stepping stone for the dynamic analysis of drop impact. For instance, experimental measurements of the stress distribution can directly provide the information about the features of the stress distribution under any complicated impact condition. Furthermore, the measurements of the shear stress may offer insights to the development of a boundary layer and flow patterns inside an impacting drop though experiments. In addition, we also explore the dynamics and the morphology of 2D and 3D explosion cratering in granular media [141, 142]. We expect these works will prepare the way for studying the analogy of explosion cratering and impact cratering.

Bibliography

[1] Walter H Wischmeier and Dwight D Smith. Rainfall energy and its relationship to soil loss. *Eos, Transactions American Geophysical Union*, 39(2):285–291, 1958.

[2] Young Soo Joung and Cullen R Buie. Aerosol generation by raindrop impact on soil. *Nature communications*, 6(1):1–9, 2015.

[3] Edward C Monahan, Donald E Spiel, and Kenneth L Davidson. A model of marine aerosol generation via whitecaps and wave disruption. In *Oceanic whitecaps*, pages 167–174. Springer, 1986.

[4] Runchen Zhao, Qianyun Zhang, Hendro Tjugito, and Xiang Cheng. Granular impact cratering by liquid drops: Understanding raindrop imprints through an analogy to asteroid strikes. *Proceedings of the National Academy of Sciences*, 112(2):342–347, 2015.

[5] Qianyun Zhang, Ming Gao, Runchen Zhao, and Xiang Cheng. Scaling of liquid-drop impact craters in wet granular media. *Physical Review E*, 92(4):042205, 2015.

[6] Song-Chuan Zhao, Rianne de Jong, and Devaraj van der Meer. Raindrop impact on sand: a dynamic explanation of crater morphologies. *Soft Matter*, 11(33):6562–6568, 2015.

[7] Thomas Kenkmann, NA Artemieva, Kai Wünnemann, MH Poelchau, D Elbeshausen, and H NÚÑEZ del PRADO. The carancas meteorite impact crater, peru: Geologic surveying and modeling of crater formation and atmospheric passage. *Meteoritics & Planetary Science*, 44(7):985–1000, 2009.

[8] Young Soo Joung, Zhifei Ge, and Cullen R Buie. Bioaerosol generation by raindrops on soil. *Nature communications*, 8(1):1–10, 2017.

[9] Thomas Boland, Xu Tao, Brook J Damon, Brian Manley, Priya Kesari, Sahil Jalota, and Sarit Bhaduri. Drop-on-demand printing of cells and materials for designer tissue constructs. *Materials Science and Engineering: C*, 27(3):372–376, 2007.

[10] Savas Tasoglu and Utkan Demirci. Bioprinting for stem cell research. *Trends in biotechnology*, 31(1):10–19, 2013.

[11] B-J De Gans, Paul C Duineveld, and Ulrich S Schubert. Inkjet printing of polymers: state of the art and future developments. *Advanced materials*, 16(3):203–213, 2004.

[12] R Andrade, O Skurtys, and F Osorio. Drop impact behavior on food using spray coating: Fundamentals and applications. *Food research international*, 54(1):397–405, 2013.

[13] Nazrin Kooy, Khairudin Mohamed, Lee Tze Pin, and Ooi Su Guan. A review of roll-to-roll nanoimprint lithography. *Nanoscale research letters*, 9(1):1–13, 2014.

[14] Dennis C Kincaid, Kenneth H Solomon, and Joseph C Oliphant. Drop size distributions for irrigation sprinklers. *Transactions of the ASAE*, 39(3):839–845, 1996.

[15] Donald J Hayes, Michael T Boldman, and David B Wallace. Method and apparatus for dispensing spherical-shaped quantities of liquid solder, July 20 1993. US Patent 5,229,016.

[16] Martin Rein. Phenomena of liquid drop impact on solid and liquid surfaces. *Fluid Dynamics Research*, 12(2):61–93, 1993.

[17] FR Smith and David Brutin. Wetting and spreading of human blood: Recent advances and applications. *Current Opinion in Colloid & Interface Science*, 36:78–83, 2018.

[18] Raining drop. `https://en.wikipedia.org/wiki/Drop_(liquid)`.

[19] Soil erosion. https://en.wikipedia.org/wiki/Soil_erosion.

[20] Meteorite impact. https://en.wikipedia.org/wiki/Impact_crater.

[21] Spray coating. https://commons.wikimedia.org/wiki/File:Powder_Coating_Spraying.JPG.

[22] Ink-jet printing. https://en.wikipedia.org/wiki/Printing.

[23] Plasma spraying. https://en.wikipedia.org/wiki/Thermal_spraying.

[24] Arthur Mason Worthington. Xxviii. on the forms assumed by drops of liquids falling vertically on a horizontal plate. *Proceedings of the royal society of London*, 25(171-178):261–272, 1877.

[25] Claas Willem Visser, Philipp Erhard Frommhold, Sander Wildeman, Robert Mettin, Detlef Lohse, and Chao Sun. Dynamics of high-speed micro-drop impact: numerical simulations and experiments at frame-to-frame times below 100 ns. *Soft matter*, 11(9):1708–1722, 2015.

[26] Christophe Josserand and Sigurdur T Thoroddsen. Drop impact on a solid surface. *Annual review of fluid mechanics*, 48:365–391, 2016.

[27] Alexander L Yarin. Drop impact dynamics: splashing, spreading, receding, bouncing.... *Annu. Rev. Fluid Mech.*, 38:159–192, 2006.

[28] Denis Bartolo, Arezki Boudaoud, Grégoire Narcy, and Daniel Bonn. Dynamics of non-newtonian droplets. *Physical review letters*, 99(17):174502, 2007.

[29] Zi Qiang Yang, Yuan Si Tian, and Sigurdur T Thoroddsen. Multitude of dimple shapes can produce singular jets during the collapse of immiscible drop-impact craters. *Journal of Fluid Mechanics*, 904, 2020.

[30] Christopher J Howland, Arnaud Antkowiak, J Rafael Castrejón-Pita, Sam D Howison, James M Oliver, Robert W Style, and Alfonso A Castrejón-Pita. It's harder to splash on soft solids. *Physical review letters*, 117(18):184502, 2016.

[31] David Quéré. Leidenfrost dynamics. *Annual Review of Fluid Mechanics*, 45:197–215, 2013.

[32] Stefan Batzdorf, Jan Breitenbach, Christiane Schlawitschek, Ilia V Roisman, Cameron Tropea, Peter Stephan, and Tatiana Gambaryan-Roisman. Heat transfer during simultaneous impact of two drops onto a hot solid substrate. *International Journal of Heat and Mass Transfer*, 113:898–907, 2017.

[33] Lei Xu, Wendy W Zhang, and Sidney R Nagel. Drop splashing on a dry smooth surface. *Physical review letters*, 94(18):184505, 2005.

[34] Carlo Antonini, Alidad Amirfazli, and Marco Marengo. Drop impact and wettability: From hydrophilic to superhydrophobic surfaces. *Physics of fluids*, 24(10):102104, 2012.

[35] Lei Xu. Liquid drop splashing on smooth, rough, and textured surfaces. *Physical Review E*, 75(5):056316, 2007.

[36] R Rioboo, M Marengo, and C Tropea. Time evolution of liquid drop impact onto solid, dry surfaces. *Experiments in fluids*, 33(1):112–124, 2002.

[37] Michelle M Driscoll, Cacey S Stevens, and Sidney R Nagel. Thin film formation during splashing of viscous liquids. *Physical Review E*, 82(3):036302, 2010.

[38] MB Lesser and JE Field. The impact of compressible liquids. *Annual review of fluid mechanics*, 15(1):97–122, 1983.

[39] Madhav Mani, Shreyas Mandre, and Michael P Brenner. Events before droplet splashing on a solid surface. *Journal of Fluid Mechanics*, 647(1):163–185, 2010.

[40] Yuan Liu, Peng Tan, and Lei Xu. Compressible air entrapment in high-speed drop impacts on solid surfaces. *Journal of Fluid Mechanics*, 716, 2013.

[41] ST Thoroddsen, TG Etoh, K Takehara, N Ootsuka, and Y Hatsuki. The air bubble entrapped under a drop impacting on a solid surface. *Journal of Fluid Mechanics*, 545:203, 2005.

[42] V Mehdi-Nejad, J Mostaghimi, and S Chandra. Air bubble entrapment under an impacting droplet. *Physics of fluids*, 15(1):173–183, 2003.

[43] Ji San Lee, Byung Mook Weon, Jung Ho Je, and Kamel Fezzaa. How does an air film evolve into a bubble during drop impact? *Physical review letters*, 109(20):204501, 2012.

[44] John E Field, J-J Camus, Marc Tinguely, Danail Obreschkow, and Mohamed Farhat. Cavitation in impacted drops and jets and the effect on erosion damage thresholds. *Wear*, 290:154–160, 2012.

[45] Herbrt Wagner. Über stoß-und gleitvorgänge an der oberfläche von flüssigkeiten. *ZAMM-Journal of Applied Mathematics and Mechanics/Zeitschrift für Angewandte Mathematik und Mechanik*, 12(4):193–215, 1932.

[46] Guillaume Riboux and José Manuel Gordillo. Experiments of drops impacting a smooth solid surface: a model of the critical impact speed for drop splashing. *Physical review letters*, 113(2):024507, 2014.

[47] Julien Philippi, Pierre-Yves Lagrée, and Arnaud Antkowiak. Drop impact on a solid surface: short-time self-similarity. *Journal of Fluid Mechanics*, 795:96–135, 2016.

[48] José Manuel Gordillo, Guillaume Riboux, and Enrique S Quintero. A theory on the spreading of impacting droplets. *Journal of Fluid Mechanics*, 866:298–315, 2019.

[49] A Mongruel, V Daru, F Feuillebois, and S Tabakova. Early post-impact time dynamics of viscous drops onto a solid dry surface. *Physics of Fluids*, 21(3):032101, 2009.

[50] Benjamin R Mitchell, Joseph C Klewicki, Yannis P Korkolis, and Brad L Kinsey. The transient force profile of low-speed droplet impact: measurements and model. *Journal of Fluid Mechanics*, 867:300–322, 2019.

[51] Romain Rioboo, Cameron Tropea, and Marco Marengo. Outcomes from a drop impact on solid surfaces. *Atomization and sprays*, 11(2), 2001.

[52] Christophe Clanet, Cédric Béguin, Denis Richard, and David Quéré. Maximal deformation of an impacting drop. *Journal of Fluid Mechanics*, 517:199, 2004.

[53] CHR Mundo, M Sommerfeld, and C Tropea. Droplet-wall collisions: experimental studies of the deformation and breakup process. *International journal of multiphase flow*, 21(2):151–173, 1995.

[54] Denis Bartolo, Christophe Josserand, and Daniel Bonn. Singular jets and bubbles in drop impact. *Physical review letters*, 96(12):124501, 2006.

[55] Yuriko Y Renardy, Stéphane Popinet, Laurent Duchemin, Michael J Renardy, Stéphane Zaleski, Christophe Josserand, MA Drumright-Clarke, D Richard, Christophe Clanet, and David Quéré. Pyramidal and toroidal water drops after impact on a solid surface. 2003.

[56] Yahua Liu, Lisa Moevius, Xinpeng Xu, Tiezheng Qian, Julia M Yeomans, and Zuankai Wang. Pancake bouncing on superhydrophobic surfaces. *Nature physics*, 10(7):515–519, 2014.

[57] JE Field. Elsi conference: invited lecture: liquid impact: theory, experiment, applications. *Wear*, 233:1–12, 1999.

[58] Vinay Sharma, Somnath Chattopadhyaya, and Sergej Hloch. Multi response optimization of process parameters based on taguchi—fuzzy model for coal cutting by water jet technology. *The International Journal of Advanced Manufacturing Technology*, 56(9-12):1019–1025, 2011.

[59] Ilia V Roisman, Edin Berberović, and Cam Tropea. Inertia dominated drop collisions. i. on the universal flow in the lamella. *Physics of fluids*, 21(5):052103, 2009.

[60] Ilia V Roisman. Inertia dominated drop collisions. ii. an analytical solution of the navier–stokes equations for a spreading viscous film. *Physics of Fluids*, 21(5):052104, 2009.

[61] Jens Eggers, Marco A Fontelos, Christophe Josserand, and Stéphane Zaleski. Drop dynamics after impact on a solid wall: theory and simulations. *Physics of fluids*, 22(6):062101, 2010.

[62] Christophe Josserand and Stephane Zaleski. Droplet splashing on a thin liquid film. *Physics of fluids*, 15(6):1650–1657, 2003.

[63] S Santosh Kumar, Ashish Karn, Roger EA Arndt, and Jiarong Hong. Internal flow measurements of drop impacting a solid surface. *Experiments in Fluids*, 58(3):12, 2017.

[64] Jingyin Li, Bin Zhang, Penghua Guo, and Qian Lv. Impact force of a low speed water droplet colliding on a solid surface. *Journal of Applied Physics*, 116(21):214903, 2014.

[65] Dan Soto, Aurélie Borel De Lariviere, Xavier Boutillon, Christophe Clanet, and David Quéré. The force of impacting rain. *Soft matter*, 10(27):4929–4934, 2014.

[66] Leonardo Gordillo, Ting-Pi Sun, and Xiang Cheng. Dynamics of drop impact on solid surfaces: evolution of impact force and self-similar spreading. *Journal of Fluid Mechanics*, 840:190–214, 2018.

[67] Amina Nouhou Bako, Frédéric Darboux, Francois James, Christophe Josserand, and Carine Lucas. Pressure and shear stress caused by raindrop impact at the soil surface: Scaling laws depending on the water depth. *Earth Surface Processes and Landforms*, 41(9):1199–1210, 2016.

[68] Harold Mirels. Laminar boundary layer behind shock advancing into stationary fluid. 1955.

[69] DM Hartley and CV Alonso. Numerical study of the maximum boundary shear stress induced by raindrop impact. *Water Resources Research*, 27(8):1819–1826, 1991.

[70] David M Hartley and PY Julien. Boundary shear stress induced by raindrop impact. *Journal of Hydraulic Research*, 30(3):341–359, 1992.

[71] Nguyen Thanh-Vinh, Kiyoshi Matsumoto, and Isao Shimoyama. Pressure distribution on the contact area during the impact of a droplet on a textured surface. In *2016 IEEE 29th International Conference on Micro Electro Mechanical Systems (MEMS)*, pages 177–180. IEEE, 2016.

[72] Thanh-Vinh Nguyen and Isao Shimoyama. Maximum pressure caused by droplet impact is dependent on the droplet size. In *2019 20th International Conference on Solid-State Sensors, Actuators and Microsystems & Eurosensors XXXIII (TRANSDUCERS & EUROSENSORS XXXIII)*, pages 813–816. IEEE, 2019.

[73] Nick Laan, Karla G de Bruin, Denis Bartolo, Christophe Josserand, and Daniel Bonn. Maximum diameter of impacting liquid droplets. *Physical Review Applied*, 2(4):044018, 2014.

[74] Anne-Laure Biance, Frédéric Chevy, Christophe Clanet, Guillaume Lagubeau, and David Quéré. On the elasticity of an inertial liquid shock. *Journal of Fluid Mechanics*, 554:47, 2006.

[75] Rouslan Krechetnikov and George M Homsy. Crown-forming instability phenomena in the drop splash problem. *Journal of colloid and interface science*, 331(2):555–559, 2009.

[76] Gilou Agbaglah, Christophe Josserand, and Stéphane Zaleski. Longitudinal instability of a liquid rim. *Physics of Fluids*, 25(2):022103, 2013.

[77] Michelle M Driscoll and Sidney R Nagel. Ultrafast interference imaging of air in splashing dynamics. *Physical review letters*, 107(15):154502, 2011.

[78] John M Kolinski, Shmuel M Rubinstein, Shreyas Mandre, Michael P Brenner, David A Weitz, and L Mahadevan. Skating on a film of air: drops impacting on a surface. *Physical review letters*, 108(7):074503, 2012.

[79] Evert Klaseboer, Rogerio Manica, and Derek YC Chan. Universal behavior of the initial stage of drop impact. *Physical review letters*, 113(19):194501, 2014.

[80] MA Nearing, JM Bradford, and RD Holtz. Measurement of force vs. time relations for waterdrop impact. *Soil Science Society of America Journal*, 50(6):1532–1536, 1986.

[81] Frederick Gnichtel Hammitt. *Cavitation and Multiphase Flow Phenomena: FG Hammitt*. McGraw-Hill Book Company, 1980.

[82] Manuel Gamero-Castano, Anna Torrents, Lorenzo Valdevit, and Jian-Guo Zheng. Pressure-induced amorphization in silicon caused by the impact of electrosprayed nanodroplets. *Physical review letters*, 105(14):145701, 2010.

[83] Harold J Brodie. The splash-cup dispersal mechanism in plants. *Canadian Journal of Botany*, 29(3):224–234, 1951.

[84] Andrew K Dickerson, Peter G Shankles, Nihar M Madhavan, and David L Hu. Mosquitoes survive raindrop collisions by virtue of their low mass. *Proceedings of the National Academy of Sciences*, 109(25):9822–9827, 2012.

[85] Sean Gart, Joseph E Mates, Constantine M Megaridis, and Sunghwan Jung. Droplet impacting a cantilever: A leaf-raindrop system. *Physical Review Applied*, 3(4):044019, 2015.

[86] A Sahaya Grinspan and R Gnanamoorthy. Impact force of low velocity liquid droplets measured using piezoelectric pvdf film. *Colloids and Surfaces A: Physicochemical and Engineering Aspects*, 356(1-3):162–168, 2010.

[87] Bin Zhang, Jingyin Li, Penghua Guo, and Qian Lv. Experimental studies on the effect of reynolds and weber numbers on the impact forces of low-speed droplets colliding with a solid surface. *Experiments in Fluids*, 58(9):1–12, 2017.

[88] P Savic and GT Boult. *The fluid flow associated with the impact of liquid drops with solid surfaces*. National Research Council of Canada, 1955.

[89] Sander Wildeman, Claas Willem Visser, Chao Sun, and Detlef Lohse. On the spreading of impacting drops. *arXiv preprint arXiv:1602.03782*, 2016.

[90] Grigory Isaakovich Barenblatt, Grigorii Isaakovĭc Barenblatt, and Barenblatt Grigory Isaakovich. *Scaling, self-similarity, and intermediate asymptotics: dimensional analysis and intermediate asymptotics*. Number 14. Cambridge University Press, 1996.

[91] Lev D Landau, Evgeny M Lifshitz, et al. *Theory of elasticity*, volume 7. Pergamon Press, Oxford New York, 1986.

[92] Guillaume Lagubeau, Marco A Fontelos, Christophe Josserand, Agnès Maurel, Vincent Pagneux, and Philippe Petitjeans. Spreading dynamics of drop impacts. *Journal of Fluid Mechanics*, 713:50, 2012.

[93] S Tabakova, F Feuillebois, A Mongruel, V Daru, et al. First stages of drop impact on a dry surface: asymptotic model. *Zeitschrift für angewandte Mathematik und Physik*, 63(2):313–330, 2012.

[94] Tao Deng, Kripa K Varanasi, Ming Hsu, Nitin Bhate, Chris Keimel, Judith Stein, and Margaret Blohm. Nonwetting of impinging droplets on textured surfaces. *Applied Physics Letters*, 94(13):133109, 2009.

[95] Hyuk-Min Kwon, Adam T Paxson, Kripa K Varanasi, and Neelesh A Patankar. Rapid deceleration-driven wetting transition during pendant drop deposition on superhydrophobic surfaces. *Physical review letters*, 106(3):036102, 2011.

[96] Carl M Bender and Steven A Orszag. *Advanced mathematical methods for scientists and engineers I: Asymptotic methods and perturbation theory*. Springer Science & Business Media, 2013.

[97] Milton Van Dyke. Perturbation methods in fluid mechanics/annotated edition. *NASA STI/Recon Technical Report A*, 75:46926, 1975.

[98] Ilia V Roisman, Romain Rioboo, and Cameron Tropea. Normal impact of a liquid drop on a dry surface: model for spreading and receding. *Proceedings of the Royal Society of London. Series A: Mathematical, Physical and Engineering Sciences*, 458(2022):1411–1430, 2002.

[99] James Legge. *The texts of Taoism*, volume 1. Courier Corporation, 1962.

[100] David Pimentel, Celia Harvey, Pradnja Resosudarmo, K Sinclair, D Kurz, M McNair, S Crist, Lisa Shpritz, L Fitton, Ri Saffouri, et al. Environmental and economic costs of soil erosion and conservation benefits. *Science*, 267(5201):1117–1123, 1995.

[101] PIA Kinnell. Raindrop-impact-induced erosion processes and prediction: a review. *Hydrological Processes: An International Journal*, 19(14):2815–2844, 2005.

[102] Aykut Erkal, Dina D'Ayala, and Lourenço Sequeira. Assessment of wind-driven rain impact, related surface erosion and surface strength reduction of historic building materials. *Building and Environment*, 57:336–348, 2012.

[103] Mingshen Shao, Li Li, Sijing Wang, Enzhi Wang, and Zuixiong Li. Deterioration mechanisms of building materials of jiaohe ruins in china. *Journal of Cultural Heritage*, 14(1):38–44, 2013.

[104] Qulan Zhou, Na Li, Xi Chen, Tongmo Xu, Shien Hui, and Di Zhang. Liquid drop impact on solid surface with application to water drop erosion on turbine blades, part ii: Axisymmetric solution and erosion analysis. *International Journal of Mechanical Sciences*, 50(10-11):1543–1558, 2008.

[105] Tomoki Kondo and Keita Ando. Simulation of high-speed droplet impact against a dry/wet rigid wall for understanding the mechanism of liquid jet cleaning. *Physics of Fluids*, 31(1):013303, 2019.

[106] Ruizi Zhang, Bin Zhang, Qian Lv, Jingyin Li, and Penghua Guo. Effects of droplet shape on impact force of low-speed droplets colliding with solid surface. *Experiments in Fluids*, 60(4):1–13, 2019.

[107] H MichelleáGrandin et al. Micro-well arrays for 3d shape control and high resolution analysis of single cells. *Lab on a Chip*, 7(8):1074–1077, 2007.

[108] Joong Yull Park, Sung Ju Yoo, Eun-Joong Lee, Dae Ho Lee, Ji Young Kim, and Sang-Hoon Lee. Increased poly (dimethylsiloxane) stiffness improves viability and morphology of mouse fibroblast cells. *BioChip Journal*, 4(3):230–236, 2010.

[109] ID Johnston, DK McCluskey, CKL Tan, and MC Tracey. Mechanical characterization of bulk sylgard 184 for microfluidics and microengineering. *Journal of Micromechanics and Microengineering*, 24(3):035017, 2014.

[110] William Thielicke and Eize Stamhuis. Pivlab–towards user-friendly, affordable and accurate digital particle image velocimetry in matlab. *Journal of open research software*, 2(1), 2014.

[111] Matthew S Hall, Rong Long, Chung-Yuen Hui, and Mingming Wu. Mapping three-dimensional stress and strain fields within a soft hydrogel using a fluorescence microscope. *Biophysical journal*, 102(10):2241–2250, 2012.

[112] Ted Belytschko, Yun Yun Lu, and Lei Gu. Element-free galerkin methods. *International journal for numerical methods in engineering*, 37(2):229–256, 1994.

[113] Shreyas Mandre, Madhav Mani, and Michael P Brenner. Precursors to splashing of liquid droplets on a solid surface. *Physical review letters*, 102(13):134502, 2009.

[114] LB Freund. Dynamic fracture mechanics cambridge university press. *New York*, 1990.

[115] Gang Wen, ZhiGuang Guo, and Weimin Liu. Biomimetic polymeric superhydrophobic surfaces and nanostructures: from fabrication to applications. *Nanoscale*, 9(10):3338–3366, 2017.

[116] Sigurdur T Thoroddsen, Kohsei Takehara, and TG Etoh. Micro-splashing by drop impacts. *Journal of Fluid Mechanics*, 706:560–570, 2012.

[117] Minhee Lee, Young Soo Chang, and Ho-Young Kim. Drop impact on microwetting patterned surfaces. *Physics of Fluids*, 22(7):072101, 2010.

[118] Darin Comeau, Kevin LaTourette, and John Pate. The effect of weber number and spread factor of a water droplet impinging on a super-hydrophobic substrate. *Applied mathematics*, 2007.

[119] Yong Chae Jung and Bharat Bhushan. Dynamic effects of bouncing water droplets on superhydrophobic surfaces. *Langmuir*, 24(12):6262–6269, 2008.

[120] Carlo Antonini, Fabio Villa, and Marco Marengo. Oblique impacts of water drops onto hydrophobic and superhydrophobic surfaces: outcomes, timing, and rebound maps. *Experiments in fluids*, 55(4):1–9, 2014.

[121] Yong Han Yeong, James Burton, Eric Loth, and Ilker S Bayer. Drop impact and rebound dynamics on an inclined superhydrophobic surface. *Langmuir*, 30(40):12027–12038, 2014.

[122] Nathan Blanken, Muhammad Saeed Saleem, Carlo Antonini, and Marie-Jean Thoraval. Rebound of self-lubricating compound drops. *Science advances*, 6(11):eaay3499, 2020.

[123] Peichun Tsai, Sergio Pacheco, Christophe Pirat, Leon Lefferts, and Detlef Lohse. Drop impact upon micro-and nanostructured superhydrophobic surfaces. *Langmuir*, 25(20):12293–12298, 2009.

[124] Longquan Chen, Zhiyong Xiao, Philip CH Chan, and Yi-Kuen Lee. Static and dynamic characterization of robust superhydrophobic surfaces built from nano-flowers on silicon micro-post arrays. *Journal of micromechanics and microengineering*, 20(10):105001, 2010.

[125] Longquan Chen, Zhiyong Xiao, Philip CH Chan, Yi-Kuen Lee, and Zhigang Li. A comparative study of droplet impact dynamics on a dual-scaled superhydrophobic surface and lotus leaf. *Applied surface science*, 257(21):8857–8863, 2011.

[126] Nagesh D Patil, Rajneesh Bhardwaj, and Atul Sharma. Droplet impact dynamics on micropillared hydrophobic surfaces. *Experimental Thermal and Fluid Science*, 74:195–206, 2016.

[127] Junlei Chen, Jihui Wang, and Aiqing Ni. A review on rain erosion protection of wind turbine blades. *Journal of Coatings Technology and Research*, 16(1):15–24, 2019.

[128] Enrique S Quintero, Guillaume Riboux, and José Manuel Gordillo. Splashing of droplets impacting superhydrophobic substrates. *Journal of Fluid Mechanics*, 870:175–188, 2019.

[129] H Lastakowski, F Boyer, A-L Biance, C Pirat, and C Ybert. Bridging local to global dynamics of drop impact onto solid substrates. *Journal of Fluid Mechanics*, 747:103–118, 2014.

[130] Ji San Lee, Su Ji Park, Jun Ho Lee, Byung Mook Weon, Kamel Fezzaa, and Jung Ho Je. Origin and dynamics of vortex rings in drop splashing. *Nature communications*, 6(1):1–8, 2015.

[131] Yujie Wang, Ayoub El Bouhali, Sijia Lyu, Lu Yu, Yue Hao, Zhigang Zuo, Shuhong Liu, and Chao Sun. Leidenfrost drop impact on inclined superheated substrates. *Physics of Fluids*, 32(11):112113, 2020.

[132] Guillaume Dupeux, Marie Le Merrer, Christophe Clanet, and David Quéré. Trapping leidenfrost drops with crenelations. *Physical review letters*, 107(11):114503, 2011.

[133] Cunming Yu, Mengfei Liu, Chunhui Zhang, Hao Yan, Minghui Zhang, Qingshan Wu, Mingjie Liu, and Lei Jiang. Bio-inspired drag reduction: from nature organisms to artificial functional surfaces. *Giant*, page 100017, 2020.

[134] FT Smith, L Li, and GX Wu. Air cushioning with a lubrication/inviscid balance. *Journal of Fluid Mechanics*, 482:291–318, 2003.

[135] Leon Bolle and J Cl Moureau. Spray cooling of hot surfaces. *Multiphase science and technology*, 1(1-4), 1982.

[136] François Boyer, Enrique Sandoval-Nava, Jacco H Snoeijer, J Frits Dijksman, and Detlef Lohse. Drop impact of shear thickening liquids. *Physical review fluids*, 1(1):013901, 2016.

[137] Marine Guémas, Álvaro G Marín, and Detlef Lohse. Drop impact experiments of non-newtonian liquids on micro-structured surfaces. *Soft Matter*, 8(41):10725–10731, 2012.

[138] A Dechelette, PE Sojka, and CR Wassgren. Non-newtonian drops spreading on a flat surface. *Journal of Fluids Engineering*, 132(10), 2010.

[139] Miguel Balzan, Ayoub Abdollahi, Frederick S Wells, and Geoff R Willmott. Drop impact of non-newtonian dairy-based solutions. *Colloids and Surfaces A: Physicochemical and Engineering Aspects*, page 126895, 2021.

[140] Phalguni Shah and Michelle M Driscoll. Drop impact dynamics of complex fluids: A review. *arXiv preprint arXiv:2012.10433*, 2020.

[141] Ming Gao, Xiao Liu, Luana Pasetti Vanin, Ting-Pi Sun, Xiang Cheng, and Leonardo Gordillo. Dynamics and scaling of explosion cratering in granular media. *AIChE Journal*, 64(8):2972–2981, 2018.

[142] Tianyu Liu, Boen Cao, Xiao Liu, Ting-Pi Sun, and Xiang Cheng. Explosion cratering in 3d granular media. *Soft matter*, 16(5):1323–1332, 2020.

[143] Clayton T McKee, Julie A Last, Paul Russell, and Christopher J Murphy. Indentation versus tensile measurements of young's modulus for soft biological tissues. *Tissue Engineering Part B: Reviews*, 17(3):155–164, 2011.

Appendix A

Supporting Information to Section 2

A.1 Propagation of Isobars

We analyze the propagation of isobars within impacting drops based on the self-similar solution of [47]. The self-similar dimensionless vertical and radial coordinates are defined as $\eta \equiv z/\sqrt{\tau}$ and $\xi \equiv r/\sqrt{\tau}$. Consequently, the self-similar velocity potential and pressure fields can be written as $\widetilde{\Phi}(\eta,\xi) = \Phi(r,z,t)/\sqrt{\tau}$ and $\widetilde{P}(\eta,\xi) = \sqrt{\tau}P(r,z,t)$, respectively (cf. Equations (3.1) and (3.2) in [47]). The self-similar arguments of the pressure and potential fields show that the length scale of the self-similar structure should scale as $z \sim r \sim \sqrt{\tau}$. In the dimensional form, we have $z \sim r \sim \sqrt{U_0 D t}$ as shown in Section 2.3.2.

The self-similar pressure along the axis of symmetry ($r = 0$) in the lab frame is given by (cf. eq. (3.35b) in [47])

$$P(r=0,z,\tau) = \frac{3\sqrt{6\tau}}{\pi\left(6\tau + 4z^2\right)}. \tag{A.1}$$

Note that we use D, instead of R, as the relevant length scale to construct dimensionless variables. Thus, equation (A.1) has different prefactors compared with Equation (3.35b)

in [47]. Correspondingly, in the self-similar frame of reference, we have

$$\widetilde{P}\left(0,\eta\right)=\frac{\delta}{\pi}\frac{\delta^2}{\delta^2+\eta^2}, \tag{A.2}$$

where $\delta=\sqrt{6}/2$. Far away from the impact region, Equation (A.2) can be expanded as

$$\lim_{\eta\to\infty}\widetilde{P}\left(0,\eta\right)=\frac{\delta}{\pi}\left(\frac{\delta}{\eta}\right)^2-\frac{\delta}{\pi}\left(\frac{\delta}{\eta}\right)^4+\mathcal{O}\left[\left(\frac{\delta}{\eta}\right)^6\right]. \tag{A.3}$$

Thus, the isobar of $\widetilde{P}_0$ far from the region of impact can be obtained through the first term of the expansion. In the self-similar frame, it is given by

$$\frac{\delta}{\pi}\left(\frac{\delta}{\eta}\right)^2=\widetilde{P}_0 \tag{A.4}$$

This yields $\eta=\left(\delta^3/(\pi\widetilde{P}_0)\right)^{1/2}\sim\tau^0$ in terms of the self-similar variable and $z\sim\sqrt{\tau}$ in terms of the lab-frame variable. On the other hand, the isobar of P_0 in the lab frame is given by

$$\frac{\delta}{\pi}\left(\frac{\delta}{\eta}\right)^2\frac{1}{\sqrt{\tau}}=P_0, \tag{A.5}$$

where the additional $1/\sqrt{\tau}$ comes from the scaling of the self-similar pressure field $\widetilde{P}$. Equation (A.5) gives the location of the isobar in the lab frame, $\eta\sim\tau^{-1/4}$ in the terms of self-similar variable and $z\sim\tau^{1/4}$ in terms of the lab-frame variable. Thus, in the dimensional form, we have the location of the isobar

$$z\sim\left(U_0D^3t\right)^{1/4} \tag{A.6}$$

as shown in Section 2.3.3.

Appendix B

Supporting Information to Section 3

B.1 Comparison of the Impact Craters by Liquid Drops and Solid Spheres

To demonstrate the efficiency of impacting drops in erosion, we compare the size of impact craters by water drops and those by solid spheres on both granular media and plaster slabs.

For granular media, we use a nylon sphere of diameter $D = 3.0$ mm with impact velocity $U = 2.97$ m/s, impacting normally onto the at surface of a granular bed composed of 90 μm glass beads. The water drop used in our experiments has a similar diameter $D = 3.4$ mm and impact velocity $U = 2.97$ m/s. Since the density of nylon $\rho = 1.15$ g/cm^3 is quantitatively similar to the density of water, the water drop and the solid nylon sphere have similar impact momentum and energy. The diameter of the drop-impact crater is 1.38 cm, which is noticeably larger than that of the solid-sphere-impact crater at 1.04 cm (Figure 3.1(b) and (c) of Section 3). De Jong and co-workers have compared the size of impact craters by liquid drops and those by solid spheres over a wide range of impact velocities [**?**]. They also found that the diameter of drop-impact craters is consistently larger than that of solid-sphere-impact craters. Moreover, they showed that the excavated volume is the same for both drop-impact and solid-sphere-impact craters

Impact Condition	Water-drop Craters		Steel-ball Craters		Number of Impact
	Diameter (mm)	Depth (mm)	Diameter (mm)	Depth (mm)	
Same N	8	2.75	5.6	0.59	$N = 2500$
Same E	8	2.75	3.1	0.39	$N = 2500$ for drops $N = 235$ for balls
Same P (Inelastic)	8	2.75	3.0	0.38	$N = 2500$ for drops $N = 126$ for balls
Same P (Elastic)	8	2.75	2.6	0.32	$N = 2500$ for drops $N = 63$ for balls

Table B.1: Comparison of the size of impact craters by water drops and steel balls.

when plotting against a rescaled deformation energy.

Plaster slabs are much harder than granular media. Hence, we need to repeat impact many times in order to create noticeable craters. We use water drops of $D = 3.0$ mm falling from a height of 35 cm at $U = 2{:}6$ m/s, which impact normally onto the initially at surface of plaster slabs. We repeat impact N = 2500 times and then measure the resulting crater. The time interval between two impacts is 20 s. Thus, the total time of the experiment for the erosion of a plaster slab is close to 14 hours. Note that cratering in plaster slabs by water drops is not due to the dissolution of the slabs by water. We check that a slab fully immersed in water maintains its mechanical strength after 36 hours. It is difficult to control precisely the impact locations of nylon spheres falling from a high height of 35 cm over many repeated impacts. Hence, we use steel balls of $D = 5.0$ mm falling from a lower height of 10 cm at $U = 1.4$ m/s instead. To make meaningful comparisons between water-drop-impact craters and steel-ball-impact craters, we consider three different impact conditions, i.e., the same number of impact (N), the same total impact energy (E) and the same total impact momentum (P). For the impact momentum, we treat the collisions between steel balls and slabs as either elastic or perfectly inelastic. In all situations, the diameter and the depth of the impact craters by water drops are consistently larger than those by steel spheres. The results are summarized in the table below:

B.2 Integration Path of the Impact Pressure Measurements

Figure B.1 shows the integration path used in our calculation of impact pressure (Section 3.2.4).

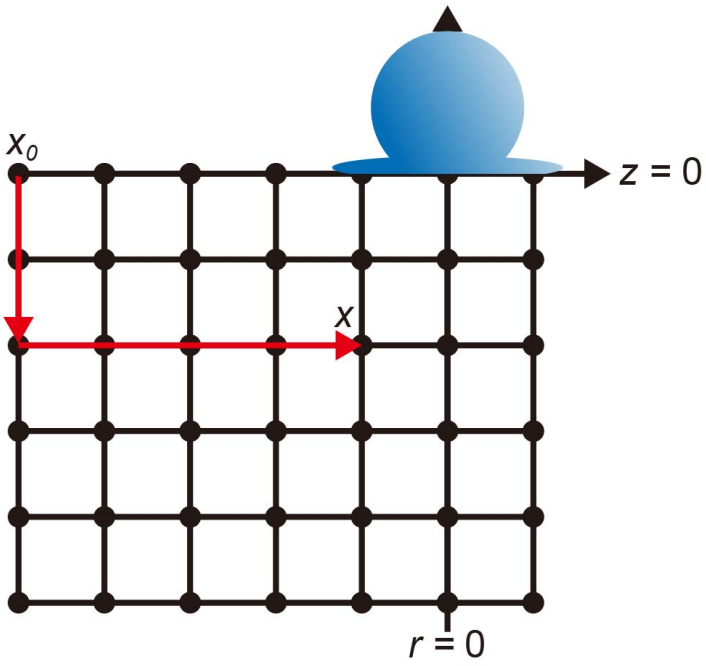

Figure B.1: Impact pressure measurements. Red arrows indicate the integration path for calculating the pressure at point x from the reference point at x_0.

B.3 The Scaling Factor for the Impact Stress of Solid-sphere Impact

The force of solid-sphere impact on an elastic medium follows the Hertzian contact law [66, 143],

$$F(x) = \frac{2\sqrt{3}}{3} E^* D^{1/2} x^{3/2}, \tag{B.1}$$

where x is the vertical displacement and the reduced Young's modulus E^* follows

$$\frac{1}{E^*} = \frac{1-\nu^2}{E} + \frac{1-\nu_s^2}{E_s} \approx \frac{1-\nu^2}{E}. \tag{B.2}$$

Here, ν and E are the Poisson's ratio and the Young's modulus of the PDMS gel and ν_s and E_s are the Poisson's ratio and the Young's modulus of the steel sphere. Since $E_s \gg E$, we ignore the deformation of the steel sphere. Balancing the elastic potential

with the kinetic energy of the solid sphere,

$$\int_0^{x_{max}} F(x)dx = \frac{4\sqrt{2}}{15}\frac{E}{1-\nu^2}D^{1/2}x_{max}^{5/2} = \frac{\pi}{12}\rho_s D^3 U^2, \tag{B.3}$$

we have the maximum displacement into the gel

$$x_{max} = [\frac{5\sqrt{2}\pi}{32}(\frac{1-\nu^2}{E})\rho_s D^{5/2}U^2]^{2/5}, \tag{B.4}$$

where ρ_s is the density of the sphere. Thus, the maximum pressure is given by

$$p_{max} = \frac{F_{max}}{\pi a^2} = \frac{4\sqrt{2}}{3\pi}(\frac{E}{1-\nu^2})(\frac{x_{max}}{D})^{1/2} = [\frac{4\sqrt{2}}{3\pi}(\frac{5\sqrt{2}\pi}{32})^{1/5}\frac{1}{(1-\nu^2)^{4/5}}]E^{4/5}(\rho_s U^2)^{1/5}, \tag{B.5}$$

where $F_{max} = F(x = x_{max})$ is the maximum force and $a = \sqrt{Dx_{max}/2}$ is the radius of the contact area at the maximum force. Ignoring the constant factor of $\mathcal{O}(1)$ in the square bracket, the maximum pressure provides the scale for the impact stress of solid-sphere impact

$$\sigma \sim E^{4/5}(\rho_s U^2)^{1/5}. \tag{B.6}$$

B.4 Effect of the Wettability and the Stiffness of PDMS Gels

The position of the shear-stress maximum does not depend on the wettability and stiffness of the PDMS gels (Figure B.2). The contact angle of the hydrophobic gels is about 90°, whereas that of the hydrophilic gels is less than 10°.

B.5 Shear Force of Drop Impact and Solid-Sphere Impact

Figure B.4 compares the shear force of the drop impact and that of the solid-sphere impact.

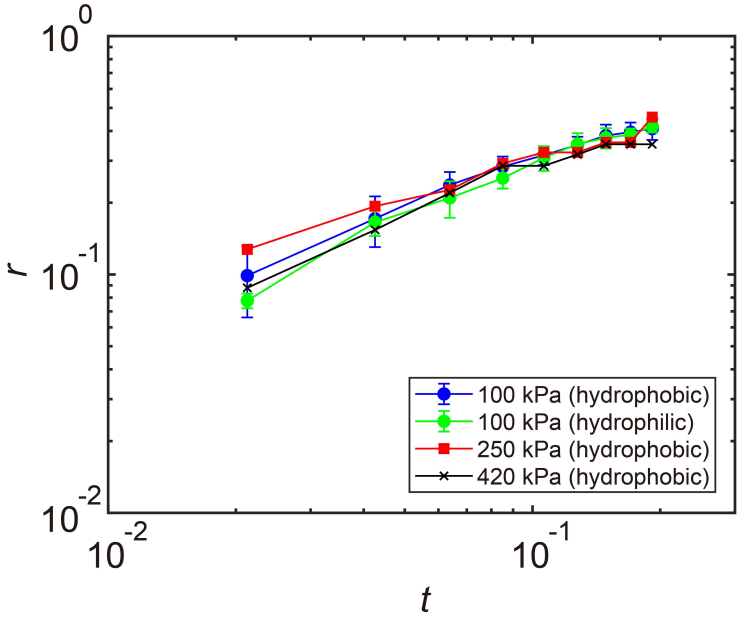

Figure B.2: Position of the shear-stress maximum. The position of the maximum shear stress of drop impact as a function of time on substrates of different wettabilities and Young's moduli.

B.6 Theory and Numerical Solutions

The deformation of an elastic medium at small strains is described by the Navier-Lamé equation:

$$(\lambda + 2G)\nabla(\nabla \cdot \mathbf{u}) - G\nabla \times (\nabla \times \mathbf{u}) + \mathbf{F} = \rho_s \frac{\partial^2}{\partial^2}\mathbf{u}, \tag{B.7}$$

where $\lambda = E\nu/[(1+\nu)(1-2\nu)]$ is the Lamé coefficient and $G = E = [2(1+\nu)]$ is the shear modulus. ρ_s, E and ν are the density, Young's modulus and Poisson's ratio of the medium, respectively. $u = (u_r; u_\theta, u_z)$ is the displacement of the medium in a cylindrical coordinate. F is the body force per unit volume. Since F is small compared with the impact stress, we ignore the term below. In the cylindrical coordinate, an axisymmetric

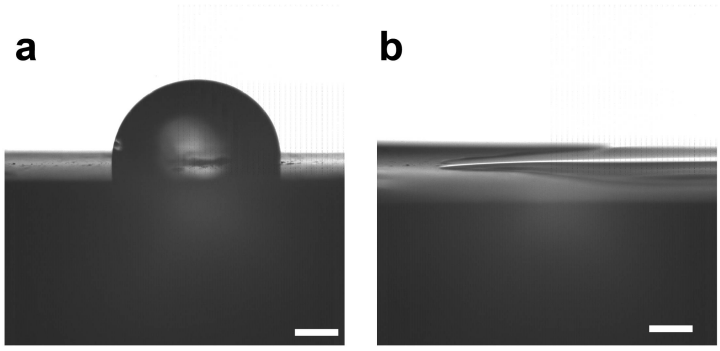

Figure B.3: Wettability of PDMS. (a) PDMS is intrinsically hydrophobic with a contact angle around 90°. (b) After the plasma treatment, the surface of PDMS becomes hydrophilic with a contact angle less than 10°. The scale bar: 1 mm.

Navier-Lamé equation reduces to

$$(\lambda + 2G)\partial_r(\frac{1}{r}\partial_r(ru_r) + \partial_z u_z) + G\partial_z(\partial_r u_z - \partial_z u_r) = \rho_s \frac{\partial^2}{\partial t^2} u_r \tag{B.8}$$

$$(\lambda + 2G)\partial_z(\frac{1}{r}\partial_r(ru_r) + \partial_z u_z) - G\frac{1}{r}\partial_r[r\partial_r u_z - \partial_z u_r)] = \rho_s \frac{\partial^2}{\partial t^2} u_z. \tag{B.9}$$

To determine the deformation of the medium under the impact of a liquid drop, we adopt the theoretical prediction on the pressure and shear stress distributions of incompressible drops on infinitely rigid substrates [47]. It should be noted that the impact stress, in particular the impact pressure of liquid drops, should be modified due to the deformation of substrates of finite stiffness and deviate from the prediction based on non-deformable substrates. The interplay between an impacting drop and a deformable impacted substrate is quite complicated. To the best of our knowledge, the analytical solutions for the impact stresses of liquid drops on deformable elastic media are not available. A theoretical investigation of this complicated mathematical problem is certainly beyond the scope of our current work. The approximation we take here can be considered as the one-way coupling between the impacting drop and the impacted substrate, where the substrate deforms under the impact stress of the liquid drop but does not modify the impact stress. The approximation is justified when the deformation of the substrate is small as the case of our experiments. The stiffer

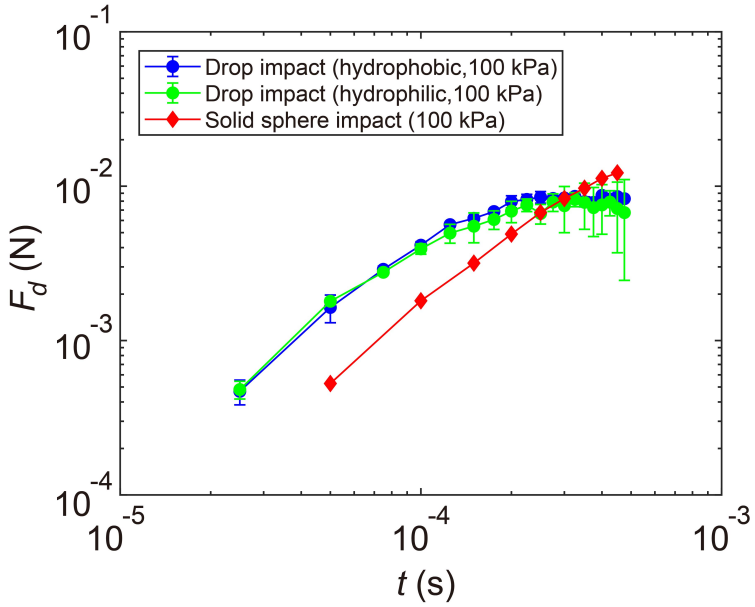

Figure B.4: Shear force of drop impact and solid-sphere impact. Both the shear force and the time are expressed in dimensional forms. The impact conditions are specified in the main text. Young's modulus of the PDMS gel is 100 kPa.

the material, the more accurate the approximation. Indeed, the position of the shear-stress maximum is independent of Young's modulus of gels (Figure B.2), indicating the weak effect of the gel stiffness on the kinematics of impacting drops within the range of our experiments. Furthermore, the agreement between the measured shear stress distributions and the theoretical prediction (Equation 3.21 of Section 3) away from the singular region further suggests that the one-way approximation qualitatively captures the dynamics of impacted substrates under drop impact.

Under the one-way approximation, we apply the pressure and shear distributions of incompressible drops on infinitely rigid substrates as the boundary conditions of

Equation B.8 and B.9:

$$\sigma_{rz}|_{z=0} = \begin{cases} \sqrt{\frac{6}{\pi^3}\frac{1}{Re}}\rho U^2 \frac{2rD}{3UDt-2r^2} & \text{for } r \le r_c \\ 0 & \text{for } r > r_c \end{cases} \tag{B.10}$$

$$\sigma_{zz}|_{z=0} = \begin{cases} \frac{3\sqrt{2}}{2\pi}\rho U^2 \frac{D}{\sqrt{3UDt-2r^2}} & \text{for } r \le r_c \\ 0 & \text{for } r > r_c \end{cases} \tag{B.11}$$

where ρ, U and D are the density, the impact velocity and the diameter of the liquid drop, respectively. $r_c = \sqrt{6UDt}/2$ is the position of the turning point, where the pressure and shear stress diverge and exhibit the finite-time singularity [47].

To make the equations dimensionless, we propose the following scaling, $t \sim DM^2/U$, $u \sim DM^2$, $(r, z) \sim DM$, $(\lambda, G) \sim E$ and $\sigma \sim ME \sim E^{1/2}(\rho U^2)^{1/2}$. Here, we introduce a Mach number $M \equiv U\sqrt{\rho_s/E}$, which compares the speed of the impacting drop U with the characteristic speed of sound of the elastic medium $\sqrt{E/\rho_s}$. For example, the speed of the body **P** wave is $v_p = C\sqrt{E/\rho_s}$, where $C = \sqrt{(1-\nu)/[(1+\nu)(1-2\nu)]} = 4.1 \sim \mathcal{O}(1)$ for an elastic material with Poisson's ratio $\nu = 0.49$. $M = 0.292$ in our experiments. In comparison, the scaling for the impact stress of solid-sphere impact is given by $\sigma \sim E^{4/5}(\rho_s U^2)^{1/5}$ (Equation B.6).

The proposed scaling yields the following boundary value problem of partial differential equations:

$$(\lambda + 2G)\partial_r(\frac{1}{r}\partial_r(ru_r) + \partial_z u_z) + \partial_z(\partial_r u_z - \partial_z u_r) = \rho_s \frac{\partial^2}{\partial t^2} u_r \tag{B.12}$$

$$(\lambda + 2G)\partial_z(\frac{1}{r}\partial_r(ru_r) + \partial_z u_z) - \frac{1}{r}\partial_r[r\partial_r u_z - \partial_z u_r)] = \rho_s \frac{\partial^2}{\partial t^2} u_z, \tag{B.13}$$

and

$$\sigma_{rz}|_{z=0} = \begin{cases} \sqrt{\frac{6}{\pi^3}\frac{1}{Re}}\frac{\rho}{\rho_s}\frac{2r}{3t-2r^2} & \text{for } r \le r_c \\ 0 & \text{for } r > r_c \end{cases} \tag{B.14}$$

$$\sigma_{zz}|_{z=0} = \begin{cases} \frac{3\sqrt{2}}{2\pi}\frac{\rho}{\rho_s}\frac{1}{\sqrt{3t-2r^2}} & \text{for } r \le r_c \\ 0 & \text{for } r > r_c \end{cases} \tag{B.15}$$

where all the quantities are now dimensionless with the turning point at $r_c = \sqrt{6t}/2$. The resulting equations and boundary conditions are independent of M in terms of the scaled variables. The scaling suggests that the shear force should scale as $F_d \sim \sigma D^2 \sim E^{1/2}(\rho U^2)^{1/2} D^2$, matching our experimental measurements at different E (Figure 3.6). Note that the density ratio between the liquid and the gel $\rho/\rho_s \approx 1$ in our experiments.

We numerically solve Equation B.12 and B.13 with the boundary conditions Equation B.13 and B.14 using the finite element method (Section 3.2.6). To avoid the singularity at r_c, we impose a small cut-off δ:

$$\sigma_{rz}|_{z=0} = \begin{cases} \sqrt{\frac{6}{\pi^3}\frac{1}{Re}}\frac{\rho}{\rho_s}\frac{2r}{3(1+\delta)t-2r^2} & \text{for } r \le r_c \\ 0 & \text{for } r > r_c \end{cases} \tag{B.16}$$

$$\sigma_{zz}|_{z=0} = \begin{cases} \frac{3\sqrt{2}}{2\pi}\frac{\rho}{\rho_s}\frac{1}{\sqrt{3(1+\delta)t-2r^2}} & \text{for } r \le r_c \\ 0 & \text{for } r > r_c \end{cases} \tag{B.17}$$

We choose $\delta = 0.1$ for our numerical simulations, as a good convergence of solutions is achieved for the chosen spatial resolution.

The solutions of the radial and vertical displacements of the surface of the elastic media, $u_r(r, z = 0, t)$ and $u_z(r, z = 0, t)$, are shown in Fig. S4a and b. The in-phase oscillations of u_r and u_z are the characteristic feature of the surface Rayleigh wave. The wave emerges beyond $r_c(t)$ around $t_c \approx 0.1$, consistent with experimental observations. Moreover, the surface wave is sharp and concentrated with a well-defined peak propagating along the surface radially at a speed V_R, agreeing well with the theoretical prediction of the speed of the Rayleigh wave. The much faster but weaker body P-wave can be also identified (Figure B.5(a)).

To compare with the surface wave induced by the impact of solid spheres, we apply the Hertzian contact force (Equation B.1) in the dimensionless form

$$F = \frac{2\sqrt{2}}{3}\frac{M^2}{1-\nu^2}t^{3/2} \tag{B.18}$$

over a small region of $r_0 = 0.1$ around the impact axis on the surface of the elastic medium. Here, we assume that the displacement $x = Ut$ at short times, consistent with experiments [66]. In comparison with the impact stress of liquid drops, Equation B.18

is stationary in space and does not exhibit the finite-time singularity associated with the turning point. Figure S4c and d show the numerical solutions of $u_r(r, z = 0, 0)$ and $u_z(r, z = 0, 0)$. Different from the shock-induced sharp surface wave by drop impact, the Rayleigh wave of solid-sphere impact emits continuously from $r = 0$ upon the impact at $t = 0$ and is much broader and more diffusive in nature.

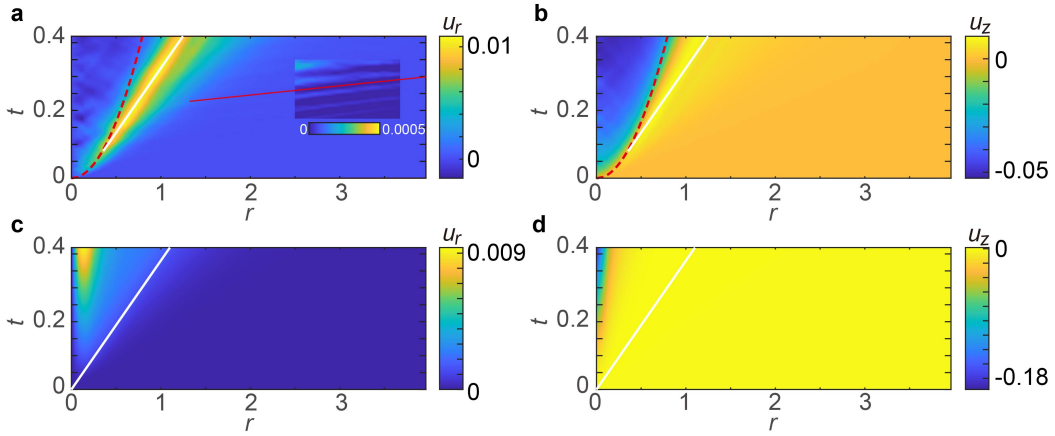

Figure B.5: Numerical solutions of the surface wave induced by the impact of liquid drops and solid spheres.(a),(b), The spatiotemporal diagram of the radial displacement of the gel surface $u_r(r,t)$ and the vertical displacement of the gel surface $u_z(r,t)$ induced by the impact of a liquid drop. (c),(d), The spatiotemporal diagram of $u_r(r,t)$ and $u_z(r,t)$ induced by the impact of a solid sphere. $u_r(r,t)$ and $u_z(r,t)$ are normalized by the diameter of the impactors D. The red dashed lines in (a) and (b) indicate the position of the turning points where pressure and shear stress reach maximum. The white solid lines indicate the propagation of the Rayleigh wave, whereas the red solid line in (a) indicates the propagation of the body P-wave. Inset of (a) shows $u_r(r,t)$ with a colormap of a much narrower range in order to highlight the presence of the much weaker P-wave.

Appendix C

Supporting Information to Section 4

C.1 Tracking of Dynamic and Kinematic Features

Based on the theoretical prediction and experimental analysis from Quintero, Riboux and Gordillo, the positions of the lamella and turning point on smooth surfaces and structured surfaces are the same at early times, and the scaling of the turning point r_c all follows $r_c = \sqrt{3t}$ [48, 128]. Figure C.1 and Figure 3.4 shows the consistency between their works and our experimental results. We also deliver the dynamic tracking of the position of the maximum g_r of both surfaces, and it shows that the position of the maximum g_r correlates with the position of r_c (Figure C.2).

C.2 Shear Stress Fields of Smooth Surfaces and Patterned Surfaces

Figure C.3 shows the temporal evolution of the shear stress fields of smooth surfaces and patterned surfaces.

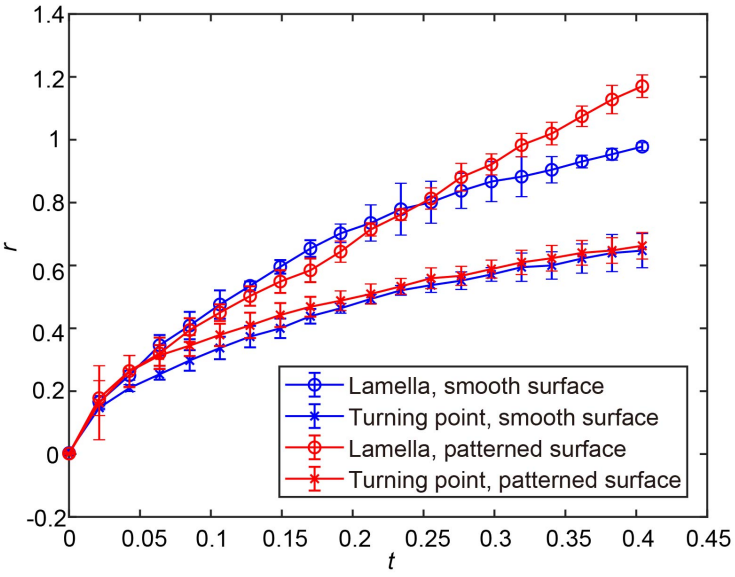

Figure C.1: Position of kinematic features of an impacting drop on the smooth and the micropatterned PDMS. In the initial impact regime ($t < 0.25$), there is no significant difference for the position of the lamella and turning point on the smooth surface or the patterned surface.

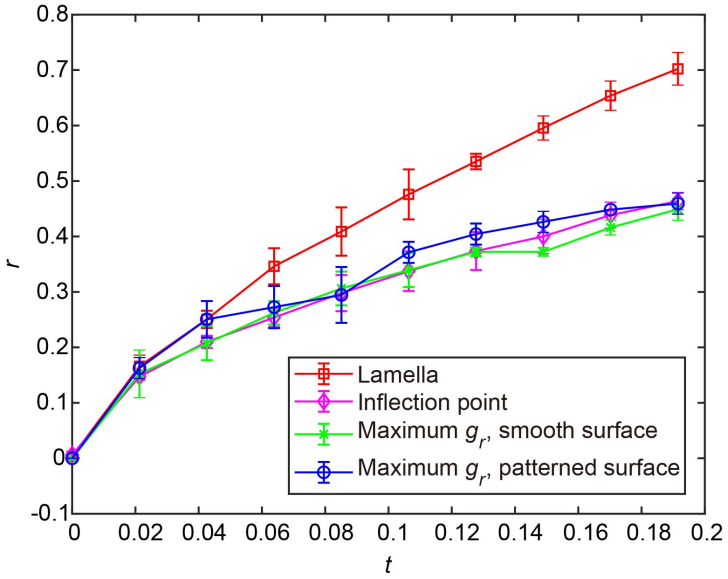

Figure C.2: Dynamic tracking of the maximum g_r of the smooth and the micropatterned PDMS. The position of the lamella, the turning point, and the maximum g_r of the smooth surface and patterned surface.

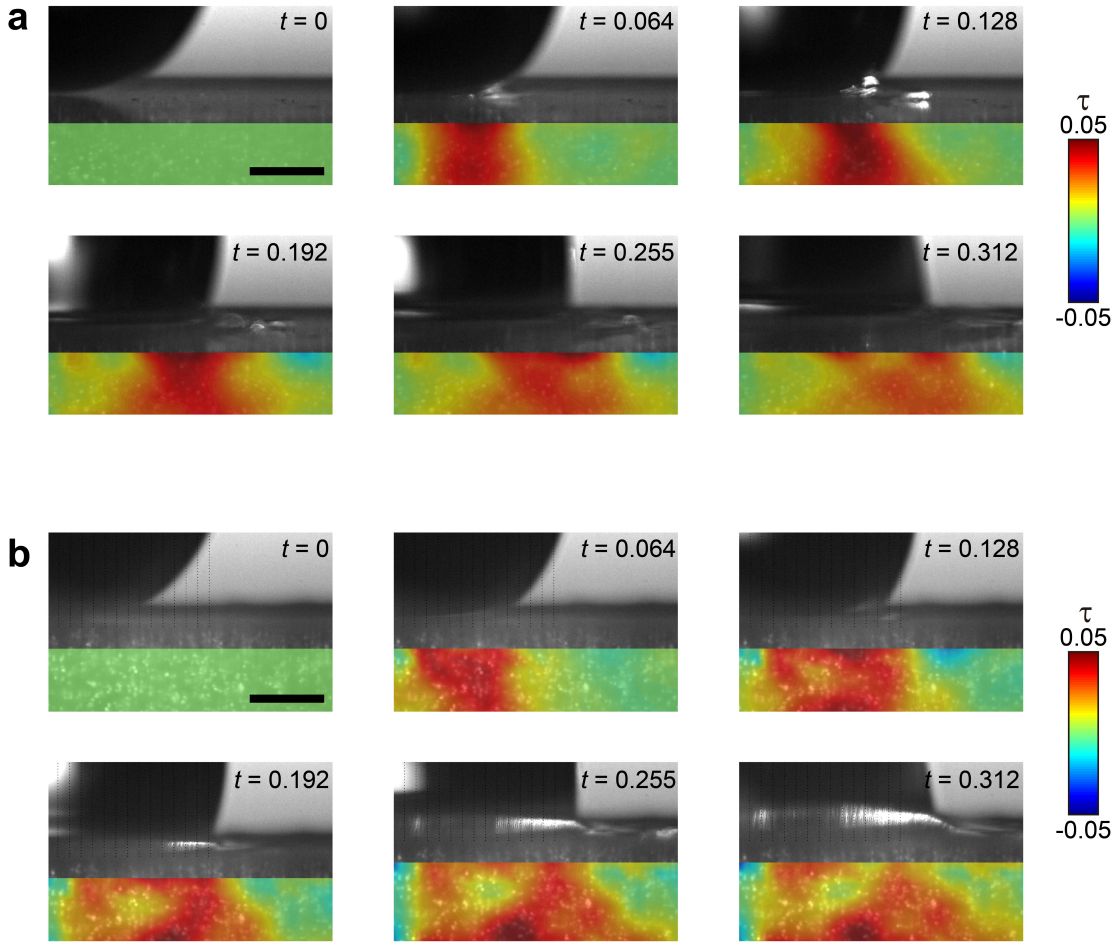

Figure C.3: Shear stress fields of drop impact of the smooth and the micropatterned PDMS. (a) and (b) show the time series of the shear stress fields of the smooth surface and the micropatterned surface, respectively. (b), The maximum τ starts to become flatten at earlier time and then split into several peaks. (a), Differently, the maximum τ splits into two peaks at the later time. τ is non-dimensionalized by ρU^2. Scale bar: 1 mm.